Copyright

by

Xiaoming YAN

2003

The Dissertation Committee for Xiaoming Yan certifies
that this is the approved version of the following dissertation:

Fundamental Surface Science Investigations of Systems Designed to Address Technological Issues

Committee:

John Michael White, Supervisor

Alan Campion

Jason B. Shear

Peter J. Rossky

C. Buddie Mullins

Fundamental Surface Science Investigations of Systems Designed to Address Technological Issues

by

Xiaoming Yan, B. S., M. S.

Dissertation

Presented to the Faculty of the Graduate School of

The University of Texas at Austin

in Partial Fulfillment

of the Requirements

for the Degree of

Doctor of Philosophy

The University of Texas at Austin

August, 2003

Dedication

To Sharon, my wife and my soul partner,

and to my parents

Fundamental Surface Science Investigations of Systems Designed to Address Technological Issues

Publication No._____________

Xiaoming Yan, Ph.D.
The University of Texas at Austin, 2003

Supervisor: John Michael White

Organometallic chemical vapor deposition of (MeCp)Ir(COD) onto Rh is simulated experimentally with and without co-reactant oxygen via isothermal reaction mass spectrometry. Auger electron spectroscopy (AES) is used to analyze the resulting film purity. Without oxygen, continuous film deposition occurs above 750 K. A large amount of carbon incorporates, and a final composition of C_4Ir is inferred. At the steady state of film growth, acetylene is the only volatile product. Before reaching steady state, various hydrocarbon species are observed. With enough oxygen, the precursor combusts and pure Ir is deposited above 600 K. At steady state, the main by-products are CO and H_2O.

The thermal decomposition of tert-butoxy (TBO) with co-adsorbed O and NO is studied using temperature programmed desorption and AES on Rh foil and Cu(111). On Cu(111) with $NO_{(a)}$, some TBO decomposes below 240 K to form H_2O, CO, CO_2, C_2H_2, proposed imide and acetate, and others disproportionate to tert-butyl alcohol, isobutene and adsorbed oxygen at 610 K. On Rh with $NO_{(a)}$, two oxygen-containing fragments—TBO and a stabilized oxametallacycle—coexist. The proposed oxametallacycle decomposes at 350 K to acetone, while TBO, relatively stable in the presence of N and NO, decomposes to isobutene at 500 K. On Rh with $O_{(a)}$, TBO is stable only up to 380 K where, assisted by O, it decomposes to acetone and butene via a transient form of the oxametallacycle.

Thermally evaporated Ag is deposited onto a thin solid water layer on clean hafnia, titania and functionized titiania surfaces. After thermal desorption of water, scanning tunneling microscopy (STM) and atomic force microscopy (AFM) reveals Ag particles on these surfaces. On HfO_2, particles have lateral dimensions between 5 and 20 nm and, in many cases, with heights exceeding the thickness of the original water layer. More interesting, particles form 1D bead-like strings spontaneously on 18 L ice. However, on trimethyl acetic acid (TMAAH) pre-saturated TiO_2(110), only a few huge particles form. The difference is attributed to the different surface hydrophilicities, which affect both the initial ice layer growth and the competition between dewetting and desorption of adsorbed water.

Table of Contents

List of Tables

List of Figures

This page is intentionally left blank

Chapter 1: Introduction

1.1 CONCEPTS AND APPLICATIONS OF SURFACE SCIENCE

The plane or curved two-dimensional boundary of a liquid or solid object defines its surface. The field of surface science was founded by Sabatier, Haber, Langmuir, Taylor and many others from the end of 19th century to the beginning of 20th century. They strove to impact the important chemical technologies of their day through the improvement of catalytic reactivity and selectivity. Their research, using relatively simple tools, led to the development of many fundamental surface principles that form the basis for current scientific understanding. The modern definition of surface science is, "*the study of surfaces and surface phenomena on the atomic or molecular level*" [1.1]. The goal of current surface science research using modern instruments and advanced theoretical methods is to understand surface behavior at the ultimate limit of atomic detail, expanding three major commercial technologies: catalysis, microelectronics and chemical sensing.

Due to the urgent, yet timeless, concerns about energy use, environmental impact and global economics, catalysis—a process modification increasing the rate of a chemical reaction induced by material unchanged chemically at the end of the reaction—has played a crucial role in the chemical industry since the 1960's. One of the most active topics in this field of research today is joint NO_x reduction and CO oxidation [1.2]. The challenge is to fully oxidize unburned hydrocarbons and CO while simultaneously reducing NO_x to N_2 under all conditions of engine use: cold start and steady-state operation over a broad range of air and fuel mixtures. The replacement of noble metal catalysts used currently is another major goal in this discipline. Other hot topics include polymerization, hydrocarbon reconstruction and partial oxidation. In these applications selectivity is much more important than reaction rate because yield and the expense of product separations strongly determine the ultimate cost of production. Related to NO_x reduction and hydrocarbon partial oxidation, thermal decomposition of an alkoxy species, common partial oxidation intermediates, on metal surfaces was studied with and without co-adsorbed NO in Chapter 3 of this dissertation.

Silicon-based technologies are at the core of computer manufacturing. The fabrication of microelectronic circuits often involves layer-by-layer deposition of semiconductor, metal and insulator thin films in various configurations [1.3]. The film thickness of each of these materials is typically on the order of 1-100 nm, and these layers alternate in both two and three dimensions. The fabrication of these layers is carried out by surface processes using chemical vapor deposition (CVD), physical vapor deposition (PVD), or sputter deposition assisted by a radiofrequency plasma. Chemical vapor deposition, most specifically metallorganic chemical vapor deposition (MOCVD), often involves complex chemical reactions at and just above growing interfaces [1.4]. To simulate a MOCVD process, an ultrathin metal film was deposited on a metal surface using an iridium precursor in Chapter 2 in this dissertation.

The aim of chemical sensing research [1.5] is to detect chemical species that are present in air, water, soil or creature bodies in very low concentrations. Monitoring changes in the chemical or physical properties of sensors induced by adsorbates is a strategy to detect and quantify the adsorbed species. Doped semiconductive oxides—SnO_2 and ZnO—have been studied extensively for this purpose. The dopants include group VIII and coinage metals [1.6, 1.7]. Ag was deposited on select, well characterized surfaces to help understanding these systems of transition metal on oxide surfaces in Chapter 4 of this dissertation.

1.2 SURFACE TECHNIQUES

One good way to classify surface analysis techniques is on the basis of stimulation-detection species (Table 1.1). In addition to the traditional surface analysis techniques, microscopies, including scanning electron microscopy (SEM), scanning transmission electron microscopy (STEM), atomic force microscopy (AFM) and scanning tunneling microscopy (STM), offer analysis with better spatial resolution. However, some, AFM and STM, provide little chemical information. Without doubt, temperature-programmed desorption (TPD) is one of the most powerful approaches for identifying surface fragments and deducing reaction pathways. It is particularly useful in systems where the species of interest are stable at temperatures above where dissociation products, e.g. $H_{(a)}$ and $OH_{(a)}$, recombine and desorb. Three techniques—TPD, AES and STM—have been used extensively used in this dissertation and will be described in more detail.

Table 1.1: Survey of popular surface techniques

Stimulation	Detected	Technique	Depth detected
Electron in KeV	Electron	Auger electron spectroscopy	3-5 ML
Electron in 10eV	Electron	Low energy electron diffraction	1-3 ML
Electron in 10eV	Electron	Electron energy loss spectroscopy	1 ML
Electron in 10Kev	Electron	Reflection high energy electron diffraction	1-3 ML
Ion (Cs^+)	Ion	Secondary ion mass spectroscopy	3-5 ML
Ion (He^+)	Ion	Ion scattering spectroscopy	1 ML
Light (X-ray)	Electron in 100eV	X-ray photoelectron spectroscopy	3-5 ML
Light (X-ray)	Electron in 10eV	Ultraviolet photoelectron spectroscopy	3-5 ML
Light (IR)	Light	Reflection adsorption infrared spectroscopy	1 ML

1.2.1 Time-of-flight mass spectrometry TPD (TOFMS-TPD)

TPD [1.8] is a powerful surface science technique that provides important information about species present and their reaction history on a surface. The gas phase products, generally monitored by mass spectrometry (MS) under vacuum or gas chromatography (GC) under high pressure, must be closely related to the adsorbed species. When the thermal energy is high, $T\Delta S>\Delta H$, surface species can either desorb or react. The former is a relatively simple process, and it is called desorption-limited desorption. The analysis of surface reactions by TPD, also named temperature programmed reaction spectroscopy (TPRS), is more complicated analytically and can provide information about reaction pathways. Adsorbates that undergo surface reactions may dissociate or rearrange to form new molecules that either desorb promptly, known as reaction-limited desorption, or stay on the surface in their new forms. Species from a reaction-limited desorption contain both elemental and chemical information about their surface precursor(s). For example, it is plausible to propose an oxametallacycle intermediate, $-_{(a)}CH_2C(CH_3)_2O_{(a)}-$ from a close review of TPD data when acetone and isobutene desorb at the same temperature (see Chapter 3). Sometimes it is not straightforward to resolve different species in MS data acquired during a TPD, e.g., both N_2O and CO_2 have base peaks at the same mass-to-charge ratio. This puzzle can be solved either by experiments using isotopicly labeled adsorbates or by carefully examining the full desorption mass spectrum for other identifying or excluding evidence. A full desorption mass spectrum not only helps in identifying the desorbing species, but also guarantees all desorption species are detected. Acquisition of full range MS data quickly over the temperature ramp can be realized by using time-of-flight mass spectrometry (TOFMS) with fast data collection systems [1.9].

Figure 1.1 shows the schematic diagram of TOFMS-TPD experiments. There, an adsorbate is activated and desorbs as the temperature rises. Meanwhile, full range MS data are collected by a digital signal averager (DSA) powered TOFMS, which can sum 10,000 individual scans (1-450 amu) within 0.6 s. After both MS and temperature data are transferred to a personal computer (PC), final TPD results are presented as an intensity-mass-temperature three dimensional surface. A cross section along the temperature axis gives a full mass spectrum at a temperature of interest and a cross section along the mass-to-charge axis nets a traditional 2-D TPD.

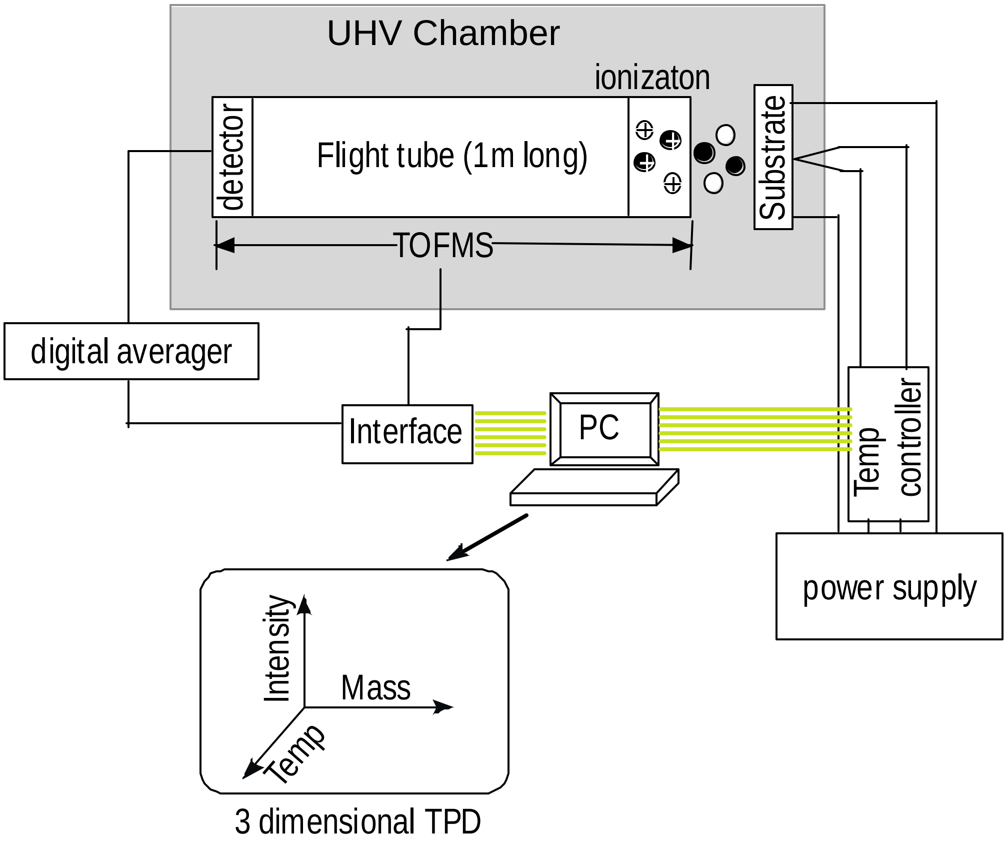

Figure 1.1 Schematic of a TOFMS-TPD experiment. After the substrate is dosed, its temperature is raised through a controlled ramp. The adsorbed molecules are activated and desorb. The desorbing species and temperature are monitored using TOFMS and coordinated to thermocouple measurements as a function of time. The final output is a 3 dimensional TOFMS-TPD spectrum (see Figure 2.1): Intensity vs. temperature (time) and mass.

1.2.2 Auger electron spectroscopy (AES)

AES [1.10] is widely used to investigate the elemental and chemical composition of the first few atomic layers and to map elemental distribution in very small (μm) features. The Auger process was first described by Pierre Auger in 1925 [1.11] to explain the radiationless relaxation of excited ions observed in a cloud chamber. Following core level ionization caused by high energy incident electrons (Figure 1.2), an atom can relax to a lower energy state through a two electron coulombic rearrangement that leaves the atom in a doubly ionized state. The energy difference between these two states is carried away by the ejected Auger electron. The emitted electrons can be detected with an energy analyzer (conventionally, cylindrical mirror analyzer) and are characteristic of each elemental species and reflect elements as unique quantum systems. Every element except hydrogen and helium emits Auger electrons and thus may be identified by its Auger spectrum (Intensity vs. Electron Energy).

Besides AES's primary use in elemental quantitative and qualitative analysis, some information about the chemical environment of the source ion can also be provided by the energy position and line shape of an Auger peak. Referring to standard samples, one can define the chemical state of detected atoms. For example, sp^2 and sp^3 hybridizations of C are distinguished in Figure 3.2. Another very useful application of AES is to estimate overlayer thicknesses [1.12]. When an Auger electron passes through an overlayer, both elastic and inelastic scattering may occur. Inelastic scattering will decrease the AES signal intensity. The probability of inelastic scattering is determined by the effective attenuation length (EAL) of the overlayer. For any material, the farther an Auger electron must travel, the greater the probability of it undergoing inelastic scattering, losing some kinetic energy. So, knowing the EAL of the overlayer and AES intensity of a clean surface, the overlayer thickness can be estimated by the attenuation of AES intensity. One example of this technique in this dissertation is its use to estimate the thickness of solid ice thin film on HfO_2 given in Chapter 4.

1.2.2 Scanning tunneling microscopy (STM)

The use of ultrahigh vacuum STM has become vital to the understanding of surface reconstructions, adsorbate-substrate and adsorbate-adsorbate interactions, and surface reactions and diffusion on the atomic and molecular level [1.13, 1.14]. Unlike traditional surface techniques, such as AES, XPS and LEED, STM probes small areas of the surface in real time and in real space, allowing observations of individual, isolated atomic-scale surface phenomena such as single molecular diffusion, vibration and reaction. Still, how well a system of 10^3-10^6 particles that can be imaged by STM can represent a larger ensemble (>10^{15} particles) remains an open question.

The principles underlying STM are quite simple (Figure 1.3). The tunneling current (I) decays exponentially with increasing tip-sample distance (d). At a typical tunneling distance (d=0.5-1.0 nm, I=0.1 nA), a vertical resolution of 10^{-15} m can be readily achieved. High lateral resolution of 10^{-14} m is possible with an atomically sharp tip. The accurate tip positioning in X, Y and Z directions is realized by a piezo tube scanner. As shown in Figure 1.3, a typical tip may have several smaller "sub-tips" protruding from its larger tip end, which may have a radius of curvature on the order of tens of nanometers. When a single sub-tip supplies a large majority of the tunneling current (>90%), the tip is considered to be atomically sharp. When this is not the case, artificial images may result from the simultaneous interactions of other minor tips with the surface. Other crucial issues related to the resolution are vibration isolation, sample thermal drifting, and scanner creeping.

While STM gives detailed information about local electron density or empty orbitals the experiment is, however, blind to elemental information about the system imaged. This makes the direct analysis of images difficult. Interpreting STM data is often based upon theoretical modeling, but many times the perturbation caused by STM tip is unpredictable. This difficulty may be overcome with the maturation of single molecule spectroscopy [1.15].

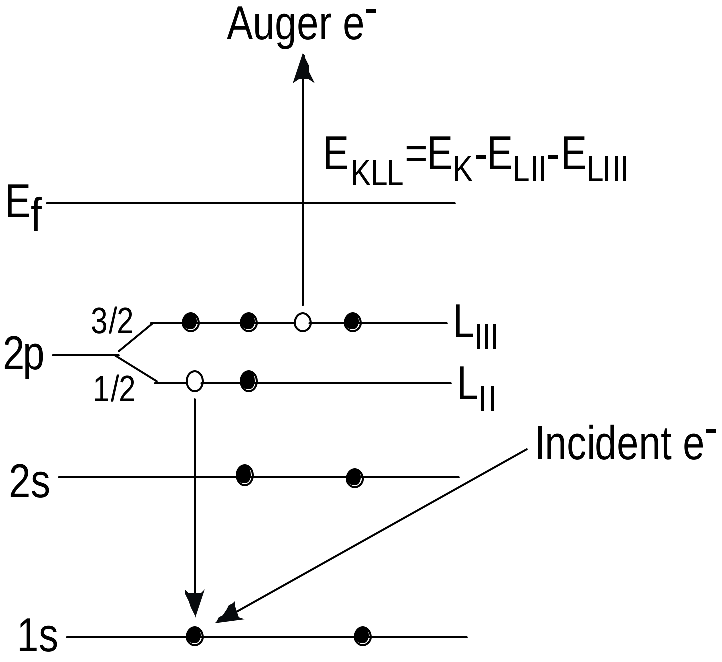

Figure 1.2: Schematic of Auger electron emission from oxygen, O(KLL). The incident electron causes the ejection of a K shell electron and the hole in K shell is refilled by an electron in L_{II}, releasing energy to emit an L_{III} electron to vacuum.

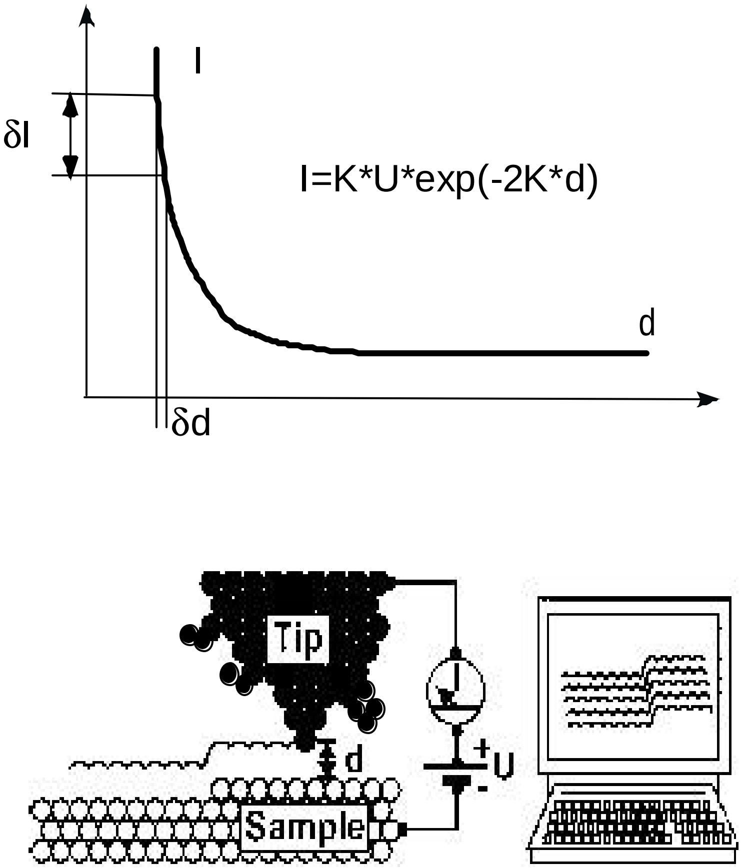

Figure 1.3: Schematic of a scanning tunneling microscopy (STM) system. STM operates at distances in the region of steeply decreasing slope. Thus, a very small distance change between the surface and tip causes a large change tunneling current. The relation between tunneling current (I) and tip-sample distance (d) is given where U is the bias voltage between tip and sample. K is a system dependent constant correlated to the work functions of the tip and sample. The lower panel shows a tip-sample interaction. Typically, d=0.5 nm, I=0.2 nA and U=2 V. Several sub-tips are drawn intentionally to show the origin of the multiple tip effect.

1.3 OVERVIEW OF DISSERTATION

1.3.1 Chapter 2: Experimental simulation of iridium thin film using (5-methylcyclopentadienyl)(1,5-cyclooctadiene) iridium, ((MeCp)Ir(COD))

Describing the chemical pathways of organometallic compounds during the chemical vapor deposition of transition metals is an interesting challenge for surface chemists, a challenge characterized by both fundamental and practical issues. Realizing conformally-controlled, thin pure film deposition of transition metals is of potential value to the microelectronics industry. On a more fundamental level, it is a challenge to describe how a gas phase organometallic precursor collides with, adsorbs on, and decomposes on a changing surface.

In Chapter 2, MOCVD of (MeCp)Ir(COD), $C_{14}H_{19}Ir$, onto a rhodium surface is performed with and without co-reactant oxygen under vacuum and analyzed via isothermal reaction mass spectrometry. AES was used to analyze the resulting film purity. Without oxygen, continuous film deposition occurs on a surface above 750 K, large amount of carbon incorporates, and a final composition of C_4Ir is inferred. At the steady state of film growth, acetylene is the only volatile product. Before reaching steady state, various hydrocarbon species desorb. With enough oxygen, the precursor combusts and pure Ir is deposited above 600 K. At the steady state, the main by-products are CO and H_2O. The reaction sticking coefficient of (MeCp)Ir(COD) onto Rh is also measured.

1.3.2 Chapter 3: Tertiary-butoxy ($(CH_3)_3CO_{(a)}$-) thermal decomposition on Rh and Cu surfaces with co-adsorbed NO and O

For several decades surface chemists have studied small molecules (number of non-hydrogen atoms less than 6) on single crystal surfaces under ultrahigh vacuum conditions. The scientific beauty of these works is that the adsorbate-substrate interactions, surface reconstruction and surface reaction mechanisms can be demonstrated clearly. However, the number of possible reaction pathways increases factorially as the number of non-hydrogen atoms increases [1.16]. Use of the currently available results from smaller molecules to understand the reaction paths of medium sized molecules (7-10 non-hydrogen atoms) is one of the basic science motivations of this project. Practically, this project is directly related to two industrial applications: alkene partial oxidation and NO_x reduction by alkenes and alcohols.

In Chapter 3, both tertiary butyl nitrite (TBN) and tertiary butyl alcohol (TBA) were used to synthesize tertiary butoxy (TBO) on clean and oxygen-covered Rh and Cu surfaces. The thermal decomposition of TBO with co-adsorbed NO and

O was studied using TOFMS-TPD and AES. For TBN on clean Cu(111), adsorbed TBO and NO form as the dissociation products of TBN. N_2O and N_2 desorb at 194 K and leave adsorbed N and O on the surface. Some tert-butoxy reacts at low temperatures (<240 K) to form water, carbon monoxide, carbon dioxide, acetylene, proposed imide and acetate intermediates, and the remaining TBO disproportionates to tert-butyl alcohol, isobutene and adsorbed oxygen at 610 K. The proposed mechanisms at low temperature is initialized by C-H bond cleavage followed by C-C bond breaking to form adsorbed methylene. This methylene can couple to form di-σ-bonded ethylene which can either dehydrogenate to acetylene desorbing at 335 K via a vinyl intermediate or be partially oxidized to acetate that dissociates at 580 K. There is also evidence of N-H bond formation during this process. The high temperature tert-butoxy disproportionation is a bimolecular reaction involving direct hydrogen intermolecular transfer. For TBN on clean Rh, there is evidence that a monolayer decomposes to form NO and two oxygen-containing fragments, TBO and a stabilized oxametallacycle. The proposed oxametallacycle decomposes at 350 K to acetone, while TBO, relatively stable in the presence of N and NO, decomposes to isobutene at 500 K. For TBA dosed onto an O-covered surface, the O—H bond breaks between 200 and 300 K to form *t*-butoxy. This occurs in competition with TBA desorption. The TBO is stable only up to 380 K where, assisted by O, it decomposes to acetone and butene via a transient form of the oxametallacycle involved in TBN. Combustion reactions to form water, carbon monoxide and carbon dioxide compete. For monolayer TBA dosed on a clean Rh surface, H_2, H_2O and CO, but no acetone or butene, appear in TPD and carbon remains on the surface after annealing to elevated temperatures.

1.3.3 Chapter 4: Nanoparticle formation of Ag deposition onto an ice layer on clean and modified oxide surfaces

Because of their unique electronic and structural properties, considerable attention has been directed to nanoparticles, especially transition metal nanoparticles on oxides. One interesting example of how surface chemistry changes on the nanoscale is that CO does not poison the catalytic activity of silica supported Pt nanoparticles in the reactions for ethylene hydrogenation as it does Pt(111) [1.17]. To avoid the effects of averaging over a broad distribution of particle sizes, monodisperse distributions of nanoparticles are sought for basic research investigations. Thus, there is strong motivation to explore various means of preparing and characterizing a monodisperse set of size-controlled nanoparticles spread over a macroscopic area of a planar oxide support.

In Chapter 4, an alternative technique to grow coinage metal nanoparticles on oxides—vapor deposition into a buffer layer, is described. Thermally evaporated Ag was deposited onto a thin (~1.2 nm) crystalline ice layer on clean hafnia, titania and functionalized titiania surfaces. After controlled thermal desorption of water by heating to 300 K, scanning tunneling microscopy (STM) and atomic force microscopy (AFM) reveals Ag particles on these surfaces. On HfO_2, particles have lateral dimensions between 5 and 20 nm and, in many cases, with heights exceeding the thickness of the original water layer. Fewer, higher and more regular Ag particles are formed in the presence, as compared to the absence, of ice. On clean TiO_2(110), the particle size distribution peaks at 3-4 nm with the shape of pancakes. Interestingly, one dimensional bead-like strings of Ag particles are formed spontaneously with deposition onto 18L ice on TiO_2(110). However, on trimethyl acetic acid (TMAAH) pre-saturated TiO_2(110), very large particles, ~10 nm high and ~25 nm in diameter form. The difference is attributed to the different surface hydrophilicities, which affect both the initial ice layer growth and the dewetting and desorption competition of adsorbed water on the surfaces.

References

[1.1] Somorjai, G. A. *Chem. Rev*. **1996**, 96(4), 1223

[1.2] Taylor, K. C. *Catal. Rev.-Sci. Eng.* **1993**, *35* (4), 457

[1.3] Ekerdt, J. G.; Sun, Y.-M.; Szabo, A.; Szulczewski, G. J.; White, J. M. *Chem. Rev*. **1996**, 96, 1499

[1.4] Gates, Stephen M. *Chem. Rev*. **1996**, 96, 1519

[1.5] Cammann, K.; Lemke, U.; Rohen, A.; Sander, J.; Wilken, H.; Winter, B. *Angewandte Chemie* **1991**, 103(5), 519

[1.6] Van De Walle, C. G. *Materials Science Forum* **2000**, 338-342 (Pt. 2, Silicon Carbide and Related Materials, Part 2), 1561

[1.7] Mizsei, J., L. Pirttiaho, M. Karppinen, & V. Lantto,. *Sensors and Actuators, B: Chemical* **2000**, B65, 195

[1.8] Hubbard, A. T., Ed., *Handbook of Surface Imaging and Visualization*, Chapter 59, CRC Press, **1995**

[1.9] Kim, C.; Yan, X.-M.; White, J. M. *Rev. Sci. Instrum*. **2000**, 71(9), 3502

[1.10] *Handbook of Auger Electron Spectroscopy*, 3rd Edition, Physical Electronics, **1995**

[1.11] Auger, P. *J. Physique Radium* **1925**, 6, 205

[1.12] Powell, C.J. *NIST Electron Effective-Attenuation-Length Database*, Version 1.0, 2001

[1.13] Kubby, J. A.; Boland, J. J. *Surf. Sci. Rep*. **1996**, 24, 61

[1.14] Chen, C. J. *Introduction to Scanning Tunneling Microscopy*, Oxford Press, London, 1993

[1.15] Ho, W. *J. Chem. Phys.* **2002**, 117(24), 11033

[1.16] Ihm, H. Ph.D. Dissertation: *Thermal activation and intermediates of six-membered cyclic hydrocarbons and alkyl nitrites on platinum(111) and copper* 2000, 169 pp, University of Texas at Austin

[1.17] Grunes, J.; Zhu, J.; Yang, M.; Somorjai, G. A. *Catal. Lett*. **2003**, 86(4), 157

This page is intentionally left blank

Chapter 2: Adsorption, decomposition and combustion of (methylcyclopentadienyl)(1,5-cyclooctadiene) iridium on clean and oxygen-covered Rh

2.1 OVERVIEW

Thin Ir metal films are used as gate and electrode materials in the semiconductor devices. To understand the deposition reaction kinetics leading to high quality films, the adsorption, decomposition and combustion of (methylcyclopentadienyl)(1,5-cyclooctadiene) iridium, (MeCp)Ir(COD), on clean and oxygen-covered polycrystalline Rh surfaces has been studied by temperature-programmed desorption and isothermal reaction spectroscopy using time-of-flight mass spectrometry, and Auger electron spectroscopy. During early stages of dosing at 100 K on clean Rh, there is partial decomposition of (MeCp)Ir(COD) and, in subsequent TPD, only H_2 desorbs. For higher doses, (MeCp)Ir(COD) and H_2, but no hydrocarbons, desorb. The H_2 evolves in several saturable peaks reflecting stepwise C-H bond breaking. In isothermal reaction spectroscopy (IRS) involving dosing between 350 and 750 K, desorbing products include hydrocarbons with intensities varying with temperature and dosing time. Total sticking probabilities (S_t) are unity on clean Rh but decrease as deposition products accumulate. Above 550 K, the decomposition reaction continues even when the Rh surface is completely covered with precursor decomposition products. On an oxygen-covered surface, monolayer molecularly adsorbed (MeCp)Ir(COD) desorbs at 325 K competing with decomposition to form adsorbed MeCp and COD. We infer that these react with adsorbed oxygen to form O-containing organic surface-bound fragments that decompose to desorb only CO_2, CO and H_2O since no other O-containing products were detected in the 3D spectra. While dosing both (MeCp)Ir(COD) and O_2, pure Ir film growth occurs above 500 K provided there is a large excess of O_2. When dosing these two reactants at 450 K, O, C, H and Ir all accumulate to give a slowly growing film that slowly evolves CO but negligible H_2, H_2O or CO_2.

2.2 INTRODUCTION

The decomposition of organometallic compounds on metal surfaces is of both industrial and scientific interest: deposition of metal thin films and understanding the interaction between these compounds and metal surfaces are both fascinating problems. Roadmaps for microelectronics manufacturing involve future use of dielectric materials with higher dielectric constants than SiO_2 and moves in this direction may require electrode materials other than highly doped Si. For this purpose, selected group VIII transition metals, including Ir, are of interest, e.g., dynamic random access memory cell capacitors. Depositing them from metallorganic precursors (MOCVD) is an attractive processing route. MOCVD can be described as a three-step process: (1) precursor adsorption, (2) precursor decomposition and metal atom deposition, and (3) ligand removal. The last step often determines the quality of deposited films. Co-reactant gases are widely used to remove the organic ligands either by reduction or oxidation reactions to obtain pure Ir films [2.1-2.3]. Commonly the reductant is H_2 and the oxidant is O_2. Alkenes reacting with oxygen, catalyzed heterogeneously by Rh, either fully oxidize to form CO_2, H_2O and CO [2.4], or partially oxidize to yield ketones or alcohols [2.5, 2.6]. There are two different combustion reaction pathways proposed: direct (oxygen-activated) and indirect (decomposition and oxidation) combustions [2.7, 2.8]. Partial oxidation reactions typically occur via oxametallacycle intermediates formed by direct oxygen addition to a carbon atom that is not bonded to the metal to form a -C-O-M linkage followed by either (1) β-H elimination and hydrogenation at the α carbon to form ketones or (2) hydrogenation at the O-metal bond to form alcohols. Inhibition of dehydrogenation of CH_x groups by O(a) is regarded as the key for partial oxidation of alkenes on Rh(111)-p(2x1)-O since combustion to CO_2, CO and H_2O takes place at lower O(a) coverage where highly active Rh sites are available.

(Methylcyclopentadienyl)(1,5-cyclooctadiene) iridium, (MeCp)Ir(COD), is promising because of its low melting point (~ 40 ^{o}C) [2.1], fair solubility in toluene and acetone [2.2], and chemical and thermal stability [2.1, 2.2]. In bench scale chemical vapor deposition (CVD) experiments, its gas phase pyrolysis started at 680 K with nearly simultaneous release of C_6H_6 and C_8H_{10} as all the covalent and dative bonds of this precursor broke. For surface reactions on oxide and nitride substrates, in the presence of sufficient O_2, the ligands oxidize and pure polycrystalline Ir films are formed [2.1-2.3]. However, the products formed in either the absence or presence of O_2 were not identified, providing one motivation for the present work. A polycrystalline Rh foil was chosen as the substrate because: (1) the chemical properties of Rh mimic those of Ir but the Auger spectra are distinguishable, (2) in any case, once the film thickness exceeds one monolayer, the precursor will interact with an Ir surface, (3) Ir films grown with this precursor are typically polycrystalline [2.1-2.3], so the polycrystalline character of the Rh is not detrimental.

In this chapter, the adsorption, decomposition and combustion of (MeCp)Ir(COD) on clean and O-covered polycrystalline Rh surfaces were probed by time-of-flight mass spectrometry in both temperature-programmed desorption (TPD) and isothermal reaction spectroscopy (IRS) modes, and by Auger electron spectroscopy (AES). To simulate MOCVD processes, the interaction with a metal suface (Rh) of a gas phase iridium-containing precursor, (MeCp)Ir(COD), in the presence of various amount of O_2, was investigated by IRS experiments, and conditions were established for the deposition of pure Ir films.

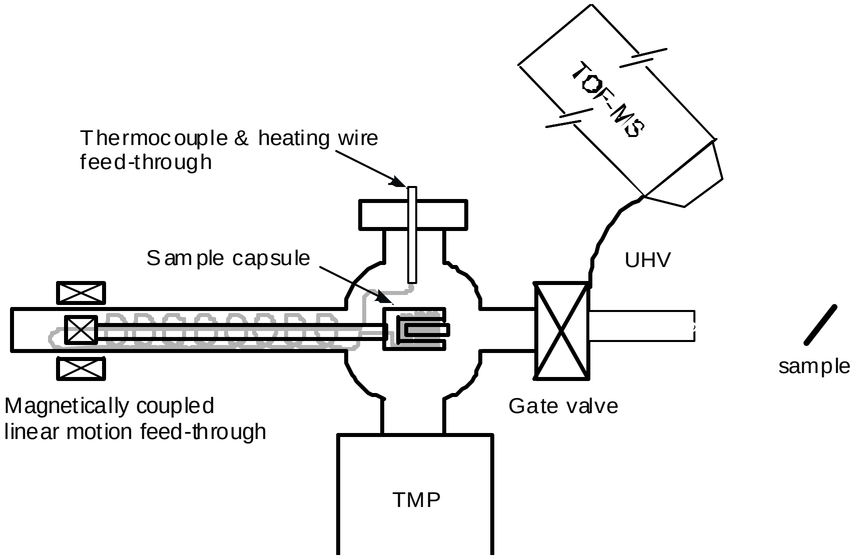

Figure 2.1a: Design of solid doser for low vapor pressure substances. The source vapor pressure is controlled by its temperature, which can be as high as 500 K. During dosing the source is transferred into the UHV chamber by a magnetically coupled feed-through.

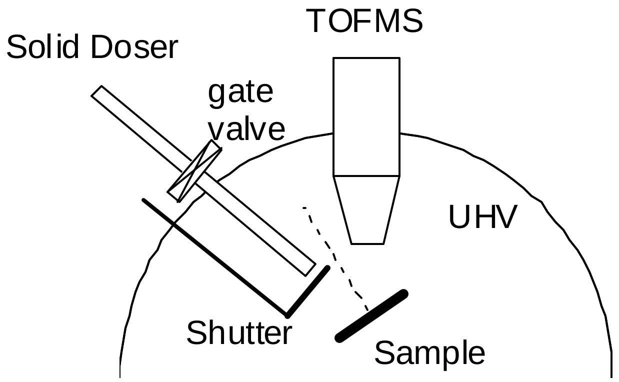

Figure 2.1b: Schematic of experimental arrangement for isothermal reaction experiments. The substrate is held at a constant temperature (≥ 450 K) and, with the shutter closed to the solid doser for (MeCp)Ir(COD), is exposed to a steady input of $^{18}O_2$. When the surface saturates with ^{18}O, and the gas phase pressure of $^{18}O_2$ has stabilized, TOFMS data (1 to 450 amu is recorded for each 0.5 s interval) is taken for 60 s. Then, while continuing $^{18}O_2$ flow and gathering TOFMS data, the shutter is opened allowing a steady flux of (MeCp)Ir(COD) to impinge on the substrate. After gathering data for a selected time (210 – 60 = 150 s here), the shutter is turned off and data gathering continue for another period of time (20 to 30 s here). In this mode of operation, there are 500 data points collected for each mass between 1 and 450 amu.

2.3 EXPERIMENTAL

All experiments were performed in a standard ultrahigh vacuum chamber, base pressure ~ 2×10^{-10} Torr, equipped with time-of-flight mass spectrometery (TOFMS) [2.9] and AES. A Rh foil ($1 \times 1 \times 0.02$ cm^3) was mounted on a tungsten wire loop that connected to a liquid nitrogen reservoir through electrically isolated copper rods. The Rh was cleaned initially by a few cycles of sputtering (3 keV Ar^+, 500 K,10 min) and oxygen annealing (2×10^{-8} Torr O_2, 800 K, 5 min) followed by vacuum annealing at 1400 K for 2 min. The surface cleanliness was verified by AES.

(MeCp)Ir(COD) (Strem, >99%, $C_{14}H_{19}Ir$), formula weight 379.53 amu, was dosed without further purification through homemade solid doser (Figure 2.1a) that can reach as close as 3 cm in front of the sample surface while dosing. The (MeCp)Ir(COD) source was isolated by a gate valve in the dosing line. The precursor was loaded at least 24 hours before dosing to pump away volatile impurities. The dosing flux is mainly controlled by the size of pinhole in the source vessel. 2 hours before experiment, the doser is warmed to a selected temperature to obtain a desired flux. The precursor source vessel was kept at 295.5 ± 0.3 K during TPD dosing, at 310.0 ± 0.1 K during IRS dosing and 305.0 ± 0.1 K during oxygen co-dosed IRS. With no UHV surfaces at cryogenic temperatures, these conditions raised the chamber pressure to 1.0×10^{-9} torr, 2.4×10^{-9} torr and 2.0×10^{-9} respectively, and we take the ratio, 1:2.4:2.0, as the factor to use when comparing their dosing rates. To calculate the TPD dose in Langmuir, we used L = (1 x 10^{-6} torr x t) where t (s) is the dose time. During dosing, H_2O and CO also adsorb (Figure 2), but only in small amounts since the oxygen signal following a 10 min dose is undetectable in AES. To distinguish background H_2O and CO from reaction products, $^{18}O_2$ (Icon, > 99%) was used and dosed though a toggle leak valve.

TPD was performed from 100 to 950 K with a ramp rate of 2.5 K/s. The temperature was measured with a K-type thermocouple spot-welded to the back of the sample. Desorbed species were monitored by TOFMS, which acquired a full mass spectrum, with unit mass resolution, from 1 to 450 amu every 0.5 sec. The upper limit exceeds the 380 amu mass of (MeCp)Ir(COD) by the mass of a few oxygen atoms. Desorbed species were ionized by pulses of 70 eV electrons and monitored by the TOFMS, to provide a full 3D (mass, intensity, time) plot [2.9]. IRS, a central aspect of this work, was performed with the TOFMS and doser positioned symmetrically with respect to the sample normal (Figure 2.1b). The doser outlet and the detector inlet were both 3 cm from the center of the face of the sample, and the $^{18}O_2$ doser parallel to the sample surface. With the sample held isothermally at a pre-selected constant temperature, a constant precursor flux was delivered to the substrate and was turned on and off using a mechanical shutter at the doser outlet. Before, during and after IRS dosing, a full TOFMS spectrum was gathered every 0.5 s to monitor the time-dependent variation of all desorbed and reflected species. It is important to recognize that this TOFMS method misses no ions below the set upper mass limit and, thus, makes possible full and retrospective identification of species that are (and are not) desorbing. A similar 3D approach has been applied to the reaction with stainless steel of a common jet fuel additive [2.10]. In the results reported below, 3D data sets for 1 to 400 amu were thoroughly analyzed for contributions from a variety of species. This limits the analysis to monomers and smaller species that result from the reaction of ligands with oxygen. Rather than full 3D presentation, we focus on positively identified desorbed products.

The surface composition after TPD and IRS was determined by derivative mode AES. On a clean Rh surface, the Rh (MNN) peak at 302 eV has a signal-to-noise ratio of 27 ± 3. Taking account of the sensitivity factors (Rh:3.16 at 302 eV, Ir: 0.304 at 171 eV and C: 0.614 at 272 eV), Ir and C signal are not expected to be detectable unless their concentrations exceed 0.2 and 0.1 ML, respectively.

2.4 RESULTS AND ANALYSIS

2.4.1 TOFMS-TPD on a clean Rh surface

Illustrating the power of this TOFMS, Figure 2.2 shows a typical 3-dimensional (mass, temperature or time and intensity data set) taken after dosing (MeCp)Ir(COD) 100 K. Since every mass form 1 to 450 amu is probed, detailed

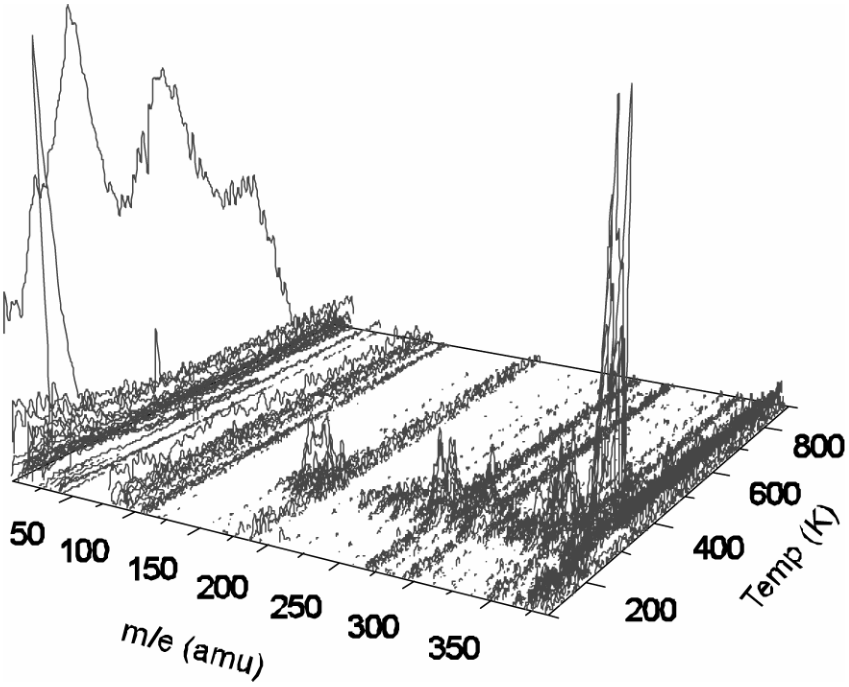

Figure 2.2: Three dimensional plot of m/e and T (in x-y plane) versus intensity along z-axis for TPD following 6 min dose of (MeCp)Ir(COD) on clean Rh at 100 K. Fourier filtering and uniform background intensity subtraction has been applied to all masses. The background subtraction was chosen to bring the region between 125 and 150 amu to zero. A background water desorption peak at 185 K has been subtracted.

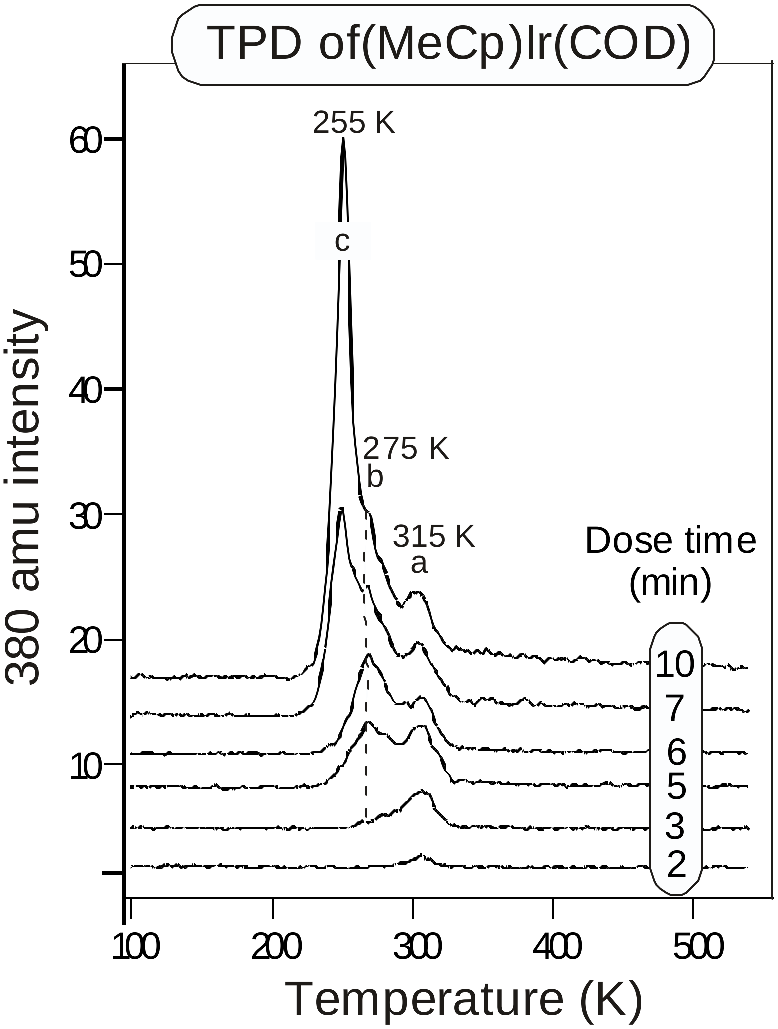

Figure 2.3: TPD spectra of 380 amu, $(MeCp)Ir(COD)^+$ for 6 dose times—10, 7, 6, 5, 3 and 2 min. The sample temperature was 100 K during dosing and the ramp rate was 2.5 K s^{-1}.

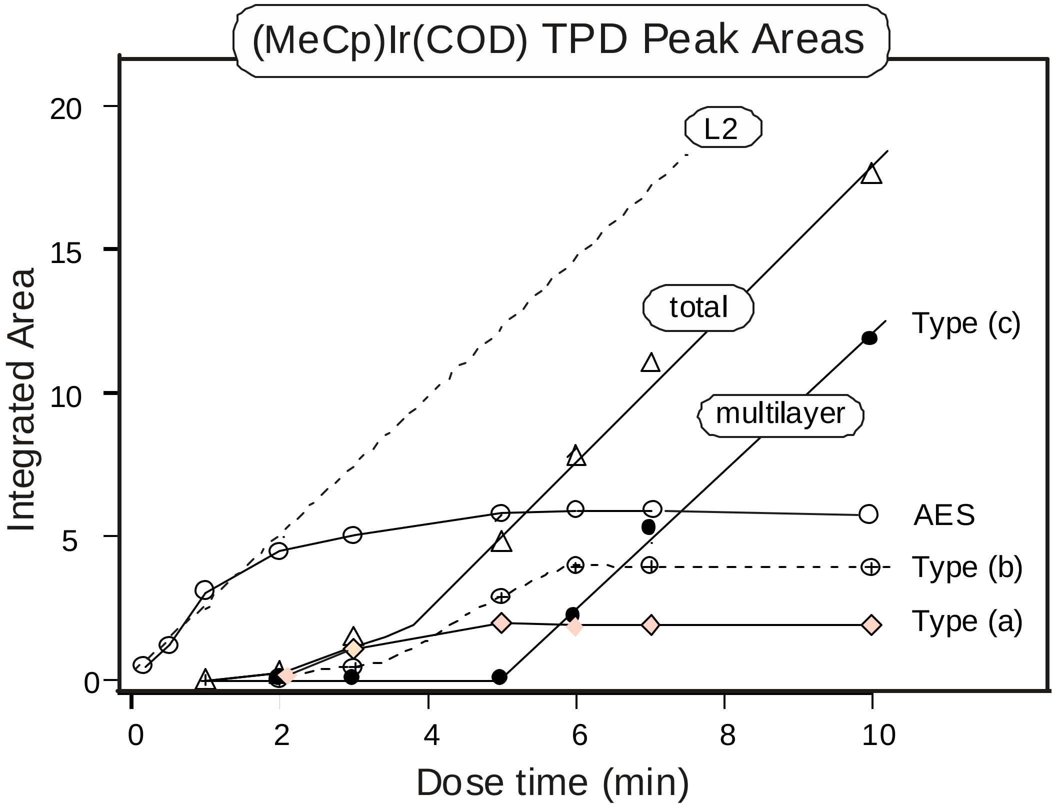

Figure 2.4: Total and decomposed (MeCp)Ir(COD)$^+$, 380 amu, peak areas as a function of dose time. Peak (c) is multilayer, (b) is (MeCp)Ir(COD) adsorbed in the presence of decomposition fragments without contact with Rh, and (a) is (MeCp)Ir(COD) adsorbed in the presence of Rh and dissociation fragments.

analysis of what does and does not desorb is possible; based on ion fragment analysis, the only desorption products are (MeCp)Ir(COD) and H_2. Strikingly, no hydrocarbons (CH_4, C_2H_4, and MeCp etc.) are found. After TPD, C is present in AES. In short, adsorbed (MeCp)Ir(COD) either desorbs intact or dissociates by breaking all the C-H bonds to form H_2 and retain C. This contrasts strongly with IRS results shown below where hydrocarbons desorb at least transiently.

In more detail, Figure 2.3 shows the TPD spectra of 380 amu, $(MeCp)Ir(COD)^+$, for various dose times on clean Rh. All other ion fragments, except H_2^+, show the same thermal profile. At very low doses (below 1 min), there is no parent desorption peak implying all adsorbed precursors decompose. With increasing dose, three peaks (a, b, and c) appear sequentially. The lowest, (c), at 255 K does not saturate and its leading edges are superimposable, a characteristic of zero-order desorption, showing that it is (MeCp)Ir(COD) multilayer desorption.

The integrated intensities of these three peaks are plotted as functions of dose time (Figure 2.4). Peak **a** (315 K) saturates at 5 min, peak **b** (275 K) saturates at 6 min and sets in before **a** saturates. Peak **c** sets in as **a** saturates and before **b** saturates. These facts indicate 3-dimensional island growth, not layer-by-layer growth, during dosing. Peak **c** is assigned to zero order multilayer desorption of (MeCp)Ir(COD) that interacts only with other (MeCp)Ir(COD), peak **b** is attributed to (MeCp)Ir(COD) that interacts with dissociation products and neighboring

(MeCp)Ir(COD), and peak **a** to (MeCp)Ir(COD) that interacts with the Rh substrate and dissociation products. In passing, note that describing peak **a** and peak **b** as first and second layer species could be misleading; the location and orientation of these species remains unknown [2.11].

The multilayer curve increases linearly at high dosage (> 6 min), reflecting a constant sticking coefficient at 100 K in the multilayer regime. The linear portion intersects the time axis at 5 min. If, for all dose times, the sticking coefficient were constant and there were no dissociative events, then the total (MeCp)Ir(COD) TPD would be a straight line (L2) through the origin with the same slope as the multilayer curve. With this assumption, the difference between L2 and the measured total (MeCp)Ir(COD) intensity provides an estimate of the fraction of the dosed (MeCp)Ir(COD) that dissociates at any exposure. For a 5 min dose there is negligible multilayer and $55 \pm 5\%$ is the estimated fraction that dissociates. At the same time, the C AES signal saturates. The (a)/(b) peak area ratio of desorbing (MeCp)Ir(COD) is 0.8 compared to the value of 0.5 at saturation, shown in Figure 2.4.

The H_2 TPD spectra (Figure 2.5) have up to four identifiable peaks reflecting stepwise ligand dehydrogenation as is typical for organic fragments on group VIII metals. With increasing dose the low temperature intensity diminishes while the higher temperature intensities increase. While the profile changes between 6 and 10 min, the total H_2 peak areas indicates saturation at 6 min, consistent with negligible dissociation for (MeCp)Ir(COD) located in the multilayer regime. For (MeCp)Ir(COD) doses exceeding 10 min the H_2 TPD intensity and thermal profiles no longer change.

Significant H_2 desorbs at temperatures lower than (MeCp)Ir(COD) desorption ($\leq$ 220 K) and can be accounted for as second-order recombination of H atoms attached to Rh [2.12]. This reaction channel is inhibited, but not eliminated, at higher doses, indicating that much of the C-H bond breaking occurs during TPD and that, as the dose (and total coverage) increase, fewer Rh sites are available to catalyze C-H cleavage.

Overall, the following H_2 desorption picture emerges. H(1) in Figure 2.5 is assigned to H atom recombination-limited desorption while the other features, H(2), H(3) and H(4) are assigned to desorption limited by C-H bond breaking from a variety of species in a variety of local chemical environments, i.e., a heterogeneous distribution of C-H bonds and environments. There is no H_2 desorbing above 800 K (vertical dashed line), a fact used to guide the IRS experiments.

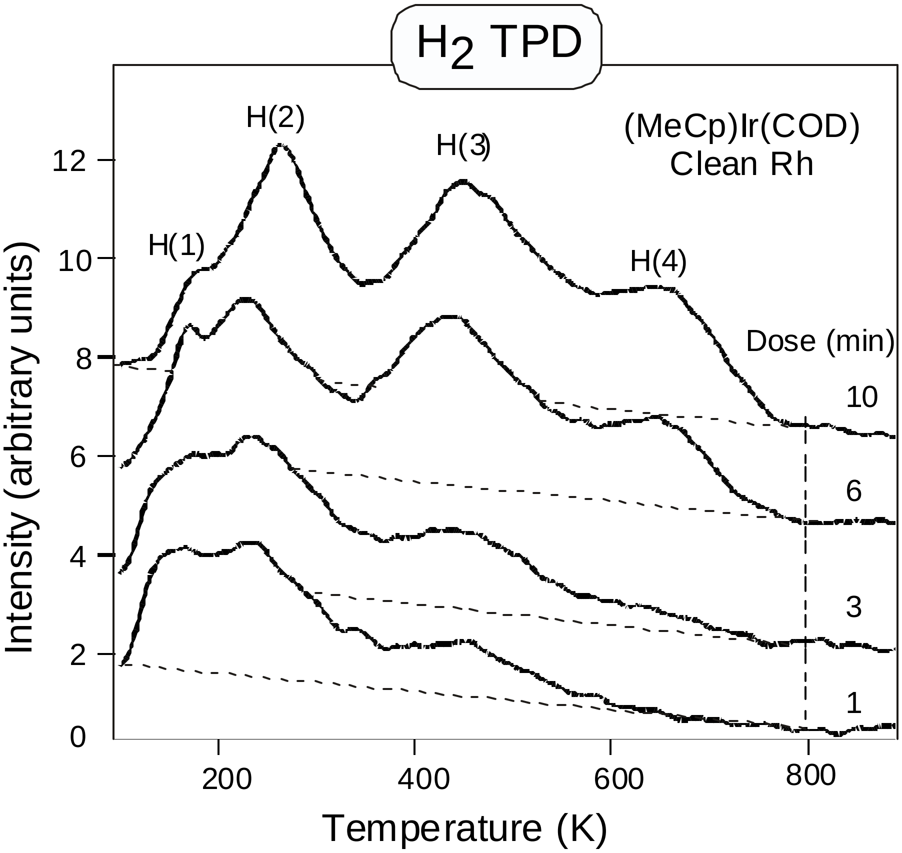

Figure 2.5: TPD of spectra of 2 amu, H_2^+, for 4 doses of (MeCp)Ir(COD) on Rh at 100 K. Ramp rate was 2.5 K s^{-1}.

2.4.2 TOFMS-TPD on an oxygen-covered Rh surface

On an ^{18}O pre-saturated Rh surface, (MeCp)Ir(COD) dosed at 100 K reacts during TPD (Figure 2.6) with oxygen atoms to form and desorb water, carbon dioxide and carbon monoxide, decomposes to release 1,3-cyclopentadiene and 1,5-cyclooctadiene, and dehydrogenates to release dihydrogen. Importantly, careful analysis of the 3D spectra reveals no partial oxidation products (aldehydes, ketones and alcohols) desorbing at any time. At 800 K, desorption ceases leaving surface carbon as measured, after cooling, by the C(KVV) AES signal at ~ 272 eV (not shown).

Figure 2.7 shows the TPD spectra of mass 380 for various exposures on ^{18}O-saturated Rh. All (MeCp)Ir(COD) fragments show the same pattern. At low coverage (< 0.07 L, 1 L = 1 x 10^{-6} Torr·sec), all the adsorbed precursors decompose, and there is no parent desorption peak. With increasing exposure, three peaks appear sequentially. The 255 K peak is again assigned to multilayer desorption. The 305 K peak is attributed to (MeCp)Ir(COD) that interacts with dissociation products and neighboring (MeCp)Ir(COD), and the 325 K peak to (MeCp)Ir(COD) that interacts with the Rh substrate and dissociation products. The monolayer desorption temperature is higher than that on a clean Rh surface, an observation attributed to interactions between oxygen and the π bonds of the organic ligands. The integrated intensities of these three peaks are plotted as the function of exposure (Figure 2.8).

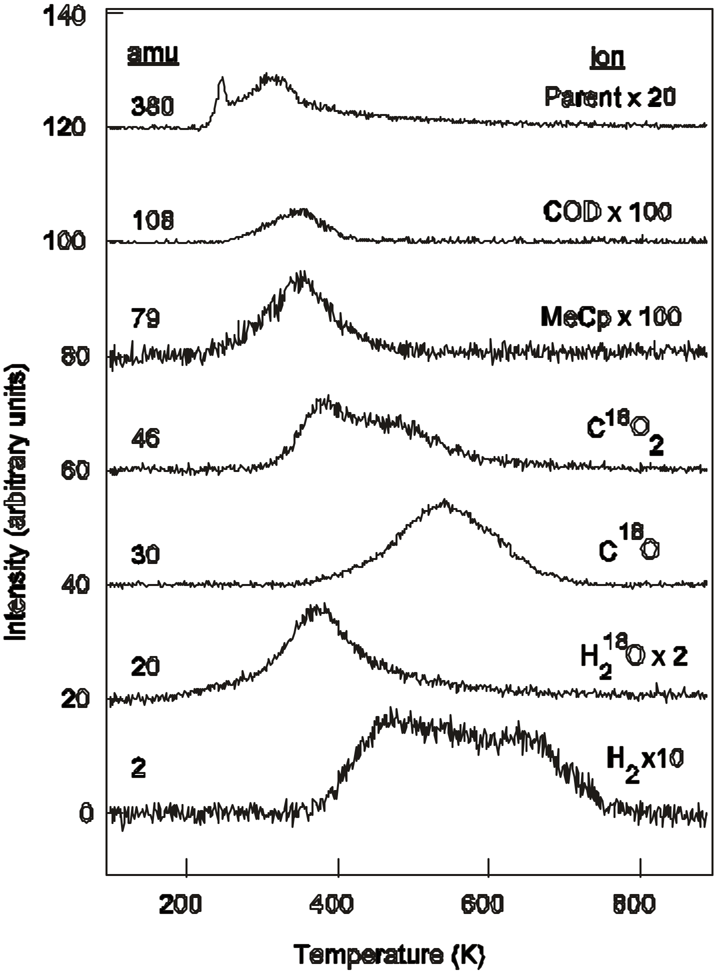

Figure 2.6: TPD spectra taken after dosing (MeCp)Ir(COD) at 100 K onto ^{18}O-saturated Rh foil. Masses to display were selected on the basis of expected desorbing species – (MeCp)Ir(COD) at 380 amu, COD at 108 amu, MeCp at 79 amu, $C^{18}O_2$ at 48 amu, $C^{18}O$ at 30 amu, $H_2{}^{18}O$ at 20 amu, and H_2 at 2 amu. Note that fragmentation patterns of (MeCp)Ir(COD) and COD contribute to 108 and 79 amu signals when multiple species are desorbing (see text).

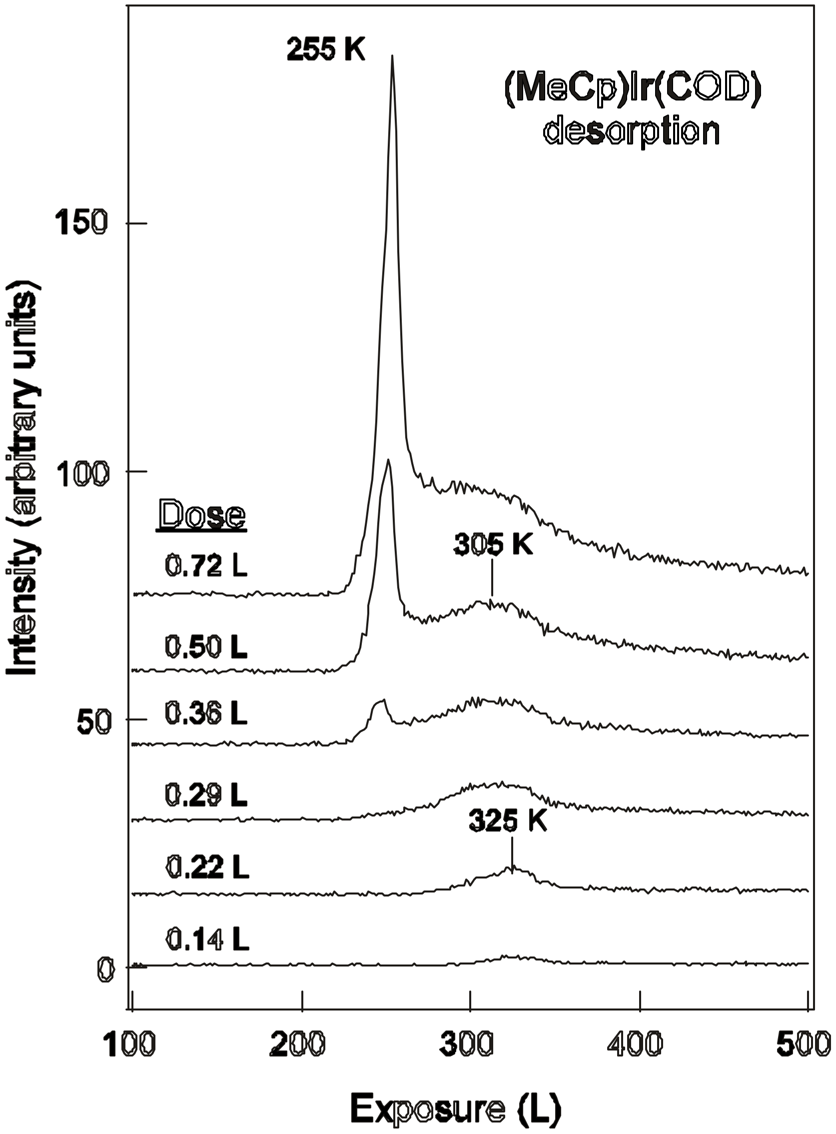

Figure 2.7: TPD spectra of 380 amu, (MeCp)Ir(COD)$^+$, for selected doses ranging from 0.14 to 0.72 L onto O-covered Rh foil at 100 K. One (1) L is defined as 10^{-6} Torr s where the uncalibrated pressure rise (?p = 1.2 x 10^{-9} Torr) measured with an ionization gauge. As noted in the experimental section, the actual dose is higher.

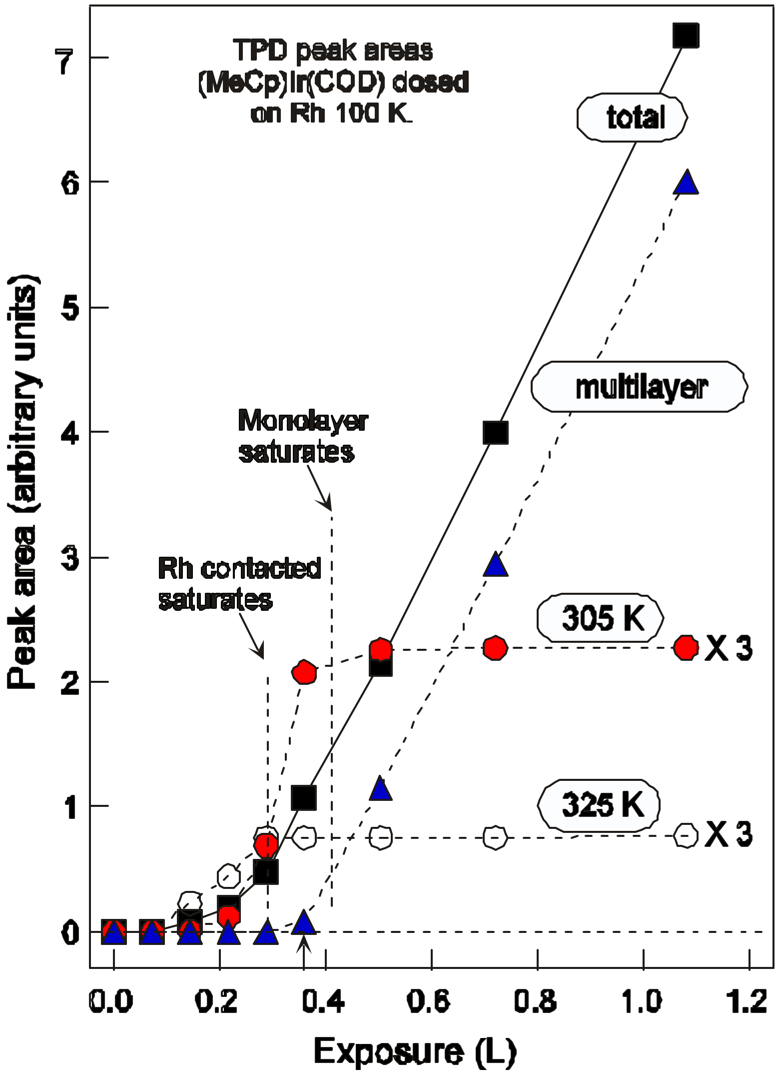

Figure 2.8: Peak areas of 380 amu TPD spectra as a function of the effective dose, calculated as the measured uncalibrated pressure rise ($\Delta p = 1.2 \times 10^{-9}$ Torr) multiplied by the dose time. Dose conditions are the same as those for figure 2.7. The total TPD area (squares) was decomposed into three separable contributions: molecules contacting Rh and dissociation products (325K, open circles), molecules contacting dissociation products and other molecules (305 K, filled circles), and unsaturable multilayer (triangles). The extrapolated onset of multilayer desorption occurs at 0.35 L. The 325 K peak contributions to $(MeCp)Ir(COD)^+$ do not appear until the dose exceed 0.15 L. The first peak area saturates at 0.3 L while the second peak saturates at 0.4 L.

Decomposition into three components is based on approximate fitting using symmetric approximations for all three peaks and assigning the 0.14 L spectrum entirely to the first peak. The first peak saturates at 0.29 L, and the second peak at 0.4 L. The multilayer peak appears slightly before the first layer saturates, suggesting that the adsorption of (MeCp)Ir(COD) at 100 K on Rh is not layer-by-layer. The precise growth mode remains undetermined.

The multilayer curve increases linearly at high exposures (> 0.4L), suggesting that the sticking coefficient of this precursor is constant at 100 K. The linear portion intersects the exposure axis at 0.35 L (recall that the actual dose in Langmuirs is higher). We define this as one monolayer (1 ML) coverage. Comparing the (MeCp)Ir(COD) intensity of a 1 ML increment (0.6 to 0.95 L) in the multilayer region to that of the initial 1 ML, we calculate that one-third of (MeCp)Ir(COD) that interacts with Rh remains intact after the exposure is more than 0.5 L. The saturated intensity of the first peak is only about one-third that of the second peak, i.e., more (MeCp)Ir(COD) decomposes on a clean surface and the dissociation products passivate the surface.

The 325 K peak has a tail extending up to 410 K (Figure 2.6 and Figure 2.7). Overlapping with this tail, there are also mass 108 and 79 desorptions (Figure 2.6), both peaking at 360 K, well above the 380 amu peak. These are assigned to a mixture of two different species: cyclooctadiene (COD, mass 108) and methylcyclopentadiene (MeCp, mass 79), on the basis of differing thermal profiles (79 amu is broader, particularly on its high temperature side) and fragmentation pattern analysis of the TOFMS extracted retrospectively from the data set. The relevant portion at 360 K is compared in Table 2.1 with standard fragmentation patterns of COD and MeCp. Clearly, neither MeCp nor COD dominates; rather, both contribute significantly (compare 79, 67, and 54 amu). At 360 K, where (MeCp)Ir(COD) contributions are negligible, all the 108, 93, and 67 amu intensity can be assigned to COD. Assuming both MeCp and COD have the same ionization cross section, the extracted MeCp/COD ratio is 1.3 ± 0.2, i.e., more MeCp than COD is desorbing.

Table 2.1: Fragment analysis at 360 K during TPD

Mass (amu)	108	93	80	79	77	67	65	54
MS at 360K	8	12	130	185	60	100	30	100
MeCp [2.13]	0	0	61	100	33	1	12	3
COD [2.13]	6	14	43	36	12	94	8	100

MeCp radical (C_6H_7) desorption is not involved since the mass 80 TPD shows exactly the same thermal profile as mass 79 (not shown). The variation with initial dose of the peak intensities of MeCp and COD increase with the same trend as that of the first desorption peak of the parent molecules (Figure 2.8). We conclude that only the (MeCp)Ir(COD) that contacts Rh contributes and MeCp and COD desorb when the initial dose is high enough to observe parent desorption. The lag of the peaks of MeCp and COD compared to the monolayer (MeCp)Ir(COD) peak shows this decomposition and desorption requires surface sites some of which are made available by parent desorption.

$H_2{}^{18}O$ is evolved at 380 K (Figure 2.6), much higher than the temperatures of molecular water desorption [2.14] and hydroxyl recombination [2.15] on Rh. Thus, the water formation and desorption is controlled by C—H bond cleavage. In other words, few C—H bonds are broken below 300 K, even though (MeCp)Ir(COD) decomposes.

Molecular hydrogen is evolved in a wide temperature region from 380 to 760 K. The leading edge of H_2 desorption overlaps with the falling edge of $H_2{}^{18}O$ desorption, suggesting that activated H atoms react with surface ^{18}O to form water, and only after most of the ^{18}O is consumed does H_2 formation become competitive.

Much of the available ^{18}O desorbs as $C^{18}O$ and $C^{18}O_2$ (Figure 2.6). $C^{18}O$ desorption has a peak at 550 K overlapping widely with the H_2 desorption. $C^{18}O_2$ is evolved in two reaction-limited peaks at 380 and 460 K. The first one matches the water desorption temperature, consistent with a model asserting that the first significant C—H bond cleavage occurs at 380 K. Both H_2 and $C^{18}O$ start to desorb as these water and carbon dioxide peaks are reached, suggesting a shortage of surface oxygen; as the ^{18}O concentration drops, $C^{18}O$ and H_2 desorption compete more and more favorably with $C^{18}O_2$ and $H_2{}^{18}O$ desorption. We speculate that the evolution of $C^{18}O_2$ at 460 K is not the product of $C^{18}O$ oxidation by ^{18}O and that one ^{18}O—C bond was formed within an organic functional group. The intermediate(s) were not identified. Since H_2 extends to higher temperatures than all other desorptions, C—H bonds remain to at least 750 K.

To summarize, (MeCp)Ir(COD) dosed on oxygen pre-saturated Rh at 100 K follows several reaction pathways in subsequent TPD: (1) desorption accompanied by decomposition to MeCp and COD, (2) O-enhanced dehydrogenation to form CO_2 and H_2O, (3) oxygen addition forming one or more organic oxygen-containing intermediates followed by decomposition to evolve CO_2, CO and H_2, (4) dehydrogenation of the products of steps (2) and (3) to form surface carbon and H_2. Identification of the surface bound intermediates awaits surface vibrational spectroscopy.

2.4.3 IRS of (MeCp)Ir(COD) without reactant gas from 350 to 750 K

IRS experiments were performed at 350, 550, 650 and 750 K. The TOFMS data included all masses from 1 to 400 amu. A full spectrum was collected every 0.5 s and involves both scattered incident (MeCp)Ir(COD) and desorbing reaction products. Analyzing the full data set, the following species were identified: H_2 and (MeCp)Ir(COD) as in TPD and, in addition, C_3H_4, COD, C_6H_6 and C_2H_4.

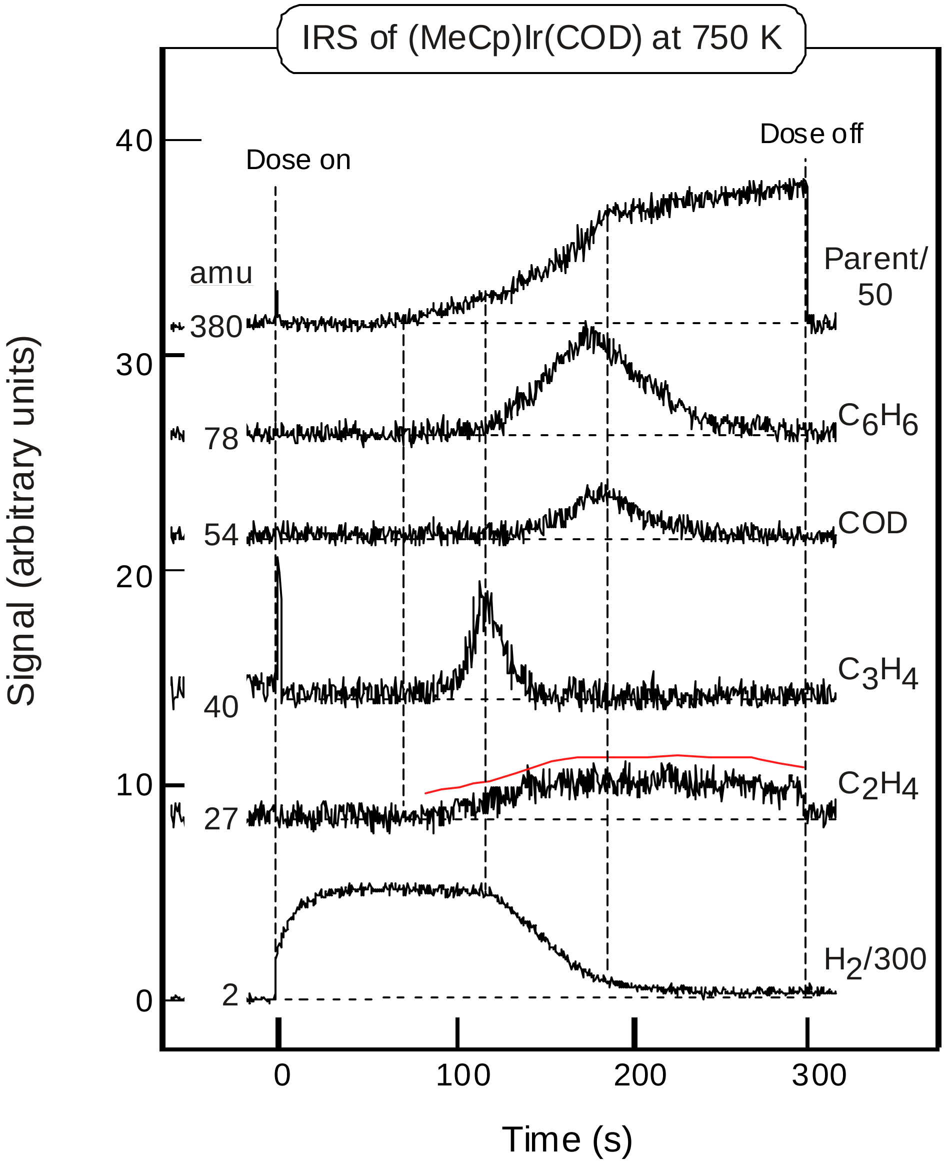

Figure 2.9: Isothermal reaction spectra (IRS) taken using geometry indicated in Figure 2.1b with the substrate at 750 K. The shutter was opened directing (MeCp)Ir(COD) to the substrate at t = 0 s. At 300 s, the shutter was closed and TOFMS spectra were taken for another 20 s. The noise-free curve associated with the 27 amu signal is a smoothed version of the raw data presented to show the slow decline between 250 and 300 s. Ion signals followed are indicated at the left side and the assignments on the right.

At 750 K, where H_2 evolution in TPD indicates that all C-H bonds are thermally activated, the time evolution of IRS characteristic signals of the above molecules, as monitored by the 2, 27, 40, 54, 78 and 380 amu signals, exhibit characteristics that reflect changes in the surface composition and structure during dosing (Figure 2.9). As noted in the Experimental section, the IRS dosing rate is 2.4 of the TPD dosing rate, i.e., in Figure 2.9, the 5 min (MeCp)Ir(COD) dose is equivalent to a 12 min dose (0.7 L) under TPD conditions. The time scale zero is set at the point where dosing commenced. Prior to dosing, i.e., left of the zero, the baseline signals are all constant. Dosing began with sharp narrow spikes in the (MeCp)Ir(COD) and C_3H_4 signals and, as expected, a sharp onset in the H_2 signal. The H_2 signal rises over a 20 to 30 s period, remains roughly constant for 100 s, then drops relatively rapidly and returning asymptotically to baseline levels by the time the doser is turned off at 300 s. In near mirror image fashion, the (MeCp)Ir(COD) remains negligible over the first 70 s, rises slowly to 120 s, accelerates between 120 and 190 s and then slowly monotonically rises over the remainder of the dose.

Clearly, the first (MeCp)Ir(COD) dosed dissociates, releasing some, but not all available H as H_2 while all the C and Ir are retained. Over the first 30 s, quasi-steady state is reached and rates of H loss and supply are balanced. Evidently, as further deposition occurs, the surface becomes less active as the surface composition changes. However, complete passivation is not reached at 300 s dose time; the ethene signal remains significant.

The transient 40, 54 and 78 amu signals that peak at different times—120, 180 and 190 s—and the rise, broad peak and slow decline of the 27 amu signal all provide insight. IRS at 650 K (not shown) also produces C_3H_4, COD, C_6H_6, and C_2H_4 but their maxima occur at earlier times that correlate with the decay of the H_2 signal and rising (MeCp)Ir(COD) at 650 K (see figures 2.10 and 2.11). The transient 40 amu signal may come from propyne and/or propadiene, and its appearance implies the occurrence of C—C and C—Ir bond cleavage involving one or both of the ligands on a partially passivated surface. From the cracking patterns, the 54 and 78 amu signals correspond to COD and C_6H_6, respectively. The COD transient is attributed to cleavage of the Lewis base type electron donor bonds between COD and Ir while the C_6H_6 is attributed, tentatively, to rearrangement of MeCp, e.g., no C—C bond breaking. The appearance of C_2H_4 desorption is striking. It commences as the Rh becomes cluttered with precursor fragments and continues well beyond the point where desorption of other dissociation products ceases. Apparently, there is a surface reaction with C-H and C-C rearrangement but not C-H bond breaking since C_2H_4 forms and desorbs but there is no H_2 desorption. Assuming this channel removes all the hydrogen in (MeCp)Ir(COD), $C_{14}H_{19}Ir$, implies that a film with average stoichiometry of C_4Ir is growing when deposition stops whereas the average is $C_{14}Ir$ at the outset. Further experiments are necessary to clarify that insignificant numbers of C-H bonds remain.

In a separate set of experiments, data were collected as a function of time for four set temperatures—350, 550, 650 and 750 K. The 380, $(MeCp)Ir(COD)^+$, and 2 (H_2^+) amu spectra were extracted, Figures 2.10 and 2.11. The doser was turned off earlier, 160 s compared to 300 s for Figure 2.9. Comparing the 750 K data for both cases indicates agreement except the dosing may have been slightly more rapid in Figure 2.9. For example, at 150 s, just as in Figure 2.9, COD, C_6H_6 and C_2H_4 are desorbing (not shown) and the H_2 signal is declining.

For comparison, an inactive surface (inactive for aftercoming molecules) was prepared and dosed with (MeCp)Ir(COD) at 275 K, curve I. An ideal inactive surface should have following characteristics: (1) an identical H_2 TPD pattern independent of subsequent dose; (2) an identical residual carbon intensity in AES after subsequent TPD; (3) no H_2 pressure variation during dosing; and (4) a nearly instantaneous rise and fall of the (MeCp)Ir(COD) ion signal in response to turning the doser on and off. To render the surface inactive, a clean Rh surface was dosed at 275 K with enough (MeCp)Ir(COD) to saturate peak (a) in Figure 2.3 and, after evacuation, the doser was turned back on while holding the sample at 275 K. This procedure adequately fulfilled the first two criteria above, but only partially the second two. The (MeCp)Ir(COD) signal rise requires ~ 20 s in part because there is some uptake into the low coverage regime of the physisorption isotherm, Figure 2.3. The H_2 signal exhibits a transient of about the same length presumably due to some displacement of H from sample or chamber surfaces. With these cautions, we take curve I of Figure 2.10 as a reasonable approximation of an inactive reference surface.

The other curves in Figure 2.10 correspond to isothermal reaction temperatures of: 350 (II), 550 (III), 650 (IV) and 750 K (V). The (MeCp)Ir(COD) signals lie at or below the inert reference and, at any time, t, the fractional difference, $(I_{ref} - I(t))/I_{ref}$, measures the total sticking coefficient, $S_t(t)$ for incident (MeCp)Ir(COD), e.g., when $I_{ref} - I(t) = 0$, all the incident (MeCp)Ir(COD) scatters without adsorption or reaction and $S_t = 0.0$. The resulting S_t curves are given in the insert of Figure 2.10. At both 350 and 550 K, $S_t(t)$ is unity initially, decays monotonically and supra-linearly, reaching zero, after the dose starts, at 80 s for 350 K and 90 s for 550 K. The situation at 650 and 750 K is qualitatively different. $S_t(t)$ remains large for a much longer period and does not drop to zero on the time scale of these experiments, indicating continuing overlayer growth. At 650 K, curve IV, there is a sharp kink near 110 s indicating a major slowing of passivation. Similar behavior occurs for 750 K but at dose times exceeding 150 s; the dashed curve is an extrapolation that would fit the longer time profile of Figure 2.9.

After dosing terminated, AES results (shown in parentheses in Figure 2.10) reflect varying C/Rh ratios—1.9 at 750 K, 1.5 at 650 K, 1.1 at 550 K and 0.9 at 350

K. After a longer exposure at 750 K (Figure 2.9) the C/Rh AES ratio was 2.9. For all these cases, the Ir AES signal was below noise levels. The increasing C/Rh ratio with substrate temperature, is clear evidence for more extensive dissociative precursor uptake and more extensive retention of carbon. At 750 K, the C/Rh ratio increases from 1.9 to 2.9 as the dose time increases from 150 to 240 s confirming sustained film growth with carbon retention. Keep in mind that C_2H_4 desorption appears after C accumulation and continues even when the C/Rh ratio reaches 2.9, i.e., there is a reaction at 750 K to form ethene on a surface that is dominated by C, but contains Ir.

The corresponding H_2 profiles are also helpful (Figure 2.11). As a monitor of the instrument response, the smooth curves are normalized versions of curve I of Figure 2.9. After dosing commences at 350 K and 550 K, the H_2 signal increases quickly, but not immediately to its maximum. After maximizing, the signal decays, reaching the background levels (curve I), at 115 s. At 650 K, the H_2 signal begins to drop sharply at 70 s but remains detectable at 150 s. At 750 K, the decay is much slower confirming that decomposition reactions continue as indicated in Figure 2.9.

Comparing the scaled versions of curve I from Figure 2.10 with the H_2 profiles, notice that the H_2 rises faster in every case confirming what we noted above; the inactive surface accumulates some molecular (MeCp)Ir(COD) in the early stages of dosing at 275 K. Further note that for 550, 650 and 750 K, the leading edges of the H_2 signals are all superimposable while at 350 K the leading edge rises slower and follows the rise of the inactive surface (I). Thus, for dosing on an inactive surface at 275 K and dosing on clean Rh at 350 K, there are processes operating that limit the onset slope of the H_2^+ signal. For the inactive surface (I), we attribute this to the same source that determines the rise of the (MeCp)Ir(COD)$^+$ signal—some parent physisorbs at the outset of dosing displacing some H as H_2. At 350 K, the situation is different; there is chemisorption with significant probability that it is not accompanied by H_2 evolution. As the temperature rises, we conclude that the initial delay, with respect to parent chemisorption, becomes shorter and limited only by the response time of the system. However, for all temperatures the maximum desorption rate of H_2 occurs 30 s or more after dosing commences. This reflects, as discussed above, a transient situation where the rate of decomposition of COD and MeCp fragments is slightly slower than the rate of their accumulation.

Evidence for accumulation of a sizable surface concentration of C-H containing material is provided by the behavior of the H_2^+ signal when dosing stops. The H_2^+ decay time is much longer (> 30 s) than the instrument response indicating the presence of C_xH_y that continues to evolve H_2 after the (MeCp)Ir(COD) signal has decayed to background levels.

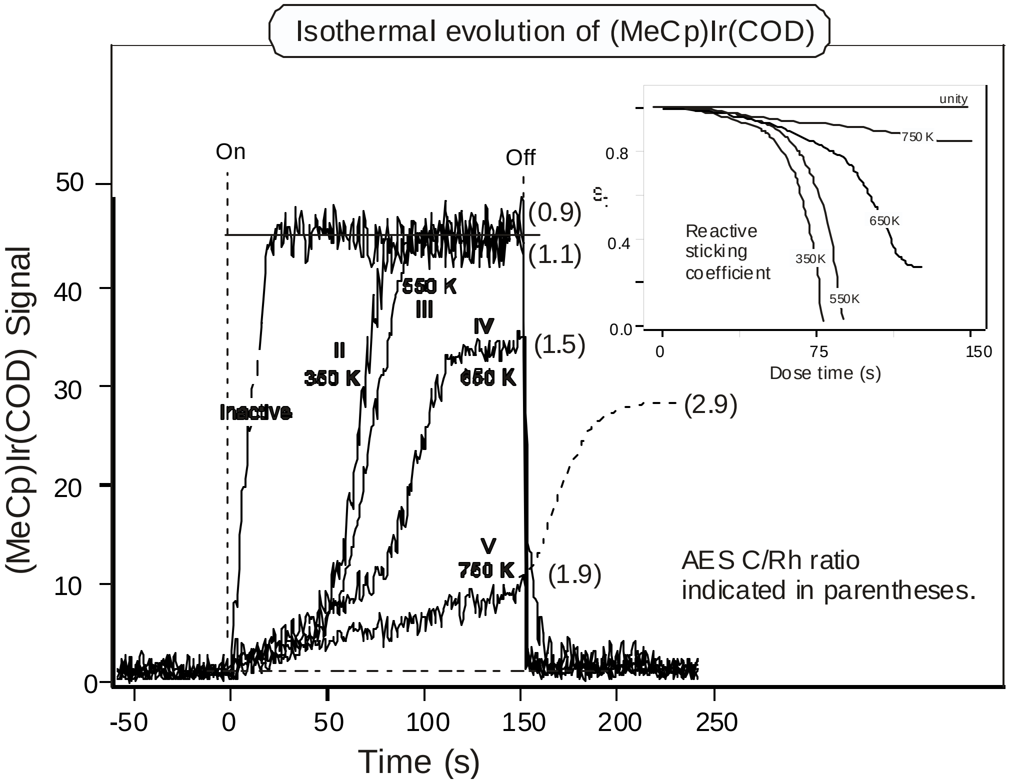

Figure 2.10: Variation of the (MeCp)Ir(COD) signal with dosing time for five dosing conditions: (I) an inactive surface, dosed at 275 K, II – V, a clean Rh surface dosed at 350, 550, 650 and 750 K. The dashed line shows the trend of the 750 K curve extended on the basis of Fig 2.9. AES C/Rh ratios are indicated in parentheses. The inset shows the total sticking coefficient, S_t, determined as described in the text from the (MeCp)Ir(COD)$^+$ profiles.

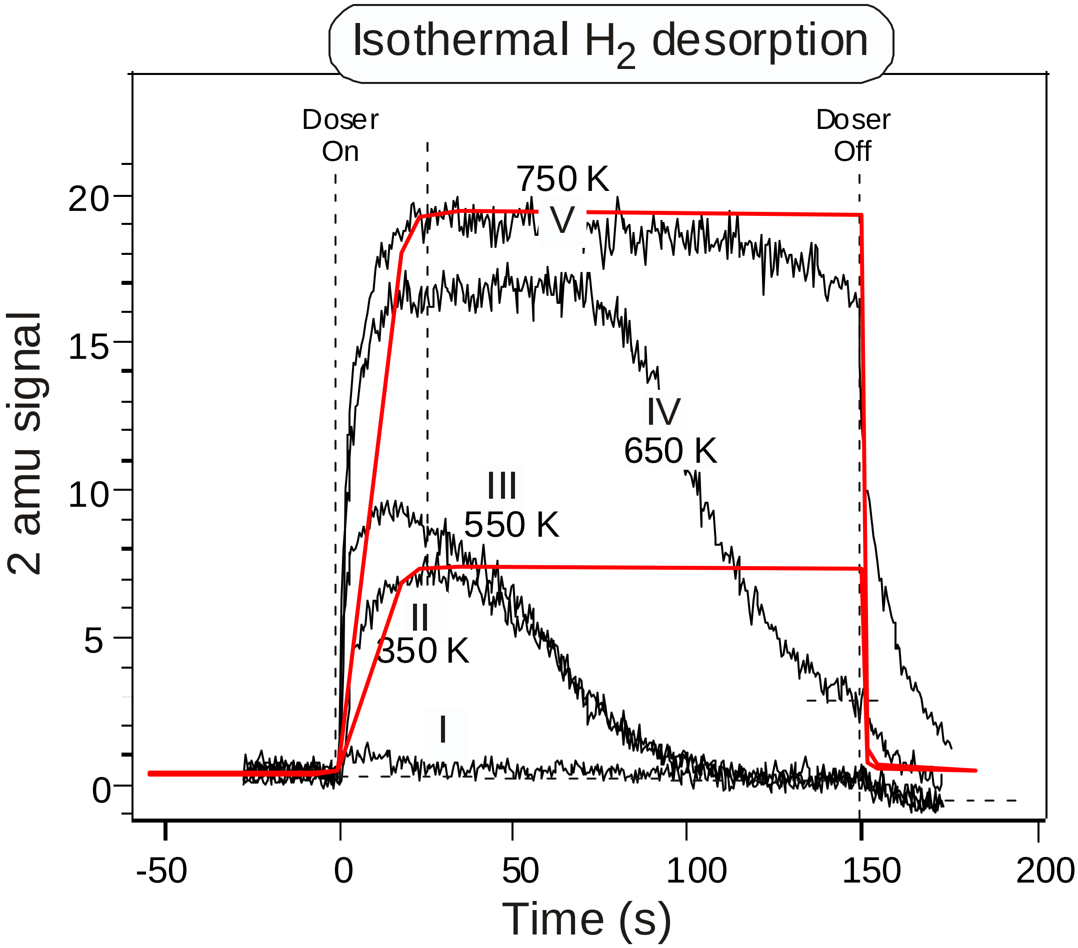

Figure 2.11: Variation of the H_2 signal with (MeCp)Ir(COD) dosing time for five initial conditions: (I) an inactive surface, dosed at 275 K, II – V, a clean Rh surface dosed at 350, 550, 650 and 750 K. The two noise-free curves are smoothed and scaled versions of curve I from figure 2.9 (see text).

2.4.3 IRS of (MeCp)Ir(COD) with co-reactant O_2 on oxygen saturated Rh

To simulate some aspects of Ir film deposition by metallorganic chemical vapor deposition (MOCVD), IRS spectra taken as (MeCp)Ir(COD) and variable amounts of $^{18}O_2$ were dosed on O-covered Rh were obtained at 600, 500 and 450 K. Between 1 and 450 amu, the TOFMS detected all scattered and desorbed species. Only $C^{18}O_2$, $C^{18}O$, and $H_2{}^{18}O$ desorbed; all other plausible desorbing species do not contribute detectable signals (< 0.5% of the combustion products). The carbon accumulated during IRS was determined by post-AES and depends strongly upon both the oxygen partial pressure and substrate temperature.

The real time variation of the measured ion signals attributable to (MeCp)Ir(COD), $C^{18}O_2$, $C^{18}O$, $H_2{}^{18}O$, $^{18}O_2$, H_2 are shown in Figure 2.12. The substrate temperature was 600 K, and the oxygen partial pressure 1.2×10^{-7} Torr. The dosing shutter, initially closed for $t < 0$, was opened at 0 sec, and reclosed at 150 sec. The parent ion signal has a brief spike at 5 s before returning to zero, the latter indicts that all adsorbed (MeCp)Ir(COD) decomposes. The reaction products—$C^{18}O_2$, $C^{18}O$, $H_2{}^{18}O$, and not others—demonstrate that throughout the (MeCp)Ir(COD) dosing interval, combustion and oxydehydrogenation, i.e., hydrogen is consumed by oxygen, reactions prevail. The constant non-zero signal intensities of all products and $^{18}O_2$ after 50 sec reflects steady-state conditions and shows that

(MeCp)Ir(COD) continuously decomposes, that Ir deposits steadily, and that the organic ligands are removed as $C^{18}O_2$, $C^{18}O$ and $H_2{}^{18}O$.

If steady-state Ir film growth were realized immediately, then the $^{18}O_2$, $C^{18}O_2$, $C^{18}O$ and $H_2{}^{18}O$ curves would rise promptly to their maximum values that would be delayed no longer than the transient spike in the (MeCp)Ir(COD) signal (~ 5 s). None of the product peaks maximizes on this time scale indicating that downward adjustment of the initially high surface concentration of O is required to reach steady-state. The $C^{18}O_2$ rises sharply to its maximum at 15 s and then drops to steady-state at 30 s. The $^{18}O_2$ signal exhibits a very sharp drop in the first 5 s followed by a steady decline to steady-state at 50 s. The $H_2{}^{18}O$ rises steadily, also reaching steady-state at 50 s. $C^{18}O$ has features that mimic the other three products.

When the doser is closed at 150 s, the parent signal does not change confirming that all incident (MeCp)Ir(COD) reacts with the growing surface. Neither does the H_2 signal change confirming that no H_2 signal above background is involved. The other four signals respond promptly. Except for $H_2{}^{18}O$, all return to baseline in 15 s. Water decays somewhat more slowly, an observation attributed to the relatively slow removal of $H_2{}^{18}O$ from the chamber walls.

The relatively small $^{18}O_2$ signal drop at 0 sec implies, as expected, that the reaction of (MeCp)Ir(COD) with oxygen is a surface, not a gas phase, reaction under these conditions. At the instant the doser is opened, the surface is saturated by ^{18}O, and the $^{18}O_2$ sticking coefficient is zero. Rapidly though, (MeCp)Ir(COD) decomposes consuming ^{18}O, desorbing products and creating sites for further $^{18}O_2$ dissociation thus reducing the $^{18}O_2$ partial pressure. When ^{18}O consumption and adsorption become equal, the gas phase $^{18}O_2$ signal becomes steady. There is a small (MeCp)Ir(COD) spike at the outset of dosing that we take as reflecting a small pressure pulse when the doser is turned on. Certainly beyond that, the adsorption/reaction probability of (MeCp)Ir(COD) is always unity. Under the IRS conditions used here, the rate of $^{18}O_2$ dissociation is always more than sufficient to consume the C and H that arrives with (MeCp)Ir(COD). The early small peak of $C^{18}O_2$ is due to the saturation ^{18}O coverage at the instant (MeCp)Ir(COD) dosing commences, i.e., the initial chemical potential of O is higher than that realized at steady state. At the beginning, the surface oxygen coverage is high, and $C^{18}O_2$ is favorable; as the reaction proceeds, $C^{18}O_2$ decreases with the decreasing of surface oxygen coverage, and $C^{18}O$ increases. AES after film growth reveals pure Ir deposition with no detectable impurities.

The IRS results at 500 K are very similar to those at 600 K (not shown): all impinging (MeCp)Ir(COD) molecules decompose up to 150 sec, and no carbon (Table 2.2) is left on the surface when oxygen partial pressure is higher than 1.2×10^{-7} Torr. When the pressure of $^{18}O_2$ is lower, carbon does accumulate as measured by the C/Rh AES ratio (Table 2.2).

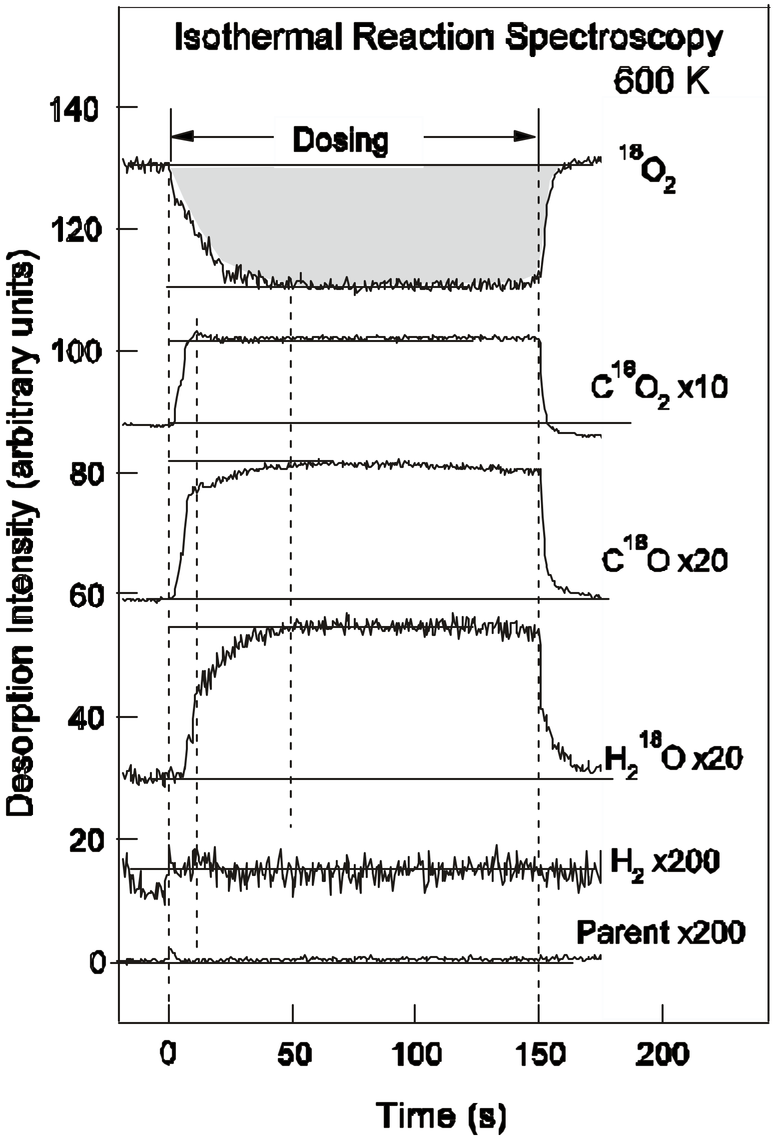

Figure 2.12: Isothermal reaction spectra (IRS) taken as indicated in Figure 2.1b with the substrate at 600 K. For 60 s prior to t = 0 s, TOFMS spectra were taken with 1.2 x 10^{-7} Torr of $^{18}O_2$ flowing. Then the shutter was opened directing (MeCp)Ir(COD) to the substrate while monitoring, with 0.5 s time resolution, every mass from 1 to 450 amu. The precursor doser was preset to give a pressure rise of 2 x 10^{-9} Torr. At 150 s total elapsed time, the shutter was closed and TOFMS spectra were taken for another 20 s. Masses to display were taken on the basis of analyzing the full spectra for peaks that rose and fell when the shutter was opened.

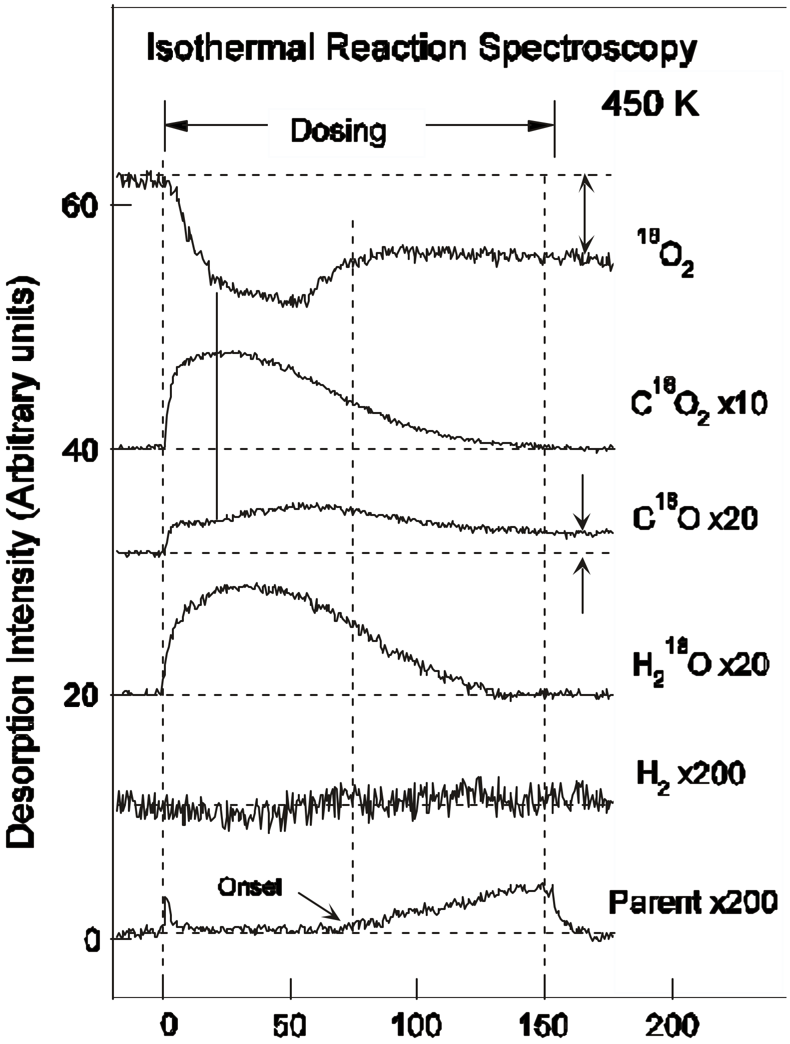

Figure 2.13: Isothermal reaction spectra (IRS) taken as indicated in Figure 2.1b with the substrate at 450 K. For 60 s prior to t = 0 s, TOFMS spectra were taken with 1.2 x 10^{-7} Torr of $^{18}O_2$ flowing. Then the shutter was opened directing (MeCp)Ir(COD) to the substrate. The precursor pressure was 2 x 10^{-9} Torr. At 150 s total elapsed time, the shutter was closed and TOFMS spectra were taken for another 20 s. See caption of figure 5 for more details.

Table 2.2: Variation of carbon content with oxygen partial pressure

P_{O2} (10^{-7} Torr)	0	0.4	0.8	1.0	1.2	1.4
AES peak ratio C(272 eV)/Rh(302 eV)	0.72	0.35	0.11	0.04	0.00	0.00

During dosing, the partial pressure of (MeCp)Ir(COD) is about 2 x 10^{-9} Torr. Thus, a pure Ir film can be obtained only if the oxygen-to-precursor ratio exceeds about 60. This exceeds the stoichiometric ratio (23.5 to 1) required for full combustion to CO_2 and H_2O. As indicated in Figure 2.12, complete oxidation is not realized; carbon monoxide makes a major contribution to the steady-state rate of reaction.

It is reasonable to suppose that adsorption of both reactants, (MeCp)Ir(COD) and $^{18}O_2$, is required and that dissociative adsorption of $^{18}O_2$ is essential. At 500 K, the dissociative sticking coefficient of O_2 on a clean Rh foil is between 0.3 and 0.4, and it drops to less than 0.1 as the coverage approaches 0.5 O per surface Rh atom [2.16]. The sticking coefficient of (MeCp)Ir(COD) on both clean [2.17] and O-saturated surfaces is unity at 500 K. Thus, the relatively large excess of $^{18}O_2$ required to consume the ligands is attributable the relatively low $^{18}O_2$ dissociative sticking coefficient.

IRS taken with the substrate held at 450 K (Figure 2.13) differs qualitatively from that taken at 600 K. Most importantly, full steady-state is not reached for any period of time during dosing. The (MeCp)Ir(COD) signal is characterized by an initial sharp spike followed by a negligibly small signal to about 15 s, and then a steady rise to 90 s. The negligibly small signal to 15 s indicates that all the inbound (MeCp)Ir(COD) is being adsorbed whereas the steadily rising signal between 15 and 150 s indicates the sticking coefficient is dropping steadily below unity. The $^{18}O_2$ signal drops steadily after dosing begins, reaches a minimum, and then rises to a steady value.

The oxidation products – water, carbon monoxide and carbon dioxide – all rise sharply, exhibit local maxima at different times, and then decay steadily. The $H_2{}^{18}O$ signal drops to zero at about 130 s, the $C^{18}O_2$ signal drops to zero about 150 s, and the $C^{18}O$ signal drops but remains well above zero at 150 s where the dose is terminated. The H_2 signal does not change when dosing begins and drifts slowly throughout. It is important to note that when the (MeCp)Ir(COD) is terminated at 150 s while continuing $^{18}O_2$ exposure, the only TOFMS signals that change are those that monitor (MeCp)Ir(COD) being scattered from the surface. These results show that, by 150 s, the rate of (MeCp)Ir(COD) reaction and the rates of $C^{18}O_2$ and $H_2{}^{18}O$ production have become negligible, that the $^{18}O_2$ consumption rate has slowed compared to the 0 to 50 s period, and that the $C^{18}O$ production rate continues uninterrupted when (MeCp)Ir(COD) dosing stops. In retrospective analysis of the TOFMS data set, there is no evidence for desorption of any other products.

In important complementary experiments (not shown), AES analysis after stopping $^{18}O_2$ flow and cooling to 300 K, shows strong C and O AES signals mixed with Ir and Rh. In subsequent TPD to 900 K, significant amounts of $C^{18}O$, $H_2{}^{18}O$ and H_2 desorb. After TPD, C, but no O, appears in the AES spectrum.

The qualitative picture emerging for the 450 K IRS experiment is that, on the O-rich starting surface, the oxygen activity is high enough to dissociate all the incident (MeCp)Ir(COD) but complete ligand removal as oxidation products does not occur. Under these conditions, dissociated (MeCp)Ir(COD) forms C-, O- and H-containing fragments, i.e., partially oxidized moieties, that are not competitively removed compared to the rate of dissociative $^{18}O_2$ adsorption. As a result, dissociative adsorption slows, the Rh sites become saturated and, speculatively, dissociative $^{18}O_2$ adsorption becomes limited by the rate at which oxidation reactions provide Ir in the form of atoms or small clusters that are not fully coordinated and can serve to dissociate both $^{18}O_2$ and (MeCp)Ir(COD).

In a more extensive analysis of Figure 2.13, note that the $^{18}O_2$ and $C^{18}O$ signals both exhibit slope changes at 15 s; the rate of carbon monoxide production and the rate of oxygen consumption both increase. At the same time, the $C^{18}O_2$ signal reaches its maximum. These features signal a reaction path change, and by inference a structural change, that we attribute to the formation of an O-deficient, relatively inactive, C-rich overlayer. This overlayer oxidizes slowly at a rate controlled by the rate of $^{18}O_2$ dissociation. Under these conditions, Rh atoms become passivated, the dissociation of $^{18}O_2$ is controlled by the availability of Ir sites, and the chemical potential of oxygen drops. As the chemical potential of oxygen drops, oxidation of carbon to CO becomes favored over oxidation to CO_2, as observed.

2.5 DISCUSSION

From these results, the following general picture emerges. Based on TPD, (MeCp)Ir(COD) adsorbs on clean Rh at 100 K and accumulates without saturation to multilayer amounts. Since the initial sticking coefficient is unity at 350 K, Figure 2.10, we assume this initial value holds at lower temperatures as well and, further, at 100 K remains unity for all dosing times. Above 300 K, clean Rh surfaces readily activate the chemisorption and decomposition of (MeCp)Ir(COD), a process occurring transiently with strong temperature dependent characteristics. The transient decaying activity revealed in the IRS results is attributed to passivation of Rh with C-containing fragments. While the Ir was not detected, we infer that initially Ir/C = 1/14, the precursor stoichiometry, is deposited and that this ratio increases as carbon atoms are removed in the form of various hydrocarbons, Figure 2.9.

Between 350 and 550 K, the transients are short-lived and the sticking coefficient of (MeCp)Ir(COD) drops to zero, indicating that Rh sites are rapidly passivated and that thermal energy is insufficient to open other reaction channels even though Ir is present and, as in cluster forms, is active for C-H and C-C bond breaking [2.18]. At 650 and 750 K, the transients are much longer and, at 750 K, are sustainable for times longer than those pursued in these experiments, presumably because the combination of thermal energy and the presence of Ir in the growing film is sufficient to sustain surface decomposition.

Keeping in mind the UHV nature of our work, there is nevertheless an interesting comparison with gas phase pyrolysis experiments; sustained film growth sets in between 650 and 750 K in our experiments while gas phase pyrolysis sets in at 680 K releasing COD and C_6H_6 [2.2, 2.3]. No C_3H_4 or C_2H_4 were observed. The difference implies, not surprisingly, that the surface plays some role in determining the detail of competition among reaction paths. Further there is clear evidence that these reaction paths change as the composition and structure of the surface change.

The fact that H_2 pressures neither rise to maximum values as soon as dosing starts nor fall to the background level as soon as dosing stops, shows that H_2 comes from not only the prompt decomposition of (MeCp)Ir(COD) but also the dehydrogenation of the accumulated hydrocarbon fragments. As the substrate temperature increases from 350 to 750 K, the initial H_2 rise becomes sharper and more intense, reflecting faster and more extensive C-H bond breaking.

The transient character of the formation of C_3H_4, C_6H_6, COD and, presumably, C_2H_4, is very interesting. For any temperature used here, the clean Rh surface activity for C-Rh bond formation and C-H bond breaking is high enough to inhibit formation and/or desorption of adsorbed hydrocarbons. As the Rh is passivated by partially decomposed (MeCp)Ir(COD), the surface composition changes and, at 650 and 750 K, compositions and structures exist transiently that make hydrocarbon desorptions compete with other reaction channels. It would be interesting to quickly switch from (MeCp)Ir(COD) to COD dosing at, for example, 170 s in Figure 2.9 and determine what hydrocarbons desorbed and whether reactivity was sustained.

Irrespective of substrate temperature, S_t is unity initially and decreases with dose as C-containing fragments accumulate. The decrease is, according to Figure 2.9, in a transition region where the products observed at no other time emerge and decay. At 350 K and 550 K, S_t decreases to zero while at 650 and 750 K it decays from unity but stabilizes at intermediate values. This occurs even though the C/Rh ratio is lower than for the higher temperature experiments (Figure 2.10). While we intuitively attribute this to the thermal activation of polymerized C_xH_y resembling in some respects amorphous hydrogenated carbon [2.19], the extent to which these differences are due to the presence of Ir mixed with C, or to other structural/compositional factors remains an open question.

While elucidating the details of reaction paths and their changes is not possible from these measurements, the following comments and observations are germane. On Rh(111), Cp exists in an η^5-hapto form up to 420K where the ring opens [2.20]. A similar species may contribute in the initial stages of our experiments, i.e., chemisorption and TPD involve transfer of MeCp from Ir to Rh. The other ligand, 1,5-COD when dosed on Pt(111), dehydrogenates to cyclooctatetrene (COT) between 325-375 K. COT dehydrogenates to form pentalene which forms surface bound C and H_2(g) above 500 K [2.21-2.23]. Since Pt and Rh exhibit comparable hydrogenation and dehydrogenation tendencies, it is reasonable to suppose that a similar process contributes to our high temperature hydrogen evolution (Figure 2.5, 2.9 and 2.11).

Other dehydrogenation pathways must also participate in order to account for the variation of the H_2 TPD intensities with dose (Figure 2.5) and for the transient hydrocarbon desorptions in IRS (Figure 2.9). We speculate that C_3H_4 comes from the decomposition of COD since COD starts to desorb when C_3H_4 desorption almost finishes. The formation of C_6H_6 could come from the rearrangement of either MeCp or COD. The formation of C_2H_4 beginning as the activity of Rh becomes negligible and continuing as the C content increases emerges as one of the most interesting findings of this study. The incident precursor—stoichiometry, C_8H_{12}—is H-deficient with respect to the formation of saturated or unsaturated C_2 species and grows even more deficient with any H_2 evolution, but as H_2 evolution slows reflecting reduced C-H bond breaking activity, the opportunity for removing hydrocarbons becomes more likely provided there is an open reaction channel. We speculate that (MeCp)Ir(COD) incident at 750 K on a surface relatively inactive for C-H bond breaking rearranges to form C clusters containing Ir and removes the H in the form of a good leaving species, C_2H_4.

With regard to film growth, these results complement previous work [2.2]; only very thin films (1.5 nm) containing 87% carbon were deposited at 770 K on SiO_2 in 30 min. On Rh, passivation occurred below 650 K. Deposition of films or particles by chemical vapor deposition can be motivated by different technological objectives. In microelectronics, for example, conformal deposition on high aspect ratio integrated circuit features is desirable to form electrodes. A small but stable S_t is required to deposit a conformal film in a reasonable time period [2.24]. This cannot be satisfied by this precursor alone—the slope of S_t is too steep around S_t = 0.1 and C incorporation is troublesome.

2.6 SUMMARY AND CONCLUSIONS

(MeCp)Ir(COD) adsorbs in 3-dimensional islands on both clean and oxygen saturated Rh surfaces. Three (MeCp)Ir(COD) desorption peaks are found and assigned to multilayer (255 K), adsorbed with decomposed (MeCp)Ir(COD) (275 K on clean Rh and 305 K on O-saturated Rh), and adsorbed in contact with Rh and decomposition products (315 K on clean Rh and 325 K on O-saturated Rh).

During TPD after dosing (MeCp)Ir(COD) onto a clean polycrystalline Rh foil at 100 K, the only desorption species are (MeCp)Ir(COD) and H_2 that appears in up to four dehydrogenation steps. Carbon forms and remains up to 1000 K. On an O-saturated Rh surface, (MeCp)Ir(COD) adsorbs molecularly and reactively in coverage-dependent amounts. In subsequent TPD, (MeCp)Ir(COD) desorbs at 325 K accompanied by its decomposition to MeCp and COD. Reactions with adsorbed O lead to formation and desorption of CO_2 and H_2O and surface-bound intermediates involving oxygen. These intermediates decompose as the temperature rises and CO_2, CO and H2 desorb. After TPD to 850 K, only surface carbon remains.

Isothermal reaction spectroscopy (IRS) of (MeCp)Ir(COD) without reactant gas shows that (MeCp)Ir(COD) decomposition on Rh follows different coverage- and composition-dependent pathways depending on the carbon and iridium content of the film grown over Rh. These paths include non-selective bond breaking catalyzed by Rh and selective formation of C_3H_4, C_6H_6 and C_2H_4 for a high temperature (≥ 650 K) dose onto surfaces covered with enough C and the accompanying Ir, to make the underlying Rh largely inaccessible to incident (MeCp)Ir(COD). IRS results, when compared to the response of an inactive surface, lead to calculated dissociative sticking coefficients ranging from unity on clean Rh to 0.0 for passivated Rh held at 350 or 550 K. At 750 K, the sticking coefficient remains at 0.8 even though the C/Rh ratio rises to as high as 2.9.

IRS experiments involving simultaneous dosing of (MeCp)Ir(COD) and O_2 reveal that the minimum temperature and oxygen partial pressure to grow a pure Ir film are 500 K and 1.2×10^{-7} Torr (with (MeCp)Ir(COD) pressure 2×10^{-9} Torr). When the substrate is above this temperature, steady state combustion occurs, CO_2, CO and H_2O desorb, and Ir is deposited. When the substrate temperature is 450 K, the organic ligands cannot be totally removed and carbon incorporates in the deposited film.

2.7 REFERENCES

[2.1] Hoke, J. B.; Stern, E. W.; Murray, H. *H. J. Mater. Chem.* **1991**, 1, 551

[2.2] Sun, Y.-M.; Yan, X.-M.; Mettlach, N.; Endle, J. P.; Kirsch, P. D.; Ekerdt, J. G.; Madhukar, S.; Hance, R. L.; White, J. M. *J. Vac. Sci. Technol. A* **2000**, 18, 10

[2.3] Endle, J. P.; Sun, Y.-M.; Nguyen, N.; Madhukar, S.; Hance, R. L.; White, J. M.; Ekerdt, J. G. *Thin Solid Films* **2001**, 388(1,2), 126

[2.4] Yao, Y-F. Y. *J. Catal.* **1984**, 87, 152

[2.5] Xu, X.; Friend, C. M. *J. Am. Chem. Soc*. **1991**, 113, 6779

[2.6] Xu, X.; Friend, C. M. *J. Phys. Chem.* 1991, 95, 10753

[2.7] Guo, X.; Madix, R. J. *ACS Symp. Ser.* **1996**, 638, 357

[2.8] Harris, T. D.; Madix, R. J. *J. Catal.* **1998**, 178, 520

[2.9] Kim, C.; Yan, X.-M.; White, J. M. *Rev. Sci. Inst*. **2000**, 71, 3502

[2.10] Chusuei, C. C.; Morris, R. E.; Schreifels, J. A. *Appl. Surf. Sci.* **1999**,153, 23

[2.11] Yan, X.-M.; Kim, C.; White, J. M. *Thin Solid Films* **2001**, 391(1), 62

[2.12] Payne, S.H.; Kreuzer, H.J.; Frie, W.; Heinz, K. *Surf. Sci.* **1999, 279**, 421

[2.13] NIST website chemistry book, http://webbook.nist.gov/chemistry

[2.14] Wagner, F. T.; Moylan, T. E.; *Surf. Sci.* **1987,** 191, 121

[2.15] Gregoratti, L.; Baraldi, A.; Dhanak, V. R.; Comeli, G.; Kiskinova , M.; Roser, R. *Surf. Sci.* **1995**, 340, 205

[2.16] Nehasil, V.; Stara, I.; Matolin, V. *Surf. Sci*. **1997**, 377-379, 813

[2.17] Yan, X.-M.; Kim, C.; White, J. M. *J. Vac. Sci. Technol. A* **2001,** 19(5),2629

[2.18] Kua, J.; Faglion, F.; Goddard III, W. A. *J. Am. Chem. Soc*. **2000**, 122, 2309

[2.19] Schenk, A.; Winter, B.; Biener, J.; Lutterloh, C.; Schubert, U. A.; Kuppers, J. *J. Appl. Phys.* **1995, 77**, *2462*

[2.20] Netzer, F. P.; Goldmann, A.; Rosira, G.; Bertel, E. *Surf. Sci*. **1988**, 204, 387

[2.21] Hostetler, M. J.; Dubois, L. H.; Nuzzzo, R. G.; Girolami, G. S. *J. Am. Chem. Soc.* **1993,** 115, *2044*

[2.22] Hostetler, M. J.; Nozzo, R. G.; Girolami, G. S.; Dubois, L. H. *J. Phys. Chem.* **1994,** 98, *2952*

[2.23] Manner, W. L.; Dubois, L. H.; Girolami, G. S.; Nuzzo, R. G.; *J. Phys. Chem.* **1998**, 102, *2391*

[2.24] Park, S.-K.; Yun, T.-H.; Rhee, S.-W. *Proc. Electrochem. Soc.* **1993**, 93(2), *64*

This page is intentionally left blank

Chaper3: *tert*-Butyl nitrite (TBN) thermal decomposition on Cu(111) and Rh surfaces

3.1 OVERVIEW

In this chapter tert-butyal nitrite (TBN) on two different transition metals, Cu—a moderately active coinage metal and Rh—a very active group VIII metal, was studied. When TBN adsorbs on metal surfaces, it normally breaks its internal $(CH_3)_3CO$-NO bond to generate surface tert-butoxy and nitric oxide, making these systems closely related to two major industrial applications: hydrocarbon partial oxidation and NO reduction. As a common intermediate in partial oxidation reactions, by which alcohols, ketones and acids etc. are transformed from hydrocarbons in the chemical refining process, tert-butoxy was synthesized by dissociation of TBN on clean Rh and Cu(111) and tert-butyl alcohol (TBA) on oxygen-covered Rh, and its thermal decomposition mechanism with and without co-adsorbed NO was studied using time-of-flight mass spectrometry and Auger electron spectroscopy. The first part of this chapter describes TBN on Cu(111), and the second part describes TBN on clean Rh and TBA on oxygen-covered Rh.

For TBN on clean Cu(111), adsorbed TBO and NO form as the dissociation product of TBN. N_2O and N_2 desorb at 194 K and leave adsorbed N and O on the surface. Some tert-butoxy reacts at relatively low temperature (<240 K) to form water, carbon monoxide, carbon dioxide, acetylene, proposed imide and acetate, and the remaining tert-butoxy disproportionates to tert-butyl alcohol, isobutene and adsorbed oxygen at 610 K. The low temperature reaction paths is proposed to be initialized by the C-H cleavage followed by C-C bond breaking to form adsorbed methylene. The methylene couples to di-σ-bonded ethylene, which can either dehydrogenate to acetylene desorbing at 335 K via a vinyl intermediate or be partially oxidized to acetate that dissociates at 580 K. There is also evidence of NH bond formation during this process. The high temperature tert-butoxy decomposition is a bimolecular reaction involving hydrogen transfer between two tert-butoxy groups.

While *t*-butoxy groups are formed when TBN and TBA dissociate on clean Rh and when TBA dissociates on O-covered Rh, there are significant differences in the thermal behavior of these systems. For TBN on clean Rh, there is evidence that a monolayer decomposes to form NO and two oxygen-containing fragments, *t*-butoxy and a stabilized oxametallacycle. The proposed oxametallacycle decomposes at 350 K to acetone, while *t*-butoxy, relatively stable in the presence of N and NO, decomposes to isobutene at 500 K. For TBA dosed onto an O-covered surface, the O—H bond breaks between 200 and 300 K to form *t*-butoxy. This occurs in competition with TBA desorption. The *t*-butoxy is stable only up to 380 K where, assisted by O, it decomposes to acetone and butene via a transient form of the oxametallacycle involved in TBN. Combustion reactions to form water, carbon monoxide and carbon dioxide compete. For monolayer TBA dosed on a clean Rh surface, H_2, H_2O and CO, but no acetone or butene, appear in TPD and carbon remains after TPD.

3.2 INTRODUCTION

Surface alkoxy species ($RO_{(a)}$) are common intermediates in heterogeneously catalyzed partial oxidation reactions, and are involved in several petrochemical processes [3.1] One example is methanol catalytic oxidation to formaldehyde on Ag [3.2]. The thermal dissociation of surface alkoxy species is mainly via β-hydrogen elimination [3.3] since β C-H bonds are 4-7 kcal/mol weaker than other C-H bonds. Generally, primary alkoxies are oxidized to aldehydes, and secondary alkoxies to ketones on oxygen covered metal surfaces [3.4-3.7]. tert-Butoxy (TBO) has no β-hydrogen, and is more stable thermally, e.g., on Cu(100), tert-butoxy is stable up to 500 K, but methoxy starts to dehydrogenate at 350 K [3.8]. tert-Butoxy decomposes thermally on relatively active transition metal surfaces, e.g. Rh [3.9-3.11] and Pt [3.12]. It undergoes dehydrogenation to form water, dihydrogen, carbon monoxide and surface carbon without co-adsorbed oxygen. With oxygen on Rh(111), it decomposes to isobutene and tert-butyl alcohol (TBA) but not acetone. On less active metal surfaces such as Ag and Cu, its chemistry is more complicated. On oxygen covered Ag(110) [3.13], tert-butyl alcohol, isobutene oxide, isobutene, acetone, water and carbon dioxide form via a proposed unstable oxametallacycle intermediate. On oxygen covered Cu(110) [3.14], no carbon-carbon bond cleavage occurs, and tert-butyl alcohol, isobutene and water form. When coadsorbed with NO on Cu(100) [3.8], C-C bonds break and the products include dihydrogen, acetone and tert-butyl alcohol.

With two functional groups bound by a weak chemical bond (~171 kJ/mol), tertiary butyl nitrite (TBN), $(CH_3)_3CO\text{-}NO$, is an excellent precursor to yield high concentration surface alkoxy species and NO. It makes TBN-on-metal a good model system for not only hydrocarbon partial oxidation but also nitrogen oxides (NOx) reduction by hydrocarbons and alcohols. Due to environmental urgency, NOx reduction by hydrocarbons has been intensively studied over the past two decades [3.15-3.17] on metal additive oxides. Coinage metals—Cu, Ag and Au, have been studied [3.18-3.20]. During the course of hydrocarbon oxidation by NOx, alkoxy species are likely one of the intermediates since the final products contain alcohols, ketones and aldehydes. Beyond this, C1-C3 alcohols were also studied to reduce NOx directly [3.21-3.23]. Although thought to be important in NOx reduction reactions, the role of alkoxy species has not been explored extensively.

Single crystalline copper is an interesting model substrate, which has much stronger oxygen affinity than the second and third row transition metals, and typically has greater catalytic oxidation activity than Ag and Au but less than Pt and Rh. Since alcohols do not readily thermally dissociate on Cu, tert-butoxy was prepared by dosing tert-butyl acohol on an oxygen-covered surface [3.8, 3.14, 3.24, 3.25]. As an alternative route to generate tert-butoxy on a clean Cu surface, TBN has been dosed directly on Cu(100) in our group. Whereas TBA produces one tert-butoxy and one surface hydroxyl for each coadsorbed O, TBN dissociates to one ter-butoxy and one adsorbed NO, the latter can be dissociated to form atomic N and O, $(NO)_2$ and N_2O [3.26].

Polycrystalline surfaces mimic the real catalysts better than single crystal surfaces. On a clean Rh surface, bond cleavage of TBA is not selective for O-H. Predosing oxygen attenuates surface dehydrogenation and facilitates the selective formation of tert-butoxy by promoting hydrogen transfer from hydroxyl in TBA to surface oxygen. An alternative *t*-butoxy source, TBN, has a weak internal $(CH_3)_3CO$—NO that readily cleaves. Whereas TBA dissociation on O-covered metals leads to OH, TBN dissociation leads to NO that on Rh surfaces is relatively strongly bound and upon thermal activation can be dissociated to form adsorbed atomic O and N that recombines to N_2 above 650 K [3.26]. The mechanism and kinetics describing decomposition of TBO coadsorbed with atomic oxygen on O-covered Rh(111) have been reported [3.9]. Isobutene forms indicating C—O bond cleavage. Contrasting with tertiary forms, primary alkoxy species dehydrogenate and decarbonylate (except methoxy) via either aldehyde or oxametallacycle intermediates [3.27-3.30]. Secondary alkoxy species form ketones [3.27, 3.31].

3.3 PART I: TBN ON Cu(111)

3.3.1 Experimental

A detailed description of the overall apparatus and of the novel analytical instrument used here can be found in another paper [3.32]. In summary, work was done in an ultrahigh vacuum chamber, base pressure of 3×10^{-10} Torr, equipped for time-of-flight mass spectrometry (TOFMS) and Auger electron spectroscopy (AES). A Cu(111) crystal (12 mm in diameter and 2.5 mm thick) was mounted on a tungsten wire loop that, in turn, was connected to electrically isolated copper rods in the UHV system. The substrate was cooled to 85 K and resistively heated to 850 K. Higher temperatures were avoided to preclude only copper evaporation. The crystal was routinely cleaned by repeated cycles of 1.6 keV argon ion sputtering at 500K and annealing to 850K for 10 minutes. Surface cleanliness was verified by AES. Carbon was the primary contaminant.

TBN (Aldrich, 90%) was used after several freeze-pump-thaw purification cycles. Based on residual gas analysis (RGA), the TBN source contained less than 2% TBA. TBN was dosed through a toggle-controlled, calibrated leak valve connected to a 3mm stainless steel tube that is terminated 2-3 cm from the copper surface. The pressure behind the toggle valve was standardized before each dose to 0.400 Torr as measured by a Baratron gauge. During dosing the chamber pressure was not recorded because the ion gauge was turned off to avoid electron-induced decomposition of the sample. However, in test exposures the leak valve was calibrated to produce an initial pressure 1 x 10^{-8} Torr. Exposures are calculated assuming a constant dosing pressure equal to this initial pressure. Low vapor pressures of TBN behind the leak valve were maintained by cooling the source in a bath of dry ice and acetone, further improving the purity of the reagent reaching the copper surface. The TBN exposure is present in Langmuire (L), 1 L=1.0 x 10^{-6} Torr·sec.

Oxygen (Spectra, research grade) was dosed by backfilling through a separate leak valve to a chamber pressure of 1 x 10^{-6} Torr with the crystal held at 400K. Oxygen coverages were evaluated by comparing the measured atomic ratio of oxygen to copper with the saturation value as determined by AES. This number was then normalized to literature value of 0.45 ML for the oxygen saturation coverage of copper [3.33].

TPD was performed over the temperature range of 100-800 K with a ramp rate of 3.0 K s^{-1}. The temperature was measured with a type-K thermocouple inserted into a hole drilled into the top of the sample. Desorbing species were monitored repeatedly by TOFMS, acquiring a full mass spectrum from 1 to 150 amu every 0.3 sec. This upper limit exceeds the parent masses of TBA (74 amu) and TBN (103 amu), allowing a searchable reference for desorption products containing up to eight carbons. Since every mass over the range is recorded in every scan, this method records in one experiment all the species that do and do not desorb, and makes possible retrospective analysis for any positive ion within the mass range recorded.

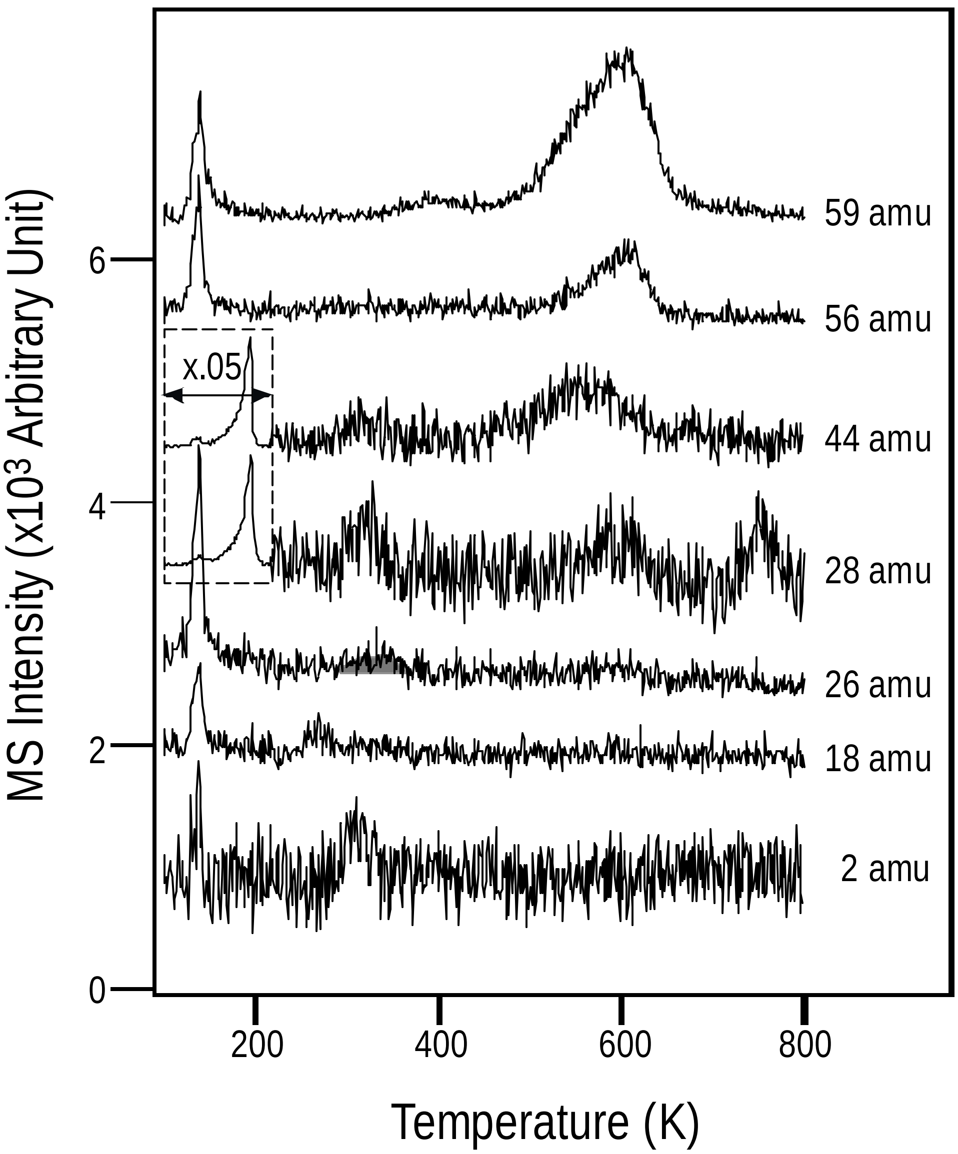

Figure 3.1: TOFMS-TPD (3.0 K/s) of 0.50 L (~ 4 monolayer) of tert-butyl nitrite (TBN) dosed onto clean Cu(111) at 100 K. The traces of 28 amu and 44 amu between 100 K and 220 K (dashed rectangle) are scaled by 0.05, and all others are on the same scale.

3.3.2 Results and Analysis

3.3.2.1 Overall Picture.

TPDs of seven chosen masses of 0.5 L TBN on Cu(111) (Figure 3.1) and AES of 0.5 L TBN on Cu(111) at different annealing temperatures (Figure 3.2) are presented to overview TBN desorption and thermal decomposition on Cu(111) before moving to detailed discussion. The TPD results are summarized using seven masses selected from the full TOFMS data set. From bottom to top, these traces are assigned, on the basis of fragmentation pattern analysis, as follows: 2 amu—dihydrogen, 18 amu—water, 26 amu—acetylene, 28 amu—carbon monoxide and dinitrogen, 44 amu—carbon dioxide and nitrous oxide, 56—amu isobutene, and 59 amu—TBA. Clearly, TBN dissociates on clean Cu(111) to yield an array of products. The characteristic TBN molecular desorption peaks at 30 and 88 amu are not plotted but TBN desorption accounts (cracking pattern) for all the peaks at 143 K in Figure 3.1. The 143 K peak is attributed to TBN multilayer desorption; its intensity does not saturate (not shown), and the peak temperature is consistent with multilayer desorption on Rh (145 K) (next section 3.4) and Pt (150 K) [3.12]. The absence of a distinct monolayer desorption features indicates that none of the TBN in contact with copper desorbs intact. Defining the appearance of TBN multilayer as a 1 ML, somewhat arbitrarily, 0.5 L exposure corresponds to ~ 4 ML.

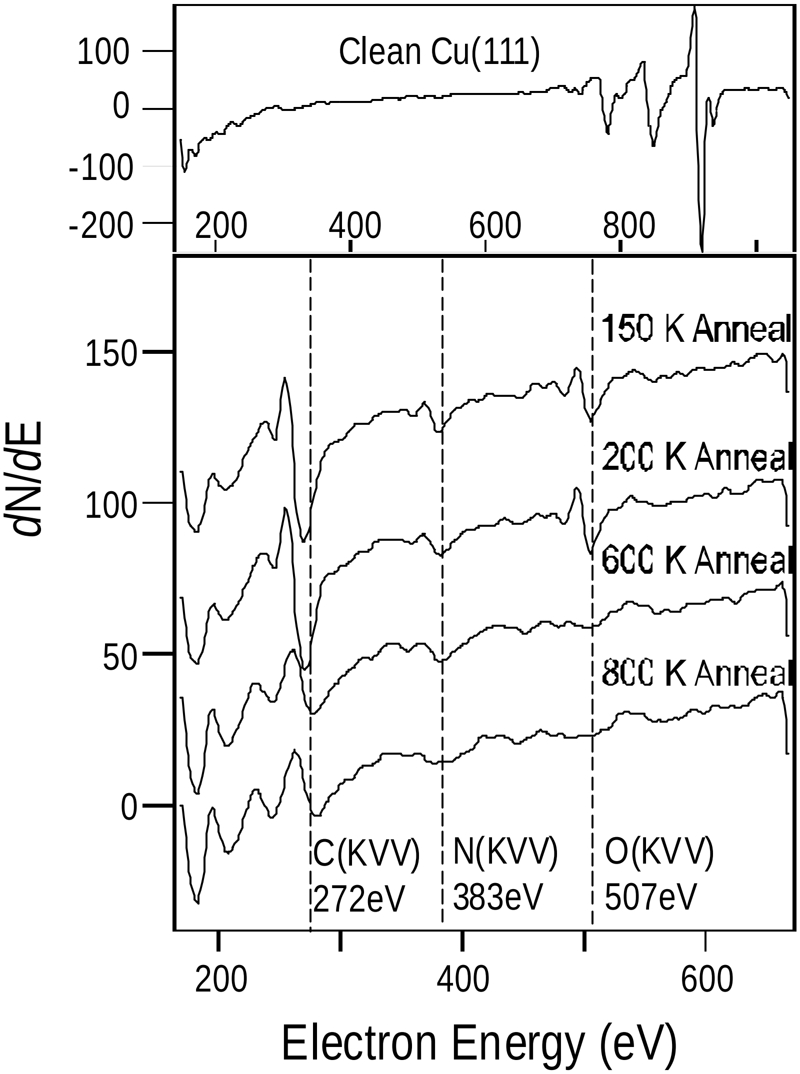

Figure 3.2. Upper panel: AES of a clean Cu(111) surface. Bottom panel: a set of AES of 0.5 L TBN on Cu(111) annealed to different temperatures. All spectra are taken at 150 K, and annealing dwell time is 60 s. Each spectrum is taken at different physical location on an identical sample to avoid the electron-induced effects [3.34].

To help identify the evolved and surface residual species, a set of AES was taken at different annealing temperatures (Figure 3.2). 150 K annealing desorbs multilayer TBN and generates a surface covered by TBN decomposition products, made up of carbon, nitrogen and oxygen. The carbon peak has 14 eV broadening, i.e. the energy difference between the maximum of the positive-going excursion and the minimum of the negative-going excursion in the derivative AES spectra, and the minimum is located at 268 eV, showing that the carbon is sp^3 hybridized [3.35, 3.36]. Likely, $(CH_3)_3O$-NO breaks its internal N-O bond to form adsorbed TBO and NO. The latter may dissociate or dimerize to $N_{(a)}$, $O_{(a)}$ and $(NO)_2$ [3.26]. Annealed to 200 K, the nitrogen and oxygen signals decrease but not carbon, reflecting desorption of nitrogen oxides, or N_2 and O_2. The latter is excluded because the temperature is too low for either oxygen [3.37] or nitrogen [3.38]. Annealing to 600 K desorbs all oxygen but there are still nitrogen- and carbon- containing species. The carbon peak is broadened to 16 eV, and its peak position moves to higher kinetic energy, 272 eV, indicating the carbon distribution contains both sp^3 and sp^2 hybridizations. The transformation of carbon hybridization from sp^3 to sp^2 implies that dehydrogenation occurs between 200 K and 600 K. Since no hydrogen containing species desorbs above this temperature, this carbon is likely amorphous. Annealing at 800 K removes nitrogen but not carbon, so the nitrogen must leave as N_2. The carbon becomes mostly, if not all, sp^2 hybridized.

Returning to TPD results (Figure 3.1), there are sharp peaks of mass 44 amu and 28 amu at 194 K. The 194 K peak is assigned to N_2O (44 amu) and N_2 (28 amu) desorption since the 28 amu to 44 amu ratio is very close to 1:1, distinctly different from the ratio (0.11) in the N_2O standard mass spectrum. Assuming N_2 and N_2O have the same sensitivity factor in the TOFMS, the N_2O to N_2 ratio is about 0.89:1. Since NO is the primary N-containing product of TBN dissociation, removing nitrogen as N_2O and N_2 will leave some oxygen on the surface. Because there is no further N_2 desorption for low TBN exposures, the estimated TBO to $O_{(a)}$ ratio is 1:0.76. At high exposures, the ratio depends on the higher temperature N_2 desorption as well. For a 0.5 L dose of TBN onto Cu(111) (Figure 3.1), the TBO to $O_{(a)}$ ratio is 1:0.88. This oxygen is used to generate H_2O when the first dehydrogenation commences at 240 K. The water desorption rate maximizes at 265 K and ends at 300 K. As the H_2O desorption rate drops, H_2 evolution begins, indicating that dehydrogenation occurs and $O—H_{(a)}$, the proposed surface precursor leading to H_2O (see next section), is consumed. The H_2 desorption, starting at 265 K and peaking at 310 K [3.39, 3.40], is considered as reaction-limited because the peak is symmetric and the coverage of dehydrogenation-generated $H_{(a)}$ is much less than the saturation coverage ($\theta \sim 0.5$ ML). How the other co-adsorbed species affect the $H_{(a)}$ recombination was not considered because there are too many species on the surface. It is noteworthy that the $H_{(a)}$ recombination of TBA on O-covered Cu(110) follows the same reaction kinetics as $H_{(a)}$ on clean Cu(110).

As the TPD temperature increases above 290 K, the CO and CO_2 signals both rise and peak at 320 K. Their peak temperatures are well above the temperatures of molecular CO (170 K) [3.41] and CO_2 desorption (200 K) [3.42] on Cu(111). Thus, the desorption is reaction-limited. These two peaks track each other very well from 290 K to 350 K, suggesting strongly they are from the same surface intermediate. C-C bond breaking is involved during this process since there is no C1 species on the starting surface. The formation of C_2H_2 peaking at 335 K also requires C-C bond breaking. Although acetylene is a barely discernable for 0.5 L TBN dose, it is obvious under other conditions (see next section). The process—starting at 240 with water desorption and ending at 360 K with ethylene formation—is denoted TBO decomposition (TBO(I)), and will be discussed more detailed in next section.

For temperature just above TBO(I), a weak and broad TBA (59 amu) peak appears at 390 K and extends to 440 K. There is some evidence that this TBA evolution is associated to N_2O and N_2 desorption at 194 K and N_2 desorption at 760 K. In other words, it may involve proton transfer between carbon and nitrogen.

Moving to higher temperature (490 K), from the coincident onsets of CO_2 and TBA desorption we infer that hydrogen transfers from a surface intermediate to

TBO and the transfer leads dehydrogenation of the intermediate to yield CO_2 and hydrogenation of TBO to form TBA. This process extends over a broad temperature range so it overlaps with TBO disproportionation, the latter yielding TBA, isobutene, and CO. If the higher temperature TBA peak is deconvoluted, its leading edge overlaps closely the 580 K CO_2 peak and its falling edge overlaps with the isobutene peak except the tail. The kinetics of the thermal decomposition of TBO, generated by t-BuO-H dissociation on an oxygen predosed surface at 120 K, has been studied by TPD of isotopically labeled TBA on Cu(110) [3.14]. TBO decomposes to isobutene, TBA and water via a proposed metallacycle intermediate (**1**) at 600 K. Unlike the Cu(110) case, we find no water desorption accompanying the decomposition of TBO (Figure 3.1) in the region between 450 and 650 K. Thus, a somewhat different mechanistic pathway must be followed. We propose that TBO generated by TBN on Cu(111) disproportionates in a concerted bimolecular reaction. The argument of bimolecular reaction is also supported by the desorption peak characteristics of TBA (right panel in figure 3.4) and isobutene (not shown). The falling edges of the TBA and isobutene peaks overlap very well and the TBA peak moves to lower temperatures with increasing coverage, consistent with a second-order reaction. The mechanisms are compared in Scheme 3.1, and the overall reaction can be writen as: $2C_4H_9O_{(ad)} \rightarrow C_4H_{10}O_{(g)} + C_4H_{8(g)} + O_{(ad)}$. The adsorbed O reacts with residual carbon to form CO leaving the surface.

Scheme 3.1. The possible reaction mechanisms of TBO disproportionation

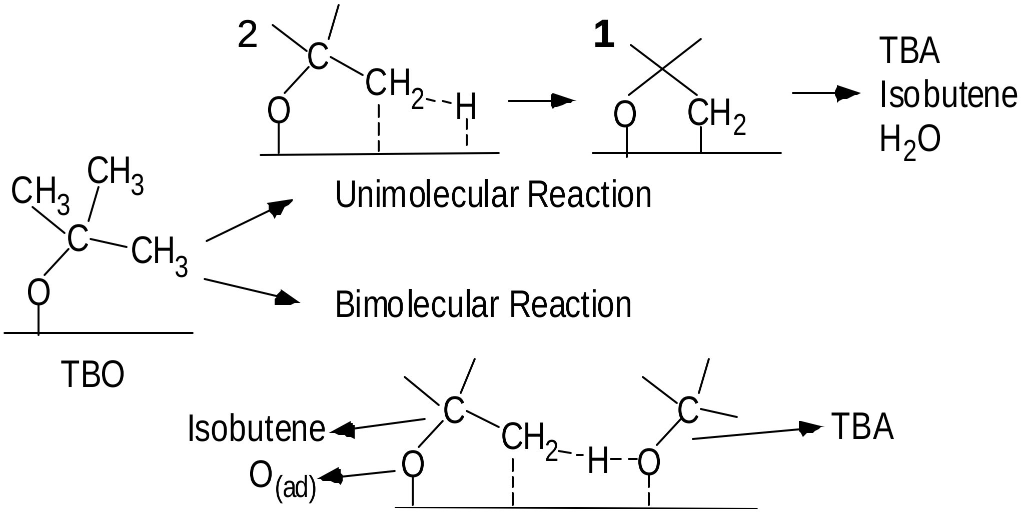

By 680 K, all the signals, except for 28 amu, have returned to background levels, i.e., there are no more C-H bonds to be broken. The highest temperature 28 amu peak is attributed to the $N_{(a)}$ recombination (760 K) [3.38], consistent with the AES annealing results (Figure 3.2). As noted above, AES after the sample was heated to 800 K indicates a small amount of C as the only contribution other than Cu itself.

As described above, after multilayer TBN desorbs from the surface at 143 K, surface reactions occur throughout the temperature region to 800 K. N_2O forms and desorbs with N_2 at 194 K, and adsorbed O and N are left on the surface. Via TBO decomposition (<350 K), the $O_{(a)}$ forms surface hydroxyl, which leads to water. The other products include dihydrogen, carbon dioxide, carbon monoxide and acetylene.

At slightly higher temperature (390 K), the first TBA desorption peak appears. We propose this involves bond breaking and formation of C-H and N-H (see below). At 580 K, a surface intermediate dissociates to form CO_2 and an H atom transfers to TBO to form TBA. Finally, TBO disproportionation happens at 610 K to yield TBA, isobutene and O, the latter reacting with surface residual C to form CO. The following sections will focus on (1) the possible reaction pathways TBO(I) and the possible intermediate(s) decomposing at 580 K, as well as its relation with TBO(I), and (2) the evidence of hydrogen transferring between carbon and nitrogen.

3.3.2.2 *TBO(I)*

The unique chemistry between 240 K and 360 K in the thermal desorption spectra deserves more careful study. A brief summary is given first before moving to a detailed analysis of our data and the literature. TBO(I) commences with oxydehrogenation and/or dehydrogenation of its methyl groups, leading to di-σ-bonded oxymetallacycle intermediate (**1**), which undergoes α-methyl elimination to form $CO_{(a)}$, $OH_{(a)}$ and, most importantly, methylene. After methylene couples to ethylene and oxydehdrogenates, two major competing intermediates exist: one is vinyl, $-CH=CH_2$, which oxydehydrogenatates further to acetylene that desorbs at 335 K, the other is ethylidyne, $=CCH_3$, which is either oxidized to acetate that decomposes further to CO_2 and H at 590 K, or is the source of the carbon retained at 800 K.

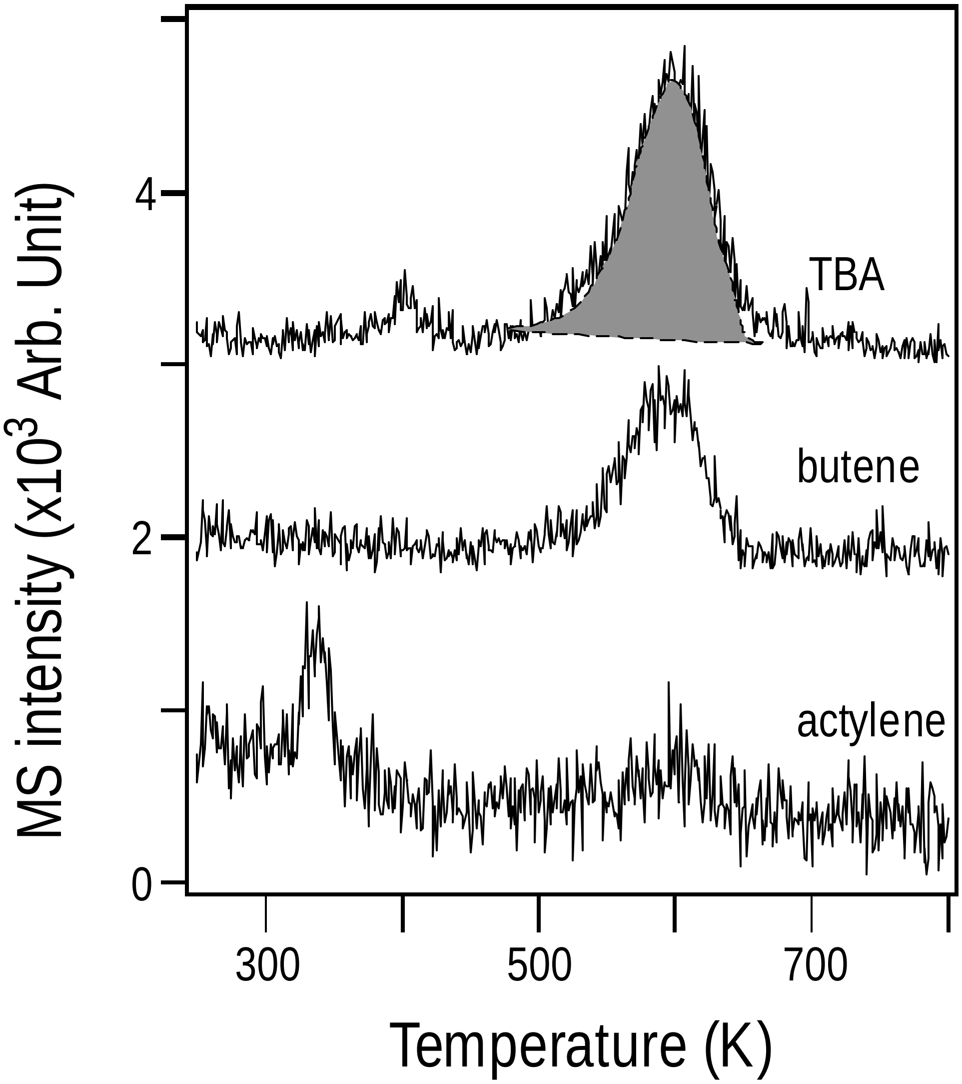

Figure 3.3. TOFMS-TPD of 0.5 L TBN dosed onto oxygen covered (θ=0.1ML) Cu(111) at 100 K. Compared to TBN on clean Cu(111) (Figure 3.1), more acetylene forms and TBA and isobutene signals track each other very well. A scaled isobutene signal (x 1.7) is outlined as a shadow under 600 K TBA desorption peak to emphasize the consistence of this two species.

After N_2O desorption, there should be $O_{(a)}$, $N_{(a)}$ and TBO on the surface. The formation of water indicates the C-H cleavage. Since there is not a distinguishable water monolayer desorption in water TPD on Cu(111) [3.43], this water desorption must come from either $H_{(a)}$—$OH_{(a)}$ recombination or $OH_{(a)}$—$OH_{(a)}$ disproportionation. Due to the fact that the Langmuir—Hinshelwood reaction between $O_{(a)}$ and $H_{(a)}$ to form $OH_{(a)}$ does not occur on Cu(111) [3.44], the origin of $OH_{(a)}$ must come from tert-butyl group oxydehydrogenation, i.e., the C-H bond cleavage is faciliated by co-adsorbed atomic O, rather than normal dehydrogenation on copper. Normal dehydrogenation also occurs to place $H_{(a)}$ transiently on Cu as evidenced by the evolution of H_2, but the dehydrogenation group may not be the methyl in TBO. The H_2 desorption onsets as the H_2O desorption starts to decrease, suggesting the H_2O is formed by $H_{(a)}$—$OH_{(a)}$ recombination. The temperature of the occurrence of TBN oxydehydrogenation cannot be determined precisely since its product(s), e.g., -$OH_{(a)}$, is not volatile, but it should be below 240 K. The complete oxidation products—CO and CO_2, onset and peak slightly later than H_2 but end at the same temperature as H_2, indicating that the dehydrogenation involves multiple steps. The formation of CO and CO_2 requires the C-C bond cleavage. Since acetylene froms, some C-C cleavage occurs before all C-H bonds break. Likely, the CO and CO_2 come from the $CH_xCO_{(a)}$ dehydrogenation.

The formation of acetylene is very interesting. The desorption-limited acetylene [3.45, 3.46] comes from either the coupling between adsorbed CH_x or methyl migration from the central carbon to a branch carbon followed by C-C cleavage. The latter is unlikely because (1) methyl migration normally involves radical, cation or anion; (2) even if methyl migration happens, tert-butyl group is more stable than other C4 alkyls and should be the product not the reactant; and (3) this reaction path is too complicated to lead to highly selective products. Alkyl C-C cleavage without oxidation on metal surfaces has been seldom documented. One example is that neopentyl ($(CH_3)_3CCH_{2(a)}$-) undergoes α-methyl elimination to form isobutene and methane on Ni(100) at 200 K or lower [3.47, 3.48]. At first glance, the lack of α-methyl in TBO (α to the surface) may be replaced by γ-methyl elimination. Indeed, these two species are very similar if the oxydehydrogenation occurs prior to the methyl elimination. As a result of C-H bond cleavage, a surface intermediate (**1**), $-_{(a)}OC(CH_3)_2CH_{2(a)}-$, is generated. Counting from the $C_{(a)}$ end (right side) but not the O end (left side) (Scheme 3.1), there is an α-methyl group. Comparing this surface intermediate with adsorbed neopentyl group, the similarity is very clear. Upon α-methyl elimination, adsorbed neopentyl fomrs surface methylene and volatile isobutene. α-Methyl elimination of the surface intermediate (**1**) would yield surface methylene and a surface intermediate, either be η^2–dimethyl methyleneoxy (**3**) or di-σ-dimethyl methoxy (**4**). The latter is favored since intermediate (**3**) will lead to acetone evolution contrary to our observations. Intermediate (**4**) can oxydehydrogenate and eliminate the rest methyl groups via the similar path and generate $CO_{(a)}$, $OH_{(a)}$ and $CH_{2(a)}$ on the surface.

Scheme 3.2 Possible surface intermediates formed during TBO degeneration below 300 K

The surface chemistry of methylene on metal surfaces has been studied extensively [3.48, 3.49]. Unlike on active transition metal surfaces, such as Rh, Pd, Pt, methylene is coupled readily into ethylene instead of oxidation and self-hydrogenation on copper. From methylene to acetylene, there are two reaction pathways at least. One is methylene coupling to di-σ bonded ethylene followed by ethylene dehydrogenation. The other is methylene dehydrogenation to methylidyne ($CH_{(a)}$) and then methylidyne is coupled to acetylene. The pathway of methylene dehydrogenation followed by coupling to acetylene is discussed first. Methylene has been studied on many surfaces, including copper [3.50-3.52] but its oxidation or dehydrogenation details on copper surfaces remains unclear. Generally, methylene coupling and oxidation (including oxydehyrogenation and dehydrogenation) compete. Methylene decomposition to methylidyne, $CH_{(a)}$ and $H_{(a)}$ is a dominant reaction path on most transition metal surfaces, but not coinage metals [3.48]. Furthermore, methylidyne coupling to acetylene has not been reported on Cu but only on Ni(111) under certain conditions [3.53]. So, dehydrogenation followed by coupling is not likely. The second path, methylene coupling to ehtylene, is a primary reaction channel on copper surfaces [3.48]. Besides molecular adsorbed ethylene desorbing at 240 K, ethylene can adsorb on copper strongly via a di-σ-bonded form that can transform into ethylidyne ($CH_3C_{(a)}$) at 371 K [3.49]. Ethylene can also react with surface oxygen on Cu(111) to form acetylene as described below [3.54, 3.55]:

$C_2H_{4(ad)} + O_{(ad)} \rightarrow C_2H_{3(ad)} + OH_{(ad)}$; $C_2H_{3(ad)} + O_{(ad)} \rightarrow C_2H_{2(ad)} + OH_{(ad)}$. The details of acetylene formation reaction will be discussed later in this section.

However, methylene to acetylene by this path is not the only reaction path. The TBA desorption peak has a strong shoulder at 580 K (Figure 3.1) coincident with the CO_2 peak, suggesting a surface intermediate dissociates. The TBA shoulder becomes a separate peak and is a clearly resolved peak at lower TBN exposure (not shown). Figure 3.3 shows how the 580 K TBA peak/shoulder associates with acetylene desorption around 335 K. Comparing 0.5 L TBN dosed onto oxygen-covered (?=0.1) Cu(111) (Figure 3.3) to the same amount of TBN dosed onto clean Cu(111) (Figure 3.1), the TBA and isobutene desorption peaks overlap quite well, showing they are from a single intermediate. The slight mismatch at their leading edges indicates there is still a minor reaction transferring hydrogen to TBO. Meanwhile, the acetylene intensity increases significantly with the decreasing of the 580 K TBA shoulder, indicating the reaction pathway leading to the acetylene competes with the pathway leading to the intermediate causing the TBA 580 K shoulder.

To identify the intermediate, careful study of Figure 3.1 from 520 K to 560 K is necessary. Between the onset of TBA and the onset of isobutene, the only desorbing species besides TBA is CO_2, indicating the intermediate is an O-containing species. From one TBO to one TBA, one additional hydrogen is needed. Thus, the intermediate contains H also. No CO desorbs during this process showing that the two oxygen atoms used to form CO_2 are bonded to the same carbon in the intermediate, i.e., the intermediate is in either an acid ($RCO_{(a)}O_{(a)}^-$) or dioxy ($R_1R_2CO_{(a)}O_{(a)}$) form. Acid is favored since dioxy is unstable and decomposes at very low temperature, e.g., η^2-methylenedioxy decomposes at 225 K on Ag(110) [3.56]. The simplest acid, formic acid, is excluded since surface formate ($HCOO^-$) decomposes at much lower temperature—480 K on Cu(111) [3.57] and 460 K on Cu(110) [3.58] and its small H-to-O ratio cannot provide enough hydrogen to form the amount of TBA observed. The decomposition temperature of the intermediate is consistent with acetate dissociate temperature on Cu(110)— ~590 K [3.59, 3.60]. So, we speculate that the intermediate is acetate, at least acetate-like. Acetate decomposition on Cu(110) has been proposed to occur via acetic anhydride intermediate to form CH_4, CH_3COOH, CO_2, H_2C_2O and residual carbon, but there is no direct evidence to support the anhydride intermediate. The inconsistency in decomposition products may result from the different reaction paths caused by different surface conditions.

Assuming formation of acetate, we expected it to be strongly affected by local chemical surroundings, and to alter the competition between ethylene oxydehydrogenation and oxidation. Ethylene adsorbs on metal surfaces in either strongly di-s-bonded form ($-_{(a)}CH_2\text{-}CH_{2(a)}-$) or weakly p-bonded form. The di-s-bonded form normally occurs on active transition metal surface, such as Ni [3.61], Pd [3.62], Pt [3.63], Ru [3.64] and Rh [3.30], and leads to surface ethylidyne by dehydrogenation, which has been verified by the absence of 1500 cm^{-1} C=C vibration. On coinage metal surfaces, such as Cu(111) [3.65], Cu(100) [3.66, 3.67], Cu(110) [3.68] , Ag(110) [3.69] and Au(110) [3.70], p-bonded ethylene overwhelms di-s-bonded ethylene. Co-adsorbed oxygen favors the p-bonded form. The reason is that the co-adsorbed oxygen withdraws electron density and inhibits the formation of di-s-bonds. Oxydehydrogenation of this di-s-bonded ethylene will yield surface ethylidyne. $O_{(ad)}$ insertion into a C-Cu bond leads to acetate formation. Although most ethylene adsorbs on copper by weak p-bond and strong di-s-bond only forms at 371 K [3.49], the origin of ethylene—methylene couples to ethylene—in our case makes the s-bond exist even before ethylene fully formed. As mentioned before, at least two possible pathways exist for the proposed di-s-bonded ethylene. One is partial oxidation and yields acetate, which decomposes at 590 K. The other, as envisioned in Scheme 3.3, involves a vinyl intermediate [3.71] and forms acetylene that desorbs at 335 K (Figure 3.1). On an oxygen-covered surface, vinyl pathway is favored, probably due to the electron withdrawing effect induced by co-adsorbed oxygen. Thus, a large amount of acetylene but little acetate is generated (Figure 3.3). On a clean surface, the ethylidyne pathway is favored, and less acetylene and more acetate form.

Scheme 3.3. The possible reaction mechanism of acetylene formation form methylene via a vinyl intermediate

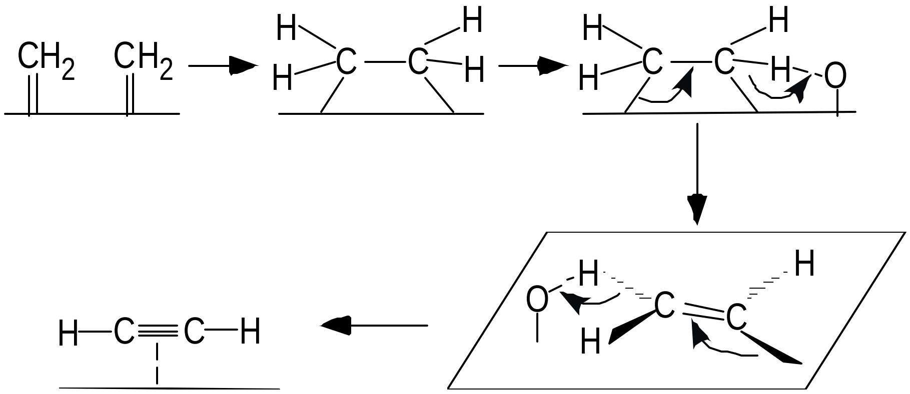

3.3.2.3 Possible NH$_y$ intermediate.

The relation between N_2 desorption and the weak 410 K TBA desorption is demonstrated by their variation with TBN dose (Figure 3.4). The desorption of both

N_2 and TBA appears at the same TBN exposure and even the variation trends follow each other. At a low exposure (= 0.1 L), there is neither N_2 nor 410 K TBA. When the exposure increases to 0.25 L, a little N_2 shows up, as well as a marginal TBA peak appears at 410 K. The TBA peak increases monotonically with increasing of N_2, showing that these two peaks are closely related. As mentioned before, TBO is the primary adsorbate on the surface, and it requires one hydrogen to become TBA. Lack of desorption species except TBA makes it difficult to determine the origin of the hydrogen, but other volatile products are excluded (such as CO and CO_2), i.e., the decomposition products stay on the surface. Above this temperature, the residual surface species are: acetate–decomposes at 580 K, TBO—decomposes at 610 K, surface C—some reacts with oxygen to CO at 610 K and some stays on the surface up to 800 K, surface N—recombines at 760 K. So, the most likely species are C_nH_m and N_xH_y. The close relation between the amount of $N_{(a)}$ and the amount of hydrogen makes N_xH_y preferred. $NH_{x(a)}$ (x=1, 2) has been synthesized from ammonia by oxidation with O_2 or NO_X and identified spectroscopically on many metal surfaces, including copper [3.54, 3.72, 3.73]. A study of hydrazine on copper [3.72] suggests there is dissociation, $N_2H_{x(ad)} \rightarrow NH_{y(ad)}$ but not coupling reaction. So, NH_x is proposed in our case. The difference between $N_{(ad)} \rightarrow NH_{x(ad)}$ and $NH_{3(ad)} \rightarrow NH_{x(ad)}$ is significant. The former requires a reducing environment, while the latter requires an oxidizing environment. In our case $N_{(a)}$ coexists with many hydrocarbon groups on the surface, such as methyl, methylene, ethylidyne and acetylene. Thermal decomposition of CH_3-NCO on clean and K-covered (K is believed to help NCO dissociation to $N_{(a)}$ and $CO_{(a)}$) Cu(110) may be a suitable analog [3.74, 3.75]. Vibrational spectroscopy verifies the formation of NH_x via $N_{(a)}$ hydrogenation by $CH_{3(a)}$ at 300 K. The disappearance of the 3300 cm^{-1} N-H vibration at 425 K indicates N-H bond cleavage below this temperature.

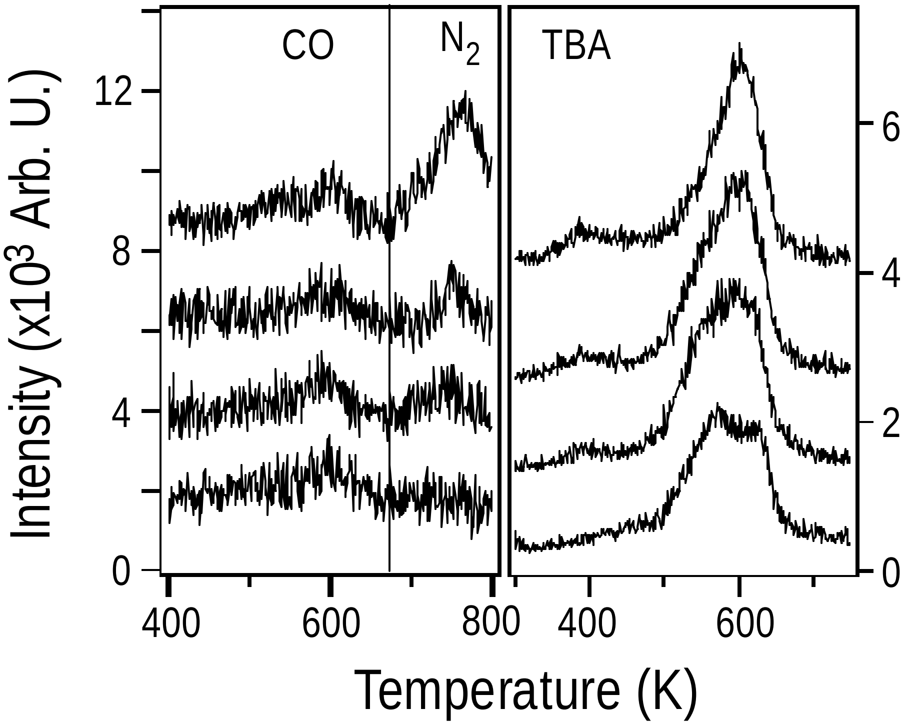

Figure 3.4: TPD of 28 amu (CO and N_2) and 59 amu (TBA) at high temperature. The TBN exposures from the bottom to the top are: 0.1 0 L, 0.25 L, 0.50 L and 1.00 L. TBN was dosed onto Cu(111) at 100 K. Other experimental conditions not specified here are the same as for Figure 3.1.

3.3.3 Reaction pathways

With the foregoing experimental results and literature review, we turn to proposed reaction pathways for TBN on Cu(111). The following steps model tert-butyl nitrite adsorption and decomposition on Cu(111):

Adsorption—desorption at 100 K

$$(CH_3)_3CONO_{(g)} \rightleftharpoons (CH_3)_3CONO_{(a)} \tag{1}$$

TBN Internal N-O bond cleavage below 140 K

$$(CH_3)_3CONO_{(a)} \rightarrow (CH_3)_3CO_{(a)} + NO_{(a)} \tag{2}$$

NO reactions on surface

$$NO_{(a)} \rightleftharpoons N_{(a)} + O_{(a)} \tag{3}$$

$$2NO_{(a)} \rightleftharpoons (NO)_{2(a)} \tag{4}$$

$$N_{(a)} + NO_{(a)} \rightleftharpoons N_2O_{(a)} \tag{5}$$

$$(NO)_{2(a)} \rightleftharpoons N_2O_{(a)} + O_{(a)} \tag{6}$$

$$N_2O_{(a)} \rightleftharpoons N_{2(a)} + O_{(a)} \tag{7}$$

N_2 and N_2O adsorption—desorption at 194 K

$$N_{2(a)} \rightleftharpoons N_{2(g)} \tag{8}$$

$$N_2O_{(a)} \rightleftharpoons N_2O_{(g)} \tag{9}$$

TBO oxydehydrogenation below 240 K

(10) $(CH_3)_3CO_{(a)} + O_{(a)} \rightarrow {}_{(a)}CCH_2C(CH_3)_2O_{(a)} + OH_{(a)}$

TBO further decomposition at 240 K to 350 K

(11) ${}_{(a)}CH_2C(CH_3)_2O_{(a)} + O_{(a)} \rightarrow CH_{2(a)} + (CH_3)_2C_{(a)}O_{(a)} + OH_{(ad)}$

(12) $(CH_3)_2C_{(a)}O_{(a)} + O_{(a)} \rightarrow\rightarrow CH_{2(a)} + CO_{(a)} + OH_{(a)}$

(13) $(CH_3)_2C_{(a)}O_{(a)} \rightarrow\rightarrow CH_{2(a)} + CO_{(a)} + H_{(a)}$

Methylene, $=CH_2$, coupling

(14) $2CH_{2(a)} \rightarrow C_2H_{4(a)}$

Ethylene, C_2H_4, oxydehydrogenation

(15) $C_2H_{4(a)} + O_{(a)} \rightarrow {}_{(a)}CCH_3 + OH_{(a)}$

(16) $C_2H_{4(a)} + O_{(a)} \rightarrow {}_{(a)}CHCH_2 + OH_{(a)}$

Vinyl, $-CH=CH_2$, oxydehydrogenation to actylene

(17) ${}_{(a)}CHCH_2 + O_{(a)} \rightarrow C_2H_{2(a)} + OH_{(a)}$

Ethylidyne, $\equiv CCH_3$, oxidation to acetate

(18) ${}_{(a)}CCH_3 + 2O_{(a)} \rightarrow {}_{(a)}OC(CH_3)O_{(a)}$

Imide, $=NH$, formation:

(19*a*) $RH_{(a)} + N_{(a)} \rightarrow R_{(a)} + NH_{(a)}$

(19*b*) $H_{(a)} + N_{(a)} \rightarrow NH_{(a)}$

Water formation and desorption at 260 K

(20) $OH_{(a)} + H_{(a)} \rightarrow H_2O_{(a)}$

(21) $H_2O_{(a)} \rightleftarrows H_2O_{(g)}$

H_2 formation and desorption at 310 K

(22) $2H_{(a)} \rightarrow H_{2(a)}$

(23) $H_{2(a)} \rightleftarrows H_{2(g)}$

CO oxidation and desorption at 325 K

(24) $CO_{(a)} + O_{(a)} \rightarrow CO_{2(a)}$

(25) $CO_{(a)} \rightarrow CO_{(g)}$

(26) $CO_{2(a)} \rightarrow CO_{2(g)}$

Acetylene, C_2H_2, desorption at 335 K

(27) $C_2H_{2(a)} \rightarrow C_2H_{2(g)}$

Hydrogen transfer between TBO and $NH_{(a)}$ leading to TBA desorption at 410 K

(28) $(CH_3)_3CO_{(a)} + NH_{(a)} \rightarrow (CH_3)_3COH_{(a)} + N_{(a)}$

(29) $(CH_3)_3COH_{(a)} \rightarrow (CH_3)_3COH_{(g)}$

Acetate, CH_3COO^-, dissociation causing CO_2 and TBA desorption at 580 K

(30) $_{(a)}OC(CH_3)O_{(a)} + (CH_3)_3CO_{(a)} \rightarrow\rightarrow CO_{2(a)} + (CH_3)_3COH_{(a)} + C_{(a)}$

(31) $CO_{2(a)} \rightarrow CO_{2(g)}$

(32) $(CH_3)_3COH_{(a)} \rightarrow (CH_3)_3COH_{(g)}$

TBO disproportionation to form TBA, isobutene and $O_{(a)}$ at 610 K

(33) $2(CH_3)_3CO_{(a)} \rightarrow (CH_3)_3COH_{(a)} + C_4H_{8(a)} + O_{(a)}$

(34) $(CH_3)_3COH(a) \rightarrow (CH_3)_3COH_{(g)}$

(35) $C_4H_{8(a)} \rightarrow C_4H_{8(g)}$

$O_{(a)}$ reacts with residual carbon to yield CO

(36) $O_{(a)} + C_{(a)} \rightarrow CO_{(a)}$

(37) $CO_{(a)} \rightarrow CO_{(g)}$

N(a) recombination at 760 K

(38) $2N_{(a)} \rightarrow N_{2(a)}$

(39) $N_{2(a)} \rightarrow N_{2(g)}$

The (a) subscripts indicate that the atoms are bound to copper, and the double single arrows (→→) indicate that the reactions involve multiple steps that cannot be subdivided into elementary steps based on our current results. The reactions of TBN on Cu(111) are very complicated, and the complexity makes it unrealistic to speculate further without vibrational spectra. For instance, the double single arrows in Equation (13) and (30) show that the reactions are definitely not elementary steps, RH in (19a) represents generally C-H bonds, and neither (19a) nor (19b) can be excluded because the precise reaction temperature is unknown. Nevertheless, the general picture of the TBN on Cu(111) is drawn and can serve as a good guide for future vibrational study.

3.4 PART II: TBN AND TBA ON CLEAN Rh AND TBA ON O-COVERED Rh

3.4.1 Experimental

The experiments were done in the same chamber as that for TBN on Cu(111). Most of experimental conditions and procedure are the same, and the differences are emphasized in the following three paragraphs.

A thin Rh foil (Alfa, 0.8 x 0.8 cm, 0.025 mm thick) was mounted on a tungsten wire loop, and cleaned initially with a few cycles of sputtering with Ar^+ at 500 K for 10 min, annealing in 2×10^{-8} torr O_2 at 800 K for 5 min, and annealing in vacuum at 1400 K for 2 min. The surface cleanliness was verified by AES.

TBA (Alfa, 99.9%) and TBN (Aldrich, 90%) were used after several freeze-pump-thaw purification cycles. Based on residual gas analysis (RGA), the TBN source contains 3% TBA. Similarly, the TBA source contains 0.4% H_2O. These were dosed via a calibrated capillary leak built into a toggle-controlled sampling valve. With a fixed pressure (y torr) behind the capillary, the dose can be stated in terms of (y x t) where t is the dose time in seconds. In these terms, 1 torr s of TBN equals 4.2 ($\pm$ 1.0) x 10^{13} molecules s^{-1} delivered to the system. During dosing, the chamber pressure was unknown since the ion gauge was turned off to avoid decomposition by electrons, especially of TBN. Oxygen (Spectra, research grade) was dosed by backfilling through a separate leak valve to a chamber pressure of 5 x 10^{-8} torr.

TPD was performed up to 950 K with a ramp rate of 4.0 K s^{-1}. The temperature was measured with a type-K thermocouple spotwelded to the back of the sample. Desorbed species were monitored repeatedly by TOFMS, acquiring a full mass spectrum from 1 to 145 amu every 0.3 sec. The upper limit exceeds the parent masses of TBA (74 amu) and TBN (103 amu), providing a search for up to C_8 products. Since every mass is recorded in every scan, this method records in one experiment all the species that do and do not desorb, and makes possible retrospective analysis for any positive ion within the mass range recorded.

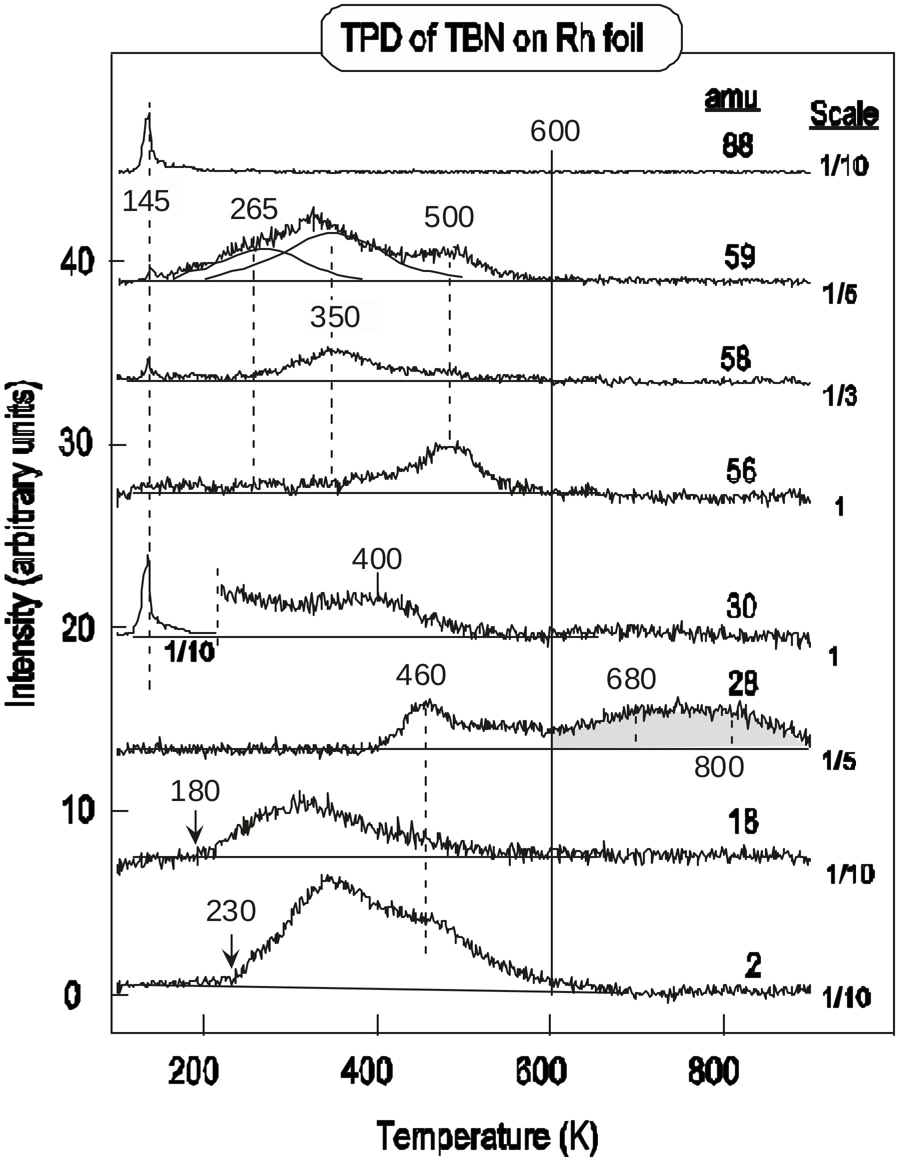

Figure 3.5: TOFMS-TPD (4.0 K s^{-1}) of 80 torr·s (3.4 x 10^{15} molecules) of t-butyl nitrite (TBN) dosed on clean Rh at 100 K. As indicated in the text and extrapolation in Figure 3.6, 1 monolayer coverage is defined as a dose of 110 torr·s. The pressure used to calculate the dose is that behind a calibrated leak, not the local pressure at the substrate.

3.4.2 Results and Analysis

3.4.2.1 TBN on Rh without $O_{(a)}$

TPD after dosing 80 torr s (3.4 x 10^{15} molecules) of TBN on clean Rh at 100 K is summarized with eight masses selected from the full TOFMS data set, Figure 3.5. From bottom to top, these traces are assigned, on the basis of fragmentation pattern analysis, as follows: 2 amu - H_2, 18 amu - H_2O, 28 amu – CO and N_2, 30 amu – TBN and NO, 56 amu – isobutene, 58 amu – TBN and acetone, 59 amu – TBN and TBA, and 88 amu – TBN. Clearly, TBN dissociates thermally on clean Rh to yield an array of products. After TPD to 900 K, the carbon level is barely detectable by AES; the C/Rh atomic ratio is < 0.05. As shown in Figure 3.6, the peak areas for TBN, two TBA peaks, acetone and isobutene are all dose-dependent.

Returning to Figure 3.5, there are sharp peaks at 145 K. The 145 K TBN peak is attributed to multilayer sublimation; its intensity does not saturate (not shown) and the peak temperature is consistent with multilayer desorption on Pt(111) [3.12] and Cu(111). The absence of a distinct monolayer desorption feature indicates that none of the TBN in contact with Rh desorbs. Based on detailed fragment analysis of all (many not shown) masses with peaks at 145 K, we conclude that small amounts of impurity TBA desorb with TBN. Since TBA dosed alone sublimes at 170 K (see Figure 3.8), apparently mixing small amounts of TBA with TBN alters the desorption properties of TBA.

When peak area is plotted as a function of dose, Figure 3.6, it is evident that TBN desorption does not occur below ~ 60 torr s (2.6×10^{15} molecules dosed), and that an extrapolation of the linearly increasing region above 150 torr s intersects the dose axis at 110 torr s. Operationally, and somewhat arbitrarily, 110 torr s (4.6×10^{15} molecules dosed) is defined as monolayer dose. Inspection of figure 2 indicates that reaction products – TBA, acetone and isobutene – are all saturated for doses exceeding 200 torr s (8.4×10^{15} molecules) and that the multilayer TBN peak makes measurable contributions below 110 torr s. Taken together, this reflects well-known tendency of TBN to form 3-dimensional islands [3.76].

As the TPD temperature increases above 145 K, the 59 and 18 amu signals (Figure 3.5) begin to rise at 180 K followed by a 2 amu onset at 230 K. This is clear evidence for surface reactions that we take as dominated by cleavage of the internal N-O bond. Although not obvious in the raw data, figure 2, there is a 59 amu peak at 265 K (sketched in) along with clearly evident peaks near 350 and at 500 K. The 265 K peak contains no evidence for TBN and is ascribed to desorption-limited TBA comprised of two parts – impurity TBA dosed with TBN and TBA formed between 100 and 265 K by hydrogenation of TBO.

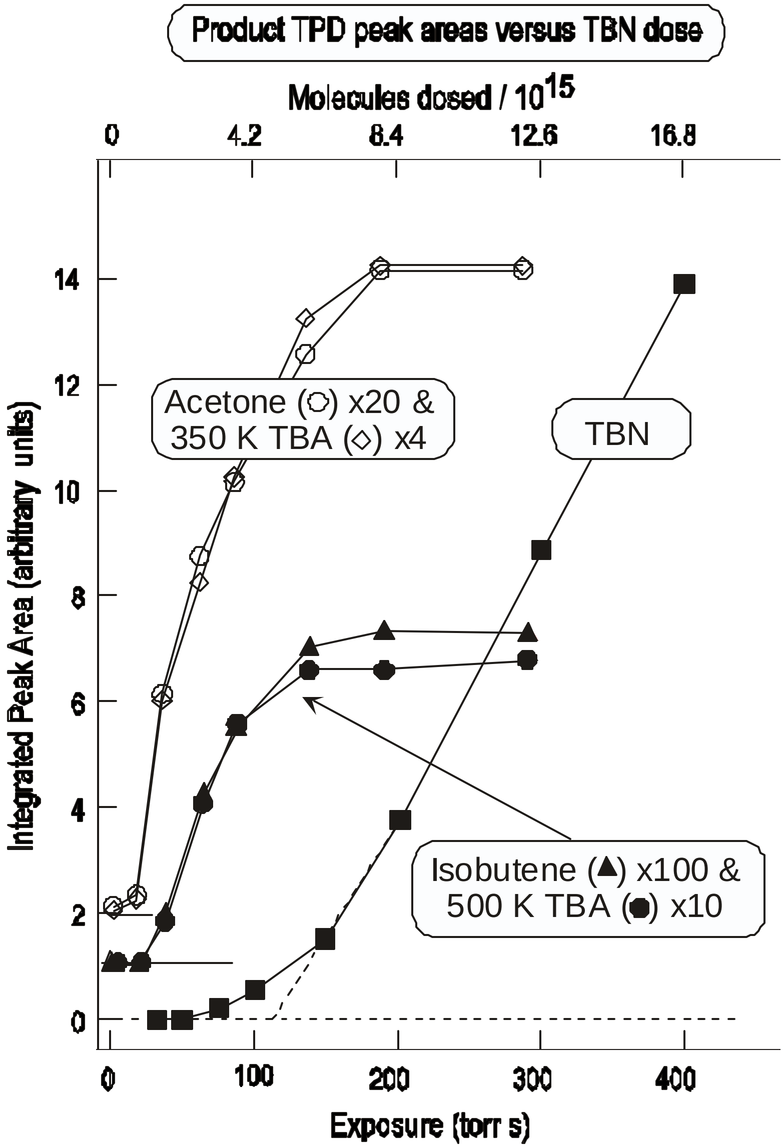

Figure 3.6: As a function of dose, integrated TPD peak areas of indicated species found in TOFMS-TPD of t-butyl nitrite (TBN) dosed on clean Rh at 100 K. The extrapolated linear region of the TBN peak area intersects the intensity axis at 110 s and is taken as an operational definition of monolayer dose (see text).

The 18 and 2 amu TPD profiles reflect low temperature activation of C-H, N-O and C-O bonds leading to water and molecular hydrogen and, by inference, new surface heteroatom hydrocarbon intermediates. The H_2O desorption is reaction limited since the peak lies above 180 K, the temperature expected for desorption-limited water evolution [3.77] Disproportionation and hydrogenation of O-H contribute, the H coming from C-H bonds. Clearly, by 250 K the rate of C-H bond breaking increases the *local* concentration of $H_{(a)}$ to a level that makes recombination to form H_2 compete effectively with both hydrogentation of *t*-butoxy to form TBA and of OH to form H_2O. The water desorption rate maximizes (320 K) 20 to 50 K below the maximum desorption rates of H_2 (345 K) and TBA (350 K). There is a maximum in the 58 amu signal at 350 K due to acetone desorption. The next higher temperature desorption peak (400 K) occurs in the 30 amu spectrum. It is broadly distributed and assigned to desorption-limited NO since this range is typical for dosed NO.

Moving to higher temperature (460 K), there is a peak in 28 amu attributed to CO and a strong shoulder in 2 amu (H_2) ascribed to further C-H bond breaking. Overlapping these and peaking at 500 K, there are strong, nearly coincident desorptions of isobutene (56 amu) and TBA (59 amu). The CO peak occurs in the range where CO normally desorbs from Rh [3.78] but the overlap with acetone, isobutene and hydrogen desorption and, the relatively high onset temperature (400

K) make it likely that this CO desorbs in a reaction-limited process. The CO desorption continues up to about 600 K (vertical line) where N_2 desorption begins.

By 600 K, all desorption signals, except 28 amu have returned to background levels, i.e., no more C-H bonds to be broken. The high temperature 28 amu peaks are ascribed to CO formed by combining adsorbed C with residual adsorbed O (680 K) and to N atom recombination (800 K). Dissociation of NO on Rh is well-documented [3.26, 3.79-3.81]. As noted above, AES after heating to 900 K contains barely detectable amounts of C as the only contribution other than Rh.

Returning to the dose dependence, Figure 3.6, it is noteworthy that the 500 K TBA and butene intensities rise and saturate together. Similarly, the 350 K TBA and acetone peaks parallel each other. Taken with the other data, these results are describable by a reaction model that involves dissociation of weakly held, designated by subscript (p), $(CH_3)_3CONO_{(p)}$ into two intermediates. Figure 3.6 also indicates that the onset coverages differ, but only slightly, for the two pairs of product peaks. The 350 K, but not the 500 K, peaks are evident for a dose of 25 torr s, while for doses of 50 torr s and more, all the areas rise monotonically until saturation is reached at 200 torr s. Accounting for the scaling factors in Figure 3.6, the two peak area ratios—(350 K / 500 K) TBA and (acetone / isobutene)— uncorrected for ionization probabilities, are 5.5 and 11, respectively. Strikingly, the (acetone /

isobutene) ratio is a factor of 20 smaller for TBA dosed on O-covered Rh (see below).

Regarding acetone formation, a C_3 structure with oxygen bound to the central carbon atom, i.e., isopropoxy, is ruled out since it would lead to some isopropanol, contrary to observation. This points to a C_4 tertiary carbon structure. Two possibilities emerge—the oxametallacycle (1) [3.9, 3.12, 3.82-3.85] (Scheme 3.1), that we favor, and a structure that involves carbon-rhodium bonding and retention of O-H, i.e., either $HOC(CH_3)_2$- $C_{(a)}H_2$-Rh or $HOC(CH_3)_2$- $C_{(a)}H$=Rh. To form acetone from (1) relies on weakening the C—$C_{(a)}H_2$ bond and, in concert, strengthening the C-O bond. Forming acetone from the second possibility is much more complicated; C—C and O—H bond breakage must be catalyzed and a transient O—Rh bond must be formed.

The 500 K desorption of isobutene in competition with TBA suggests a second intermediate with the same C_4 carbon backbone as isobutene. Since there is significant $H_{(a)}$, the absence of isobutane evolution rules against *t*-butyl while the evolution of TBA certainly favors TBO. Further, the high temperature evolution of CO (680 K) is consistent with the presence of $O_{(a)}$ after all the $H_{(a)}$ is desorbed (> 600 K). The reaction path leading to isobutene likely involves a transition state (2) in which both the C—O and C—H bonds are elongated. The path to this configuration from TBO, would involve C—O elongation allowing transient bonding of the tertiary carbon to Rh while a γ C-H bond stretches to its breaking point [3.86, 3.87]

To summarize, all submonolayer TBN decomposes and can be described in terms of two C4 intermediates, TBO and an oxametallacycle (1) accompanied by NO. NO partially dissociates to N(a) and O(a). N(a) leaves the surface as N_2 at 800 K, and O(a) as H_2O or CO. We propose that the oxametallacycle (1) dehydrogenates selectively to form acetone at 350 K while *t*-butoxy remains to 500 K where it decomposes to isobutene via the proposed intermediate (2) and other C_xH_y fragments most of which react with $O_{(a)}$.

3.4.2.2 TBA on Rh without $O_{(a)}$

For comparison, we briefly examined TBA chemistry on clean and O-covered Rh foil. On clean Rh up to monolayer coverage, most of the TBA decomposes and TOFMS-TPD is dominated by H_2, CO and small amounts of H_2O and CO_2 (see Figure 3.7 for a dose of 60 torr s, 2.5×10^{15} molecules). No hydrocarbon or other oxygen-containing species desorb up to 950 K; in particular, there is no acetone or isobutene desorption. After TPD, AES shows only C and the atomic ratio, C/Rh, is 0.15, more than three fold higher than that following TPD of TBN on Rh.

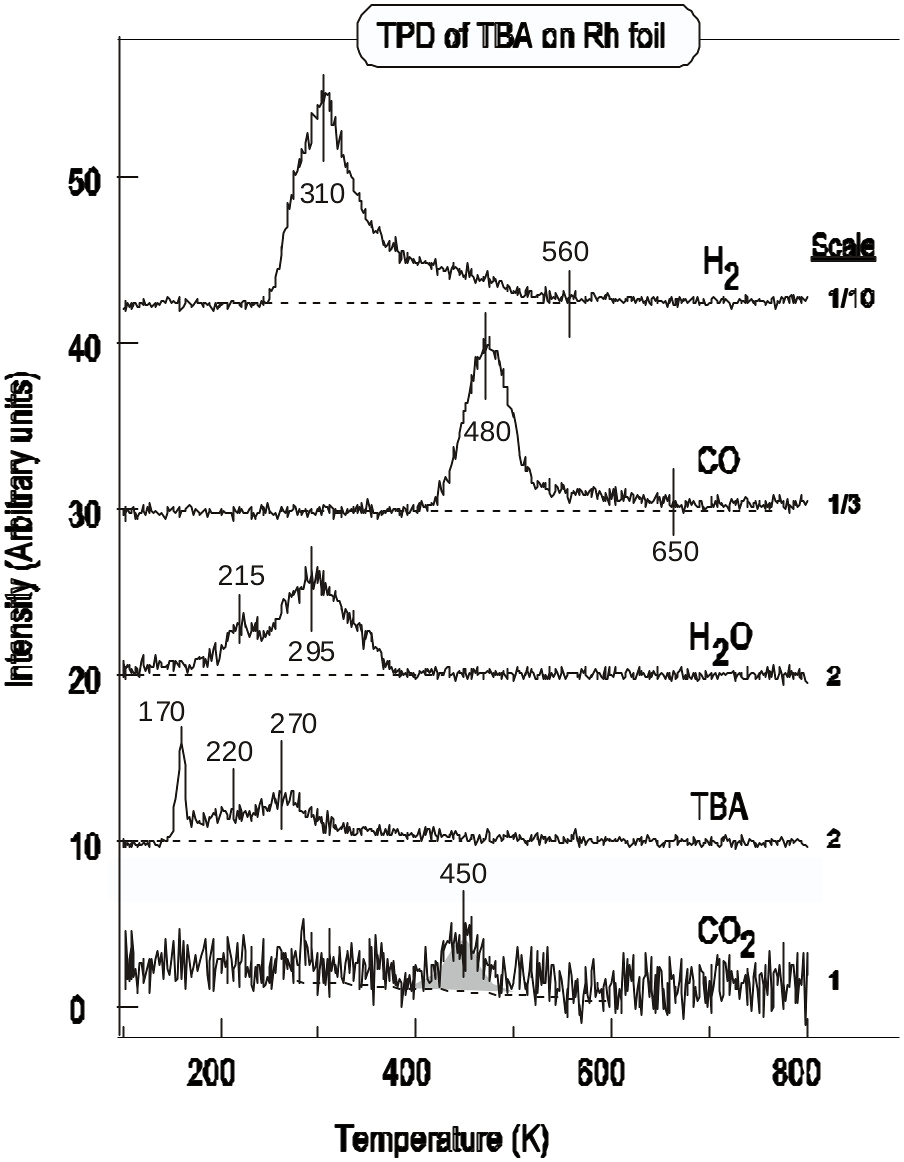

Figure 3.7: TOFMS-TPD (4.0 K s^{-1}) of *tert*-butyl alcohol (TBA) dosed on clean Rh at 100 K. The dose was 60 torr·s (2.5 x 10^{15} molecules). As operationally defined in the text, 1 monolayer dose is 70 torr·s. The pressure used to calculate the dose is that behind a calibrated leak, not the local pressure at the substrate.

The TBA desorption spectrum (Figure 3.7) has three peaks --170, 220 and 270 K. The 170 K peak is multilayer desorption, consistent with reports for TBA on Rh(111) (180 K), Pt(111) (160 K), Ag (111) (190 K), and Cu(110) (180 K) [3.9-3.14]. The other two peaks come from TBA in contact with Rh. One monolayer of TBA is defined *operationally* as the dose (70 torr s = 2.9×10^{15} molecules) that saturates the 270 K peak. There is some multilayer desorption at 170 K before the 270 K peak saturates. Assuming the TBA sticking coefficient is constant during dosing at 100 K, we conclude that 92% of monolayer (as defined above) TBA dissociates. This result arises by comparing the TBA peak area for a 70 s dose with the difference in TBA peak areas for two doses in the multilayer regime that differ by 70 torr s (not shown). The data of figure 3 differ from those on single crystal Rh(111) in that for the latter, there is a small TBA peak at 330 K assigned to *t*-butoxy hydrogenation [3.9]. Apparently, non-(111) sites on this clean Rh foil lower the activation energy for decomposition of TBO.

The strongest desorption peak of dihydrogen occurs at 310 K. This peak is ascribed to H atom recombination [3.88], and follows second order kinetics (not shown). C—H bond cleavage leads to the tail between 400 and 560 K of the 310 K H_2 desorption. This is the typical C—H bond breaking regime of alkyls on Rh [3.89].

Water is evolved with peaks at 215 and 295 K. Water dosed on Rh(111) desorbs at 180 K [3.77] and shifts to 207 K in the presence of co-adsorbed CO [3.90]. We assign the 215 K peak as desorption-limited monolayer water coming mostly from an impurity in TBA, rather than decomposition of TBA. In the range of 230 to 380 K, water desorption is reaction limited, and occurs as the result of C—O and C—H bond scission. In contrast, there is no evidence for C—O bond scission at or below 230 K in the TPD of 1-propanol [3.31] and 2-propanol [3.91] dosed on clean Rh(111). For TBA, C—O bond scission may be assisted by the tendency of the tertiary C to bond to Rh. In primary and secondary alcohols, the a C can form a C-Rh bond by breaking a C—H bond, releasing H while maintaining the C—O bond, albeit weakened. As for TBN, the dihydrogen desorption from TBA occurs at higher temperatures than water desorption.

Carbon monoxide peaks at 480 K, and there is a weak carbon dioxide peak at 450 K. Recognizing that the CO desorption peak temperature is consistent with that found on Rh(100) [3.78], and that most of adsorbed oxygen is consumed by hydrogen, it is still plausible that CO desorption is reaction-limited since it overlaps with the high temperature tail of dihydrogen desorption. While CO_2 may come from the disproportionation reaction, $2C_{(a)}O \rightarrow CO_{2(g)} + C_{(a)}$, unidentified residual $C_xH_yO_z$ species or from residual atomic oxygen, it is more likely that at this temperature (> 400 K) an oxametallocycle, i.e., di-σ-dimethyl methoxy (**4**) (see

Scheme 3.2), is formed transiently and, without significant delay, undergoes dehydrogenation accompanied by C—C bond breaking and release of CO. From the same intermediate, some C—O bond scission could release O to form CO_2.

To summarize for TBA dosed on clean Rh, partial dehydrogenation occurs below 230 K and some C—O bonds break at 230 K. At higher temperatures, the remaining $C_xH_yO_z$ species decompose and rearrange to release CO, CO_2, H_2O and H_2, leaving only carbon on the surface at 900 K.

3.4.2.3. TBA on O-covered Rh

When 60 torr s (2.5 x 10^{15} molecules) of TBA is dosed on Rh pre-covered with 0.66 of saturation $O_{(a)}$ (based on TPD), the TPD exhibits features summarized in Figure 3.8. Based on fragmentation pattern analysis, the peaks are assigned to TBA at 170, 270 and 380 K, acetone at 380 K, isobutene at 380 K, CO_2 at 420 K, CO at 420 and 680 K, H_2O at 210 and 410 K and, in very tiny amounts, H_2 between 350 and 450 K. Unlike TBA on clean Rh, significant amounts of acetone and isobutene desorb. Further, the amount of CO_2 desorbed is larger, and the amounts of H_2 and CO desorbed are smaller. Significantly, after TPD, $O_{(a)}$ not $C_{(a)}$ remains (AES not shown).

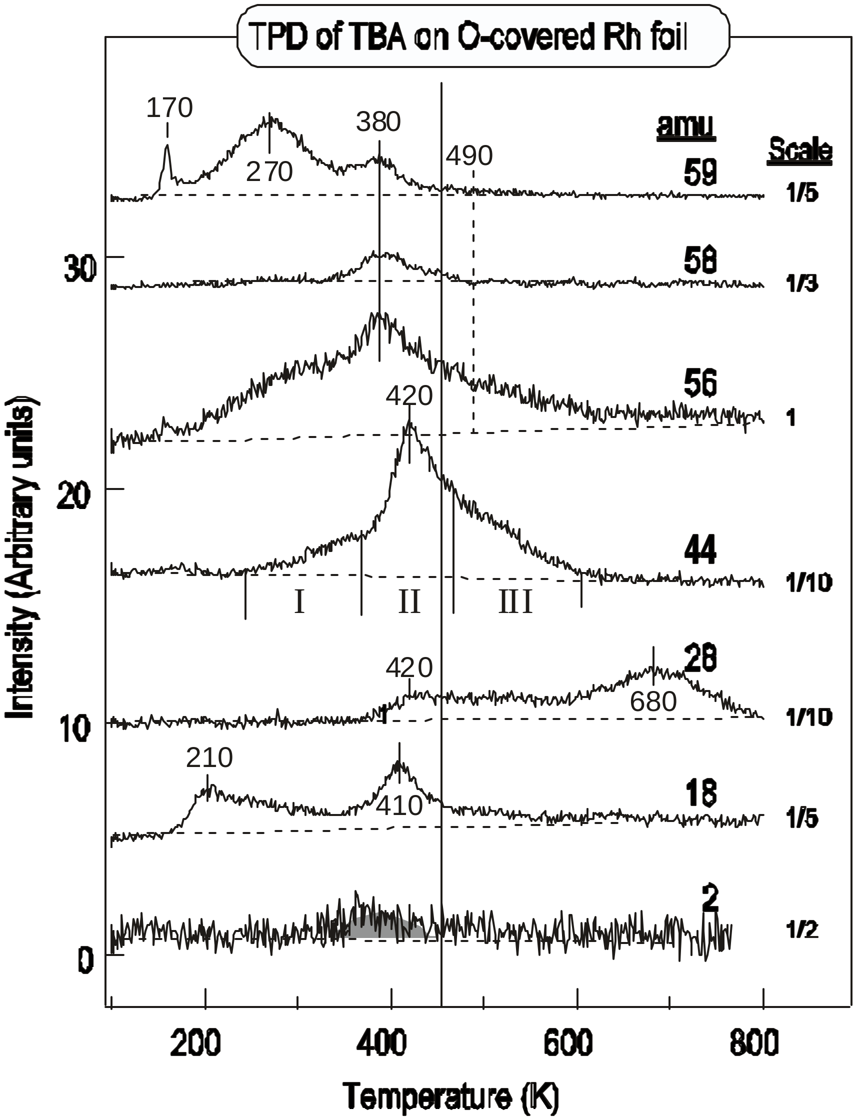

Figure 3.8. TOFMS-TPD (4.0 K s^{-1}) of 60 torr·s (2.5 x 10^{15} molecules) of TBA dosed on O-covered Rh at 100 K. Preadsorbed $O_{(a)}$ amount is 0.66 of saturation. A monolayer dose of TBA is 70 torr·s. The pressure used to calculate the dose is that behind a calibrated leak, not the local pressure at the substrate.

Compared to TBN on clean Rh (Figure 3.5), the temperature and intensity differences of the acetone and butene desorption peaks are most noteworthy. On TBN the butene desorption peaks 120 K higher (500 versus 380 K) while acetone desorption peaks slightly lower (350 versus 380 K). Noted above, the product distributions differ strongly; for TBA on O-covered Rh the (acetone / butene) peak area ratio is 0.5, while for TBN on Rh this ratio is 20-fold higher.

In Figure 3.8, there are TBA peaks at 170, 270 and 380 K. As for TBA on clean Rh, the 170 K peak is attributed to multilayer sublimation, and the 270 K peak to monolayer TBA desorption in the presence of dissociated fragments. Using the procedure described above, 68% of monolayer TBA dissociates compared to 92% on clean Rh. The 380 K TBA peak is not found for TBA dosed on clean Rh. In agreement with studies on O-covered Rh(111) [3.9], this peak is ascribed to hydrogenation of TBO. The 270 K peak area is five-fold larger than the 380 K peak indicating that most *t*-butoxy species decompose below 350 K.

Interestingly and unlike TBN and TBA on clean Rh (Figures 3.5 and 3.7), there is very little dihydrogen desorption for TBA on O-covered Rh (Figure 3.8). On the other hand, the CO_2 desorption is higher and the H_2O evolved is shifted to higher temperatures than for the other two cases. These differences reflect the higher chemical potential of $O_{(a)}$ compared to TBA or TBN dosed on Rh without $O_{(a)}$. There is enough oxygen to: (1) promote alcoholic O-H bond breaking to form

$(CH_3)_3CO_{(a)}$ and $O_{(a)}H$, (2) promote C-H bond breaking below 270 K thereby enhancing the rehydrogenation of neighboring *t*-butoxy groups, (3) favor formation of CO_2 rather than CO, (4) allow for the high temperature oxidation of $C_{(a)}$ leaving $O_{(a)}$, rather than $C_{(a)}$, at 800 K. It is noteworthy that no CO_2 desorbs during TPD of TBN (Figure 1) indicating that, in that case, there is never sufficient $O_{(a)}$ to form CO_2 in competition with other reactions.

Our results (Figure 3.8) are consistent with hydrogen for the 210 K water peak coming from O—H not C—H dissociation [3.9]. While for TBN, the onset (180 K) of H_2O desorption is nearly the same as for the other two cases, there is no peak at 210 K. This is not surprising since there are no O—H bonds in TBN, so very little $H_{(a)}$ is available at these low temperatures.

CO shows two peaks in Figure 3.8. $C_{(a)} + O_{(a)}$ accounts for the peak at 680 K whereas that at 420 K is the result of C-CO bond breaking. The latter occurs in the presence of $O_{(a)}$ and CO desorbs in competition with its oxidation to CO_2 [3.92]. The broad CO_2 profile is separable into three parts: (I) 240 to 380 K, (II) 380 to 460 K, and (III) 460 to 600 K (marked in Figure 3.8). The CO_2 signal rises slowly in I, exhibits a sharp peak in II, and undergoes a steady decay in III. Parenthetically, the desorption of CO_2 dosed on clean Rh(111) has a broad peak at 280 K [3.93]. The evolution of CO_2 in region I reflects low temperature C—C and C—H bond cleavage. Increasing the initial oxygen coverage to saturation (not shown) leads to less CO_2 desorption because there are fewer Rh sites available for C—C and C—H bond cleavage. In region II, C—H bond breaking becomes rapid and there is sufficient oxygen to oxidize both carbon and hydrogen to form CO_2, CO and H_2O. In region III the falling edge of CO_2 overlaps with the leading edge of the 680 K CO peak indicating, not surprisingly, that surface carbon is very heterogeneously distributed so that oxidation continues between 400 and 760 K.

Careful examination of the fragmentation pattern at 380 K (not shown) indicates that both isobutene and acetone are desorbed at 380 K. The 56, 58 and 59 amu signals all rise together, but the falling edge of 56 amu (isobutene-dominated) is much slower than 59 and 58 amu. The relative intensities of these three signals also vary with dose reflecting multiple desorbing species. From an extensive analysis of the TOFMS-TPD data set, including the TBA fragmentation pattern at 170 K, we deduce that some TBA desorbs with the acetone and isobutene. From Figure 3.8, we then conclude that isobutene desorption, but not acetone, extends through region III of the CO_2 desorption.

Between 360 and 460 K, the (acetone / isobutene) ratio remains constant to within 15% pointing to a common transition state formed from *t*-butoxy. The oxametallacycle (1) proposed for TBN dissociation is satisfactory but reacts quickly (does not accumulate); it has the same carbon skeleton as isobutene and its oxygen is bound in a position favorable for acetone formation. The absence of isobutene at

380 K in the case of TBN, and its presence for TBA on O-covered Rh, can be accounted for on the basis of the local chemical potential of $O_{(a)}$. In the absence of $O_{(a)}$, i.e., TBN on Rh, the activation energy required for C—O bond breaking exceeds that for C—Rh cleavage whereas in the presence of $O_{(a)}$, i.e., TBA on O-Rh, these become more nearly equal.

To summarize, for TBA dosed on O-covered Rh, TBA desorption competes with *t*-butoxy formation. *t*-Butoxy remains up to 350 K, and reacts to form acetone, isobutene and TBA via the short-lived oxametallacycle (1). Combustion reactions forming CO_2 and H_2O compete.

3.4.3 Reaction pathways

With the foregoing results in hand, we turn to proposed reaction paths for TBN on Rh and TBA on O-covered Rh (schematically depicted in Figures 3.9 and 3.10). As indicated schematically in Figure 3.9, we speculate that prior to reaching 200 K, adsorbed TBN passes through a transition state with a geometry intermediate between the *cis* and *trans* forms of TBN. Any such path will move the external O closer to the H of CH_3. Tilting the CONO plane towards the Rh surface then brings an intermediate that can relax along one of two paths. The first involves passage through a *cis*-like configuration to form the oxametallacycle (1) while the other passes through a *trans*-like configuration to form *tert*-butoxy. Both dissociation products are located in environments that contain adsorbed and dissociated NO. Likely, the C-H bond cleavage required to form (1) is assisted by bringing the C-H bond into close proximity to the external O of TBN. We propose that (1) is stable, coexists with *tert*-butoxy, accumulates to spectroscopically observable concentrations, and rearranges to desorb acetone and TBA beginning at ~ 300 K. Further, because the local environment contains NO and N, *tert*-butoxy does not begin to rearrange until much higher temperatures (~ 500 K), i.e. after neighboring NO has desorbed opening metal sites for γ-C-H activation. Unlike (1) (Scheme 3.1), only γ-H exists in *t*-butoxy and its activation transiently forms a structure (2) similar to (1). At these elevated temperatures it does not accumulate because C-O cleavage is activated. Alternatively, *t*-butoxy activation could occur via an intermediate complex (3) analogous to well-known β-H dehydrogenation [3.93]. The contributions of these two paths will depend on the orientation of *t*-butoxy and the surface dehydrogenation activity. While γ-elimination is still not well understood, it is known that C—H bond cleavage is not the rate-determining step, and a weakened C-O bond, as in (5), can facilitate γ-elimination from *tert*-butoxy [3.86, 3.87].

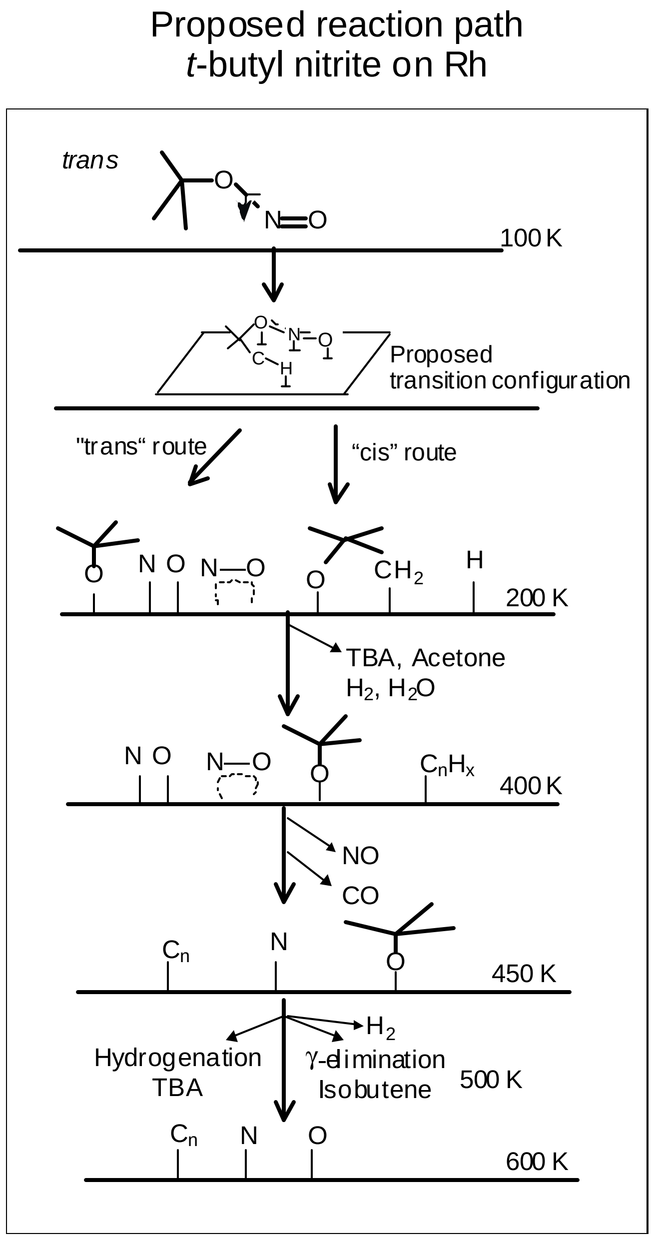

Figure 3.9: Proposed reaction paths of TBN on clean Rh.

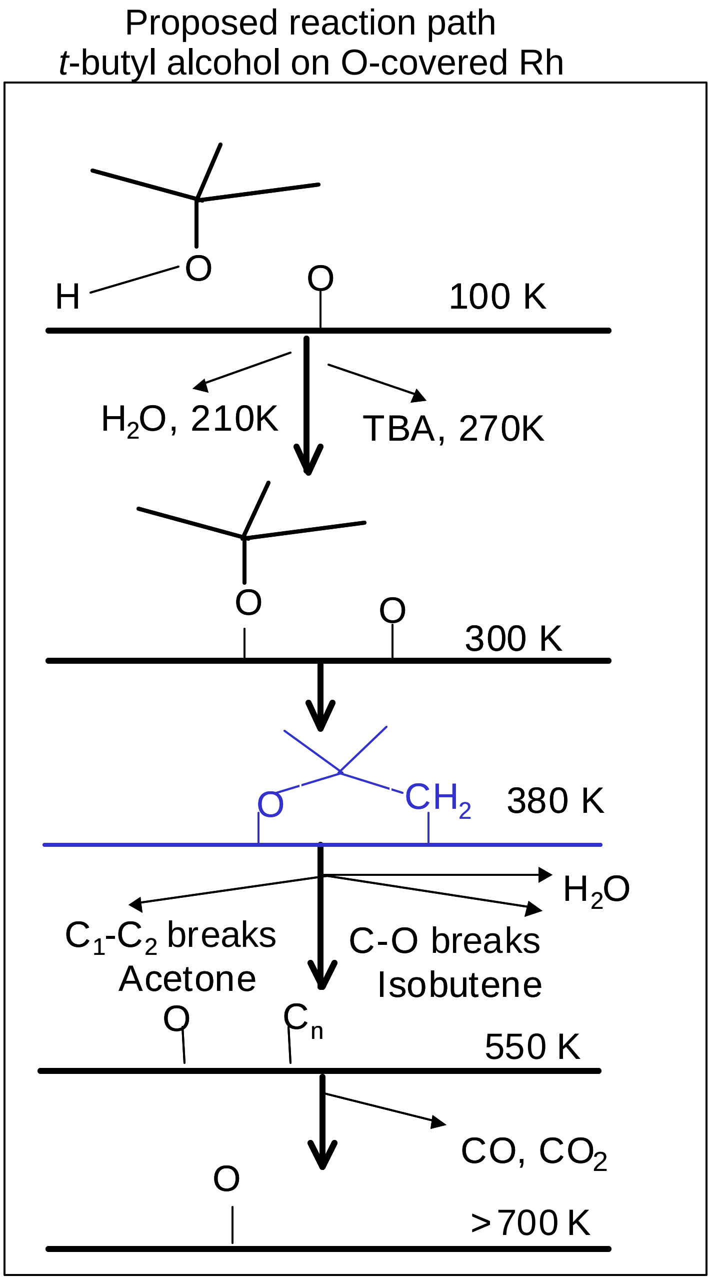

Figure 3.10: Proposed reaction paths of TBA on O-covered Rh.

(5)

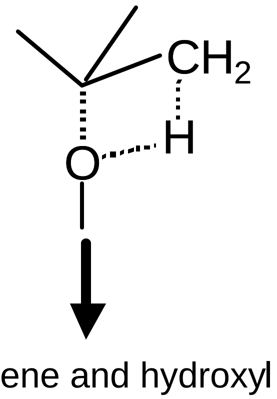

The situation for TBA on O-covered Rh is different. Following previous work [3.9], we propose, as diagrammed in Figure 3.10, that TBA reacts selectively to form *t*-butoxy on O-covered Rh. The surface hydrogen from O—H bond cleavage reacts exclusively with surface oxygen to form water that desorbs below 300 K. *tert*-Butoxy remains up to ~380 K, where coadsorbed oxygen facilitates oxydehydrogenation, i.e. the oxametallacycle (1) forms transiently via an oxygen-assisted mechanism (Scheme 3.4) [3.13]. From this transient configuration both acetone and isobutene desorb.

Scheme 3.4 Oxygen-assisted Oxametallacycle Formation

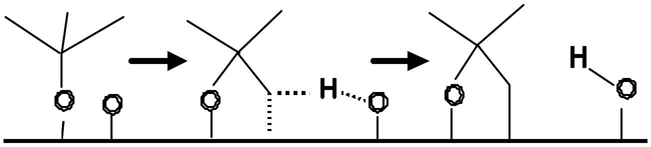

Hydrogenation of *t*-butoxy to release TBA and combustion to form CO_2 and H_2O all compete. Above 550 K, only oxygen and surface carbon remain. The latter is removed as CO at 680 K leaving an oxygen residual at 800 K.

3.5 DISCUSSION

3.5.1 Comparison of TBN on Cu(111) and TBA on O-covered Cu(110)

The differences between TBN on Cu(111) and TBA on O-covered Cu(110) [3.14] are significant. At low temperatures (<300 K), TBO from TBA on O-covered Cu(110) does not decompose to C1 and C2 species like TBN on Cu(111). At high temperature, TBO dissociates unimolecularly to form TBA, isobutene and water in TBA on O-covered Cu, but undergoes a bimolecular reaction to form TBA, isobutene and adsorbed oxygen for TBN on Cu(111). These differences are attributed to the surface concentration difference of adsorbed TBO and the TBO to oxygen ratio.

Due to the low dehydrogenation catalytic activity of copper, co-adsorbed oxygen is necessary to generate TBO from TBA on copper. Hydrogen transfers from oxygen in TBA to adsorbed oxygen. Each TBA needs one adsorbed oxygen. The oxygen in TBN comes from the dissociation of NO, and its amount can be estimated from the N_2O and N_2 desorption peak areas as described before. The final estimated TBO to $O_{(a)}$ ratio is 1.2:1 for 0.5 L TBN on Cu(111). The difference of TBO concentration itself is also significant. Since there is no TBN monolayer desorption, all first layer TBN adsorbs dissociatively on Cu(111), but strong monolayer desorption at 220K shows that many intact TBA molecules desorb from O-covered Cu(110). Significant mode softening has been reported for the methyl C-H vibrations on Cu(111) [3.51, 3.95, 3.96], Cu(100) [3.50] and Ni(111) [3.53]. Theoretical calculations interpret the softening effect as metal-to-methyl charge donation into a C-H antibonding orbital [3.48]. Co-adsorbed oxygen can withdraw electron from metal and, thus, inhibit the electron donation to C-H antibonding orbital, thereby attenuating the dehydrogenation ability of copper. Meanwhile, increasing the TBO coverage can increase copper dehydrogenation ability since the strong nucleophilic tert-butyl group can donate electron density from its bonding orbitals to the metal. More TBO and less oxygen makes TBO(I) occur at low temperature in TBN on Cu(111) but not TBA on Cu(110). Low TBO concentration also makes the bimolecular reaction less favorable on O-covered Cu(110). The mismatch of TBA and isobutene desorption in their tailing edges (Figure 3.3) indicates the reaction is not the same as proposed in Scheme 3.1 when less TBO presents on the surface.

3.5.2 Comparison of TBN on Rh and on Pt(111).

Comparing TBN on Pt(111) [3.12] and Rh, there is evidence for tert-butoxy and the oxametallacycle (1) on both. Outstanding among the differences is the absence of acetone and butene desorption from Pt(111). While the underlying reasons remain to be clarified, we note that dissociation of NO on Pt is much less likely compared to Rh and, thus, the transition configurations of the TBN may differ on the two substrates. Although the intrinsic dehydrogenation activities of Rh and Pt are similar, the atomic N and O, produced by NO dissociation on Rh, but not Pt, may locally passivate Rh atoms and help stabilize (1).

3.5.3 The formation of acetone on Rh

To form acetone (C_3H_6O) from (**1**), 1 C and 2 H must be removed. The simplest path is to remove methylene (= CH_2) to form η^2–dimethyl methyleneoxy (**3**) and then break the C-Metal bond and desorb. In a second path, methyl is removed and supplies hydrogen for the group left behind (Scheme 3.5). This path forms an enol, CH_3COHCH_2, which could reconstruct to acetone readily. The methylene path is preferred because γ-H-elimination in forming the enol is expected to require higher activation energy than the methylene path. By the same argument, 2-oxy-propene (**6**) cannot form on Cu(111), forcing C-C cleavage to form either η^2–dimethyl methyleneoxy (**3**) that leads to acetone or di-σ-dimethyl methoxy (**4**) that undergoes further C-C cleavage. These two paths have similar activation energies, and which one dominates depends upon both the surface steric effect and the stability of the products. Apparently, the di-σ-dimethyl methoxy path requires more surface sites; and its products also more stable since it occurs below room temperature on less active Cu(111) and acetone evolution occurs at 350 K on very active Rh. Due to the high dehydrogenation ability of Rh, methylene dehydrogenates extensively and the active surface sites are quickly occupied, and then the η^2–dimethyl methyleneoxy channel opens to form acetone. However, this channel is always forbidden on copper because (1) high oxygen affinity makes the Cu-O bond breaking unfavorable, (2) breaking a C=O bond via a γ-H-elimination to generate propene is highly endothermic, and (3) methylene coupling to volatile C2 species keeps enough surface active sites. In short, the differences of Rh and Cu regarding dehyrogenation ability and oxygen affinity make the η^2–dimethyl methyleneoxy path difficult on copper but facile under certain conditions on rhodium.

Scheme 3.5: two possible paths of acetone formation

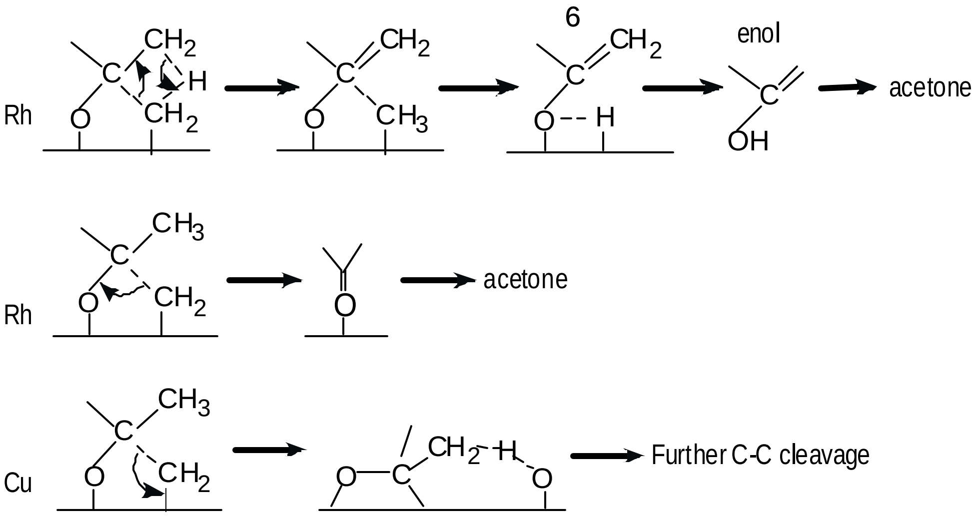

3.6 SUMMARY AND CONCLUSIONS

The TOFMS-TPD and AES investigation of tert-butyl nitrite ($(CH_3)_3O$-NO) on Cu(111) and Rh, and TBA on clean and oxygen-covered Rh leads to the following conclusions:

1) During adsorption at 100 K and subsequent TPD, tert-butyl nitrite breaks its internal N-O bond to form tert-butoxy ($(CH_3)_3O_{(a)}$-) and NO. NO decomposes to N_2O and N_2 that desorb at 194 K, and to adsorbed N and O. Some tert-butoxy decomposes at fair low temperature (<240 K) to form water, carbon monoxide, carbon dioxide, acetylene, proposed imide and acetate, and the reminder disproportionates to tert-butyl alcohol, isobutene

and adsorbed oxygen at 610 K. The pathways of tert-butoxy reacton at low temperature are proposed to be initialized by C-H cleavage followed by C-C bond breaking to form adsorbed methylene. The methylene couples to di-σ-bonded ethylene, which can either dehydrogenate to acetylene desorbing at 335 K via a vinyl intermediate or be partially oxidized to acetate that dissociates at 580 K. There is also evidence of NH bond formation during this process. The high temperature tert-butoxy decomposition is a bimolecular reaction involving directly hydrogen intermolecular transfer. A comparison with TBA on O-covered Cu(110) was made, and their differences are attributed to the different surface concentrations of adsorbed TBO and oxygen on two surfaces.

2) On a clean Rh surface, TBA dehydrogenates non-selectively to form H_2, H_2O, CO and surface carbon.

3) On O-covered Rh, TBA dissociates between 200 and 300 K by breaking the O—H bond to form TBO. TBO decomposes at 380 K to form and desorb isobutene and acetone in competition with hydrogenation of TBO to reform TBA. Combustion reactions forming CO_2 and H_2O also participate. Compared to TBA dosed on clean Rh, co-adsorbed oxygen facilitates the selective formation of TBO and subsequent decomposition through the transient formation of (**1**).

4) TBN dissociates on Rh to form NO and two intermediates, a relatively stable oxametallacycle (1) and TBO. At 350 K, (1) reacts via C—H bond activation to yield acetone. Unlike the TBA case, TBO formed from TBN is stable to 500 K where it rearranges via ?-H bond cleavage to form isobutene. The differences in the behavior of intermediates related to *t*-butoxy formed from TBA and TBN are attributed to differences in the local chemical environments, e.g., H, NO, OH and O, that lead to different surface configurations and reaction paths.

3.7 REFERENCES

[3.1] Weissermel, K.; Arpe, H.-J. *Industrial organic chemistry*, 3rd Edition, Weinheim, New York, 1997

[3.2] Wachs, I.E.; Madix, R.J. *Surf. Sci.* **1978**, *76*, 531

[3.3] Weldon, M. K.; Friend, C. M. *Chem. Rev*. **1996**, 96, 1391

[3.4] Bowker, M.; Madix, R. J. *Surf. Sci.* **1982**, 116(3), 549

[3.5] Bowker, M.; Madix, R. J., *Surf. Sci.* **1980**, 95(1), 190

[3.6] Davis, J. L.; Barteau, M. A. *Surf. Sci.* **1987**, 187(2-3), 387

[3.7] Ali, Ali H.; Zaera, F. *J. Molecular Catalysis A: Chemical* **2002**, 177(2), 215

[3.8] Ihm, H.; Scheer, K.; Celio, H.; White, J. M. *Langmuir* **2001**, 17, 786

[3.9] Xu, X.; Friend, C. M. *Langmuir* **1992**, 8, 1103.

[3.10] Bol, C.W.J.; Friend, C.M. *Surf. Sci.* **1996**, *364*, L364

[3.11] Xu, X.; Friend, C. M. *J. Phys. Chem.* **1991**, 95, 10753

[3.12] Ihm, H.; Medlin, J. W.; Barteau, M. A.; White, J. M. *Langmuir* **2001**, 17, 798

[3.13] Brainard, R. L.; Madix, R. J. *J. Am. Chem. Soc.* **1989**, 111, 3826

[3.14] Brainard, R. L.; Madix, R. J. *Surf. Sci.* **1989**, 214, 396

[3.15] Shelef, M. *Chem. Rev.* **1995**, 95(1), 209

[3.16] Jang, B.W.L.; Spiver, J.J.; Kung, M.C.; Yang, B.; Kung, H.H. *ACS Symposium Series* **1995**, 587, 83

[3.17] Burch, R.; Breen, J. P.; Meunier, F. C. *Appl. Catal. B* **2002**, 39(4), 283

[3.18] Konin, G. A.; Il'ichev, A. N.; Matyshak, V. A.; Khomenko, T. I.; Korchak, V. N.; Sadykov, V. A.; Doronin, V. P.; Bunina, R. V.; Alikina, G. M.; Kuznetsova, T. G.; Paukshtis, E. A.; Fenelonov, V. B.; Zaikovskii, V. I.; Ivanova, A. S.; Beloshapkin, S. A.; Rozovskii, A. Ya.; Tretyakov, V. F.; Ross, J. R. H.; Breen, J. P. *Topics in Catalysis* 2001, 16/17(1-4), 193

[3.19] Kung, M. C.; Bethke, K. A.; Yan, J.; Lee, J.-H.; Kung, H. H. *Appl. Surf. Sci.* **1997**, 121/122, 261

[3.20] Nyarady, S. A.; Sievers, R. E. *J. Am. Chem. Soc.* **1985**, 107(12), 3726

[3.21] Kameoka, S.; Ukisu, Y.; Miyadera, T. *Phys. Chem. Chem. Phys.* **2000**, 2(3), 367

[3.22] Haneda, M.; Kintaichi, Y.; Inaba, M.; Hamada, H. *Bull. Chem. Soc. Jpn.,* **1997**, 70, 499

[3.23] Montreuil, C. N.; Shelef, M. *Appl. Catal.* **1991**, 75, L1

[3.24] Sexton, B. A. *Surf. Sci.* **1979**, 88, 299

[3.25] Camplin, J. P.; McCash, E. M. *J. Chem. Soc. Faraday Trans.* 1996, 92, 4695

[3.26] Brown, W. A.; King, D. A. *J. Phys. Chem. B* **2000**, 104, 2578

[3.27] Davis, M.E.; Suib, S.L. *Selectivity in Catalysis*; American Chemical Society: Washington, DC, 1993

[3.28] Houtman, C.J.; Barteau, M.A. *Langmuir* **1990**, *6*, 1558

[3.29] Houtman, C.J.; Barteau, M.A. *J. Catal.* **1991**, *130*, 528

[3.30] Papageorgopoulos, D. C.; Ge, Q.; King, D. A. *Surf. Sci.* **1998**, 397(1-3), 13

[3.31] Brown, N.F.; Barteau, M.A. *Langmuir* **1992**, *8*, 862

[3.32] Kim, C.; Yan, X. M.; White, J. M. *Rev. Sci. Instrum.* **2000**, 71, 3505

[3.33] Habraken, F. H. P. M.; Kieffer, E. P.; Bootsma, G. A. *Surf. Sci.* **1979**, 83(1), 45

[3.34] Lee, I.; Kim, S. K.; Zhao, W.; White, J. M. *Surf. Sci.* **2002**, 499(1), 53

[3.35] Lascovich, J. C.; Giorgi, R.; Scaglione, S., *Appl. Surf. Sci.*, **1991**, 47(1), 17

[3.36] Patsalas, P.; Handrea, M.; Logothetidis, S.; Gioti, M.; Kennou, S.; Kautek, W. *Diamond and Related Materials* **2001**, 10(3-7), 960

[3.37] Madix, R. J. *Surface reactions* Chapter 2, Berlin; New York : Springer-Verlag, 1994

[3.38] Berko, A.; Solymosi, F. *Appl. Surf. Sci.* **1992**, 55(2-3), 193

[3.39] Anger, G.; Winkler, A.; Rendulic, K. D. *Surf. Sci.* **1989**, 220, 1

[3.40] Kammler, Th.; Kuppers, J. *J. Chem. Phys.* **1999**, 111(17), 8115

[3.41] Kirstein, W.; Kruger B.; Thieme, F. *Surf. Sci.* **1986**, 176, 505

[3.42] Fu, S. S.; Somorjai, G. A. *Langmuir* **1992**, 8, 518

[3.43] Thiel, P. A.; Madey, T. E. *Surf. Sci. Rep.* **1987**, 7(6-8), 211

[3.44] Kammler, Th.; Kuppers, J. *J. Phys. Chem. B* **2001**, 105, 8369

[3.45] Outka, D. A.; Friend, C. M.; Jorgensen, S.; Madix, R. J. *J. Am. Chem. Soc.* **1983**, 105, 3468

[3.46] Avery, N. R. *J. Am. Chem. Soc.* **1985**, 107, 6711

[3.47] Zaera, F.; Tjandra, S. *J. Am. Chem. Soc.* **1993**, 115, 5851

[3.48] Bent, B. E. *Chem. Rev*. 1996, 96(4), 1371

[3.49] Solymosi, F. *J. Mole. Catal. A.* **1998**, 131, 121

[3.50] Lin, J.-L.; Chiang, C.-M.; Jenks, C. J.; Yang, M. X.; Wentzlaff, T. H.; Bent, B. E. *J. Catal.* **1994**, 147(1), 250

[3.51] Chiang, C.-M.; Bent, B. E. *Surf. Sci.* **1992**, 279, 79

[3.52] Shustorovich, E.; Bell, A. T. *Surf. Sci.* **1991**, *248*, 359

[3.53] Yang, Q. Y.; Maynard, K. J.; Johnson, A. D.; Ceyer, S. T. *J. Chem. Phys.* **1995**, 102, 7734

[3.55] Kovacs, I.; Solymosi, F. *J. Mole. Catal. A* **1999**, 141, 31

[3.56] Stuve, E. M.; Madix, R. J.; Sexton, B. A. *Surf. Sci.* **1982**, 119(2-3), 279

[3.57] Au, C. T.; Roberts, M. W. *Chem. Phys. Lett.* **1980**, 74(3), 472

[3.57] Russell, J. N., Jr.; Gates, S. M.; Yates, J. T., Jr.. *Surf. Sci.* **1985**, 163, 516

[3.58] Bowker, M.; Madix, R. J., *Surf. Sci.* **1981**, 102, 542

[3.59] Bowker, M.; Madix, R. J. *Applications Surf. Sci.* **1981**, 8, 299

[3.60] Surman, M.; Lackey D.; King, D. A. *J. Electron Spectroscopy and Related Phenomena* **1986**, 39, 245

[3.61] Zhu, X. Y.; White, J. M. *Catal. Lett.* **1988**, 1(8-9), 247

[3.62] Pallassana, V.; Neurock, M.; Lusvardi, V. S.; Lerou, J. J.; Kragten, D. D.; Van Santen, R. A. *J. Phys. Chem. B* **2002**, 106(7), 1656

[3.63] Hwang, C.-H.; Lee, C.-W.; Kang, H.; Kim, C. M. , Surf. Sci. **2001**, 490(1-2), 144

[3.64] Livneh, T.; Asscher, M. *J. Phys. Chem. B* **2000**, 104(14), 3355

[3.65] McCash, E. M. *Vacuum* **1990**, 40, 423

[3.66] Nyberg, C.; Tengstaal, C. G.; Andersson, S.; Holmes, M. W *Chem. Phys. Lett.* **1982**, 87, 87

[3.67] Arvanitis, D.; Doebler, U.; Wenzel, L.; Baberschke, K.; Stoehr, J. *Surf. Sci.* **1986**, 178(1-3), 686

[3.68] Kubota, J.; Kondo, J. N.; Domen, K; Hirose, C. *J. Phys. Chem*. **1994**, 98, 7653

[3.69] Backx, C.; De Groot, C. P. M. *Surf. Sci*. **1982**, 115(2), 382

[3.70] Outka, D. A.; Madix, R. J. *J. Am. Chem. Soc*. **1987**, 109(6), 1708

[3.71] Yang, M. X.; Eng, J., Jr., Kash, P. W.; Flynn, G. W.; Bent, B. E. *J. Phys. Chem*. **1996**, 100, 12431

[3.72] Matloob, M. H.; Roberts, M. W. *J. Chem. Soc. Faraday Trans. I* **1997**, 73, 1393

[3.73] Asfin, B.; Davies, P. R.; Pashuski, A.; Roberts, M. W. *Surf. Sci*. **1991**, 259, L724

[3.74] Surman, M.; Solymosi, F.; Diehl, R. D.; Hoffman P., King, D. A. *Suf. Sci*. **1984**, 146, 144

[3.75] Lackey, D.; Surman, M.; King, D. A.; *Surf. Sci*. **1985**, 162, 388

[3.76] Zhao, W.; Kim, C.; White, J.M. *Surf. Sci.* **2000**, *451*, 267

[3.77] Wanger, F.T.; Moylan, T.E. *Surf. Sci.* **1987**, *191*, 121

[3.78] de Jong, A.M.; Niemantsverdriet, J.W. *J. Chem. Phys.* **1994**, *101*, 10126

[3.79] Siokou, A.; van Hardeveld, R.M.; Niemantsverdriet, J.W. *Surf. Sci.* **1998**, *402-404*, 110

[3.80] Bowker, M.; Guo, Q.; Joyner, R.W. *Surf. Sci.* **1991**, *257*, 33

[3.81] Borg, J.; Reijerse, J.F.C.-J.M; van Santen, R.A.; Niemantsverdriet, J.W. *J. Chem. Phys. 1994*, **101**, 10052

[3.82] Brown, N.F.; Barteau, M.A. *J. Phys. Chem.* **1996**, *100,* 2269

[3.83] Brown, N.F.; Barteau, M.A. *Surf. Sci.* **1993**, *298*, 6

[3.84] Jones, G.S.; Mavrikakis, M.; Barteau, M.A.; Vohs, J.M. *J. Am. Chem. Soc.* **1998**, 120, 3196

[3.85] Medlin, J. W.; Barteau, M. A.; Vohs, J. M. *J. Mol. Catal*. **2000**, 163, 129

[3.86] Wiegand, B.C.; Uvdal, P.E.; Serafin, J.G.; Friend, C.M. *J. Am. Chem. Soc.* **1991**, *113*, 6686

[3.87] Uvdal, P.; Wiegand, B.C.; Serafin, J.G.; Friend, C.M. *J. Chem. Phys.* **1992**, *97,* 8727

[3.88] Payne, S.H.; Kreuzer, H.J.; Frie, W.; Heinz, K. *Surf. Sci.* **1999**, *421*, 279

[3.89] Somorjai, G.A. *Introduction to Surface Chemistry and Catalysis;* Wiley-Interscience: New York, 1994

[3.90] Wanger, F.T.; Moylan, T.E.; Schmieg, S.J. *Surf. Sci.* **1988**, *195*, 403

[3.91] Xu, X.; Friend, C.M. *Surf. Sci.* **1991**, *260*, 14

[3.92] Au, C.; Liao, M.; Ng, C. *J. Phys. Chem. A* **1998**, *102*, 3959

[3.93] Dubois, L.H.; Somorjai, G.A. *Surf. Sci*. **1983**, *128*, L231

[3.94] Bochmann, M. *Organometallics: Complex with transition metal-carbon s-bonds*; Oxford University Press: Oxford, 1994

[3.95] Lin, J.-L.; Bent, B. E. *J. Vac. Sci. Tachnol. A* **1992**, 10, 2202

[3.96] Lin, J.-L.; Bent, B. E. *Chem. Phys. Lett.* **1992**, 194, 208

Chapter 4: nanoparticle formation of Ag deposition onto an ice layer on clean and modified oxide surfaces

4.1 OVERVIEW

As a strategy for synthesizing metal nanoparticles, thermally evaporated Ag atoms were deposited onto a thin (typically ~2 nm) solid water layer on amorphous HfO_2, $TiO_2(110)$ and trimethyl acetic acetate ($TMAA^-$) pre-saturated $TiO_2(110)$ at 55-125 K. Incident Ag atoms penetrate into the ice matrix but do not reach the underlying substrates. Subsequent thermal removal of water leads to Ag nanoparticle formation on the surfaces, revealed by atomic force microscopy (AFM) and scanning tunneling microscopy (STM). For 1.5 ML Ag onto 18L water on HfO_2, the average particle height is much larger and the number density of particles is much lower, 2×10^{10} cm^{-2}, compared to deposition and heating of the same amount of Ag on bare HfO_2. The average particle height is 5 times larger than the thickness of the original ice matrix. For Ag deposition onto 18 L water on $TiO_2(110)$, one dimensional strings of Ag nanoparticles form spontaneously, and are distributed randomly on the surface. Separated by the strings, a few large particles and crowed small particles coexist. No strings were observed with either 4 L or 60 L water exposure. For Ag deposition onto an ice layer on $TMAA^-$ saturated $TiO_2(110)$, a very few huge particles form and they have a height-to-radius ratio close to 1 form. These results for deposition onto ice are described qualitatively by a model that involves (1) formation, during Ag deposition, of a relatively homogeneous spatial distribution of tiny clusters, Ag_n; and (2) the competition of water dewetting and desorption.

4.2 INTRODUCTION

Ag, widely used in coins and photography, is also used in other technologies. For example, in heterogeneous catalysis, Ag is used for ethylene epoxidation [4.1, 4.2], alcohol partial oxidation [4.3], and NO_x reduction [4.4, 4.5]. Other applications involve use as a deoxygenation catalyst [4.6], semiconductor gas sensor additive [4.7], and antimicrobial agent [4.8]. The grain size of silver plays a crucial role in these heterogeneous reactions, e.g., in the partial oxidation of ethylene to epoxide, cesium additives are often used and the size of the Ag particles influences the type of Cs—O surface complexes [4.9].

Because of their unique electronic and structural properties [4.10, 4.11], considerable attention has been directed to nanoparticles, including those of Au and Ag for the partial oxidation of olefins at low temperatures [4.12, 4.13]. To avoid the effects of averaging over a broad distribution of particle sizes, which may lead to the competition between possible reaction pathways in catalysis, monodisperse distributions of nanoparticles are sought for basic research investigations. Another challenge is to prepare high number density particles for high specific area catalysts. Thus, as model system for heterogeneous catalysis, there is strong motivation to explore various means of preparing and characterizing a monodisperse set of controlled size nanoparticles spread over a macroscopic area of a planar oxide support.

One approach has made use of a 50 K Xe film as a matrix for vapor deposition of Ag [4.14]. After Xe evaporation, the Ag particle diameters were broadly distributed (5-15 nm) on silicon substrate. The distribution varied with the Xe matrix thickness and deposited Ag concentration, but not on the Xe removal rate.

In this chapter, a similar experiment is described that using H_2O(s), rather than Xe(s), as the solid for dissipating the incident energy of the thermally evaporated Ag atoms. Like Xe, H_2O does not react chemically with Ag and can be removed readily upon heating. Unlike a Xe lattice, the hydrogen bonded ice lattice is much stiffer and has a much higher heat capacity (2.07 J/gK at 160 K) than solid Xe (0.191 J/gK at 60 K). Thus, H_2O(s) will dissipate kinetic energy of hot Ag atoms more efficiently (at least 10x) than Xe(s). Supporting the use of H_2O(s), we note that, in a traditional matrix isolation experiment designed for optical spectroscopy, Ag atoms and small clusters (Ag_2-Ag_4) were trapped in an amorphous ice matrix by co-dosing silver monomers and water onto a NaCl substrate at 10 K [4.15]. During warming, Ag diffusion-aggregation occurred above 125 K at low Ag concentration (10^1-10^4 ppm) [4.15], a process likely accompanying phase changes in the ice matrix [4.16].

TiO_2(110) is one of the most intensively studied oxide surfaces [4.17], and has been widely used to model catalyst supporting oxides. TiO_2 itself is also used as a photocatalyst in solar cells for the production of hydrogen and electric energy [4.18]. Other applications related to surface chemistry include gas sensors [4.19], corrosion-protective coatings [4.20], and anti-fog windshields [4.21]. Stoichiometric TiO_2 is an insulator, but readily becomes semiconductive upon vacuum annealing so that it is suitable for STM and traditional surface science studies. During annealing transparent titania becomes blue and small amount of lattice oxygen desorbs, forming lattice oxygen vacancies both in bulk and on surface and forcing Ti^{4+} to reduce to Ti^{3+}. Surface oxygen vacancy, an electronphilic center, is believed to be the most active site and can dissociate O-H bonds. When hydroxyl containing species, such as H_2O and $(CH_3)_3COOH$, adsorb, the O-H bonds break, the O-containing fragments fill surface vacancy sites, and the hydrogen atoms bond to lattice oxygen atoms to form surface hydroxyl groups. On vacancy-free TiO_2(110), organic acids deprotonate by attacking five-coordinated Ti^{4+} using their carboxylic oxygen. For $(CH_3)_3CCOOH$, both its oxygen atoms enter the lattice and it becomes bi-dentate $–_{(a)}O(t\text{-}Bu)CO_{(a)}$ – finally [4.22], possibly via oxygen vacancy surface diffusion [4.23]. With high enough $(CH_3)_3CCOOH$ exposure, the bi-dentate $–_{(a)}O(t\text{-}Bu)CO_{(a)}$ – gives long range order and covers the whole titania surface densely with its tert-butyl group pointing out of the surface perpendicularly. Thus, an extremely hydrophobic surface forms.

As a good system to model catalysts, which commonly are nano particles or clusters spreading on oxide surfaces, the growth of Ag nanoparticles on TiO_2 has been studied intensively. At room temperature the growth is thermodynamically controlled, and nano particles grow along the step-edges [4.24] and at surface defect sites. At low temperature (~100 K) their growth is kinetically controlled, and nano particles spread evenly on the whole surface [4.25, 4.26]. In both cases, the most probably size of final particles has an upper limit of ~ 7 nm.

Unlike active TiO_2, hafnia (HfO_2) is relatively inert. Because Hf, Zr and Ti are in the same column of the periodic table, the structural properties of their oxides have many common features. These include relatively high dielectric constants that have motivated studies, in our labs [4.27] and many others [4.28], as high dielectric materials for the semiconductor industry. Thus, HfO_2 with its very high melting point (~3050 K) and excellent thermal stability can serve as a useful benchmark for comparison with TiO_2.

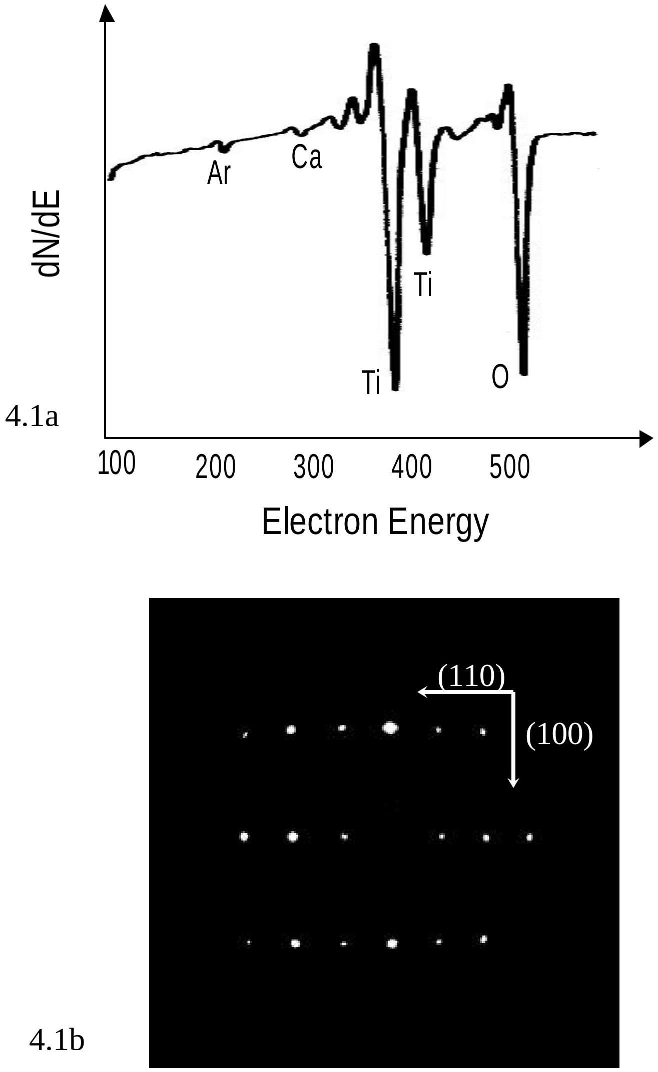

Figure 4.1: Macroscopic characterization of a $TiO_2(110)$ surface: (a) AES survey and (b) (1x1) LEED pattern. The surface has been cleaned by tens of sputtering-annealing cycles (see text). The only impurities are Ar and Ca. AES is taken using 1 KeV incident electrons, and LEED is taken using 88 eV electrons.

4.3 EXPERIMENTAL.

For different substrates, different ultrahigh chambers were used. For convenient, we call them hafnia chamber and titania chamber, respectively.

4.3.1 On HfO_2

Samples involving Ag and H_2O on hafnia were prepared in hafnia chamber and analyzed *in-situ* with a time-of-flight mass spectrometer (TOFMS, Comstock), that gathered data for all masses between 2 and 200 atomic mass units, and an Auger electron spectrometer (AES, Phi 15-255G) [4.29]. AES was taken at an electron energy of 3 keV and an emission current of 1.0 mA. Atomic force microscopy (AFM) images (Digital Instrument multimode AFM), were taken *ex-situ* under ambient conditions using a high aspect ratio silicon tip (radius of curvature ~ 10 nm.) In one set of experiments involving an additional UHV chamber, a measurement of the exposed Ag was obtained by titration with CH_3I TPD using a standard quadrupole mass spectrometer (Extrel). During titration, the sample was held at 150 K to avoid multilayer accumulation and to saturate the monolayer that subsequently desorbs molecularly at 210 K [4.30]. Because of relatively low sensitivity, this procedure was suitable only for Ag deposited directly on HfO_2.

A high quality 50 nm thick amorphous [4.31] HfO_2 thin film, prepared *ex-situ* on a 1 x 1 cm^2 Ni foil using a sputter-deposition method, was used as a substrate

[4.32]. This substrate was spot-welded onto a U-shaped tungsten loop that, in turn, was connected to electrically isolated copper rods in the UHV system. An alumel-chromel thermocouple was spot welded to the Ni foil and the whole assembly was mounted to a standard UHV XYZ-rotary motion manipulator. Liquid nitrogen cooling was supplied to the copper rods.

The HfO_2 surface was cleaned by cycles of 3 keV Ar^+ sputtering and vacuum annealing up to 1300 K. A small amount of carbon, < 5 atomic %, was not removable. It is attributed to the HfO_2 thin film deposition rather than a substrate transfer process.

Deionized H_2O, 18 MΩ/cm, was dosed through a standard leak valve at a chamber pressure of 1.0 x 10^{-7} Torr onto the HfO_2 surface held at 150 K. At this temperature, crystalline ice forms in competition with desorption [4.33, 4.34]. The water dose is presented in terms of effective Langmuir (L), 1 L = 1.0 x 10^{-6} Torr s. In these units, a dose of 18 L is ~ 1.2 nm thick based on the measured attenuation of the Hf AES signal at 185 eV. A (0001) bilayer of hexagonal ice is 0.36 nm thick. Comparing H_2O TPD peak areas measured for doses at 100 and 150 K, we calculate that the sticking coefficient of water on HfO_2 at 150 K is 0.56 of that at 100 K. Comparing the average ice thickness determined by AES with the amount of water adsorbed, measured by TPD, indicates that the ice forms a fairly rough surface.

Thus, while the ensemble average thickness is equivalent to ~ 3 bilayers of ice, account of roughness must be part of any model used to interpret data.

After preparation at 150 K, the crystalline ice matrix was cooled to 100 K and Ag was deposited from a thermal evaporation source held at 850 K. After Ag deposition, the H_2O was removed by ramping (2 K/s) the sample temperature to 315 K. The resulting Ag was characterized by measuring the attenuation of the Hf AES signal [4.35]. Under our experimental conditions, the rate of Ag deposition onto the ice was about 0.01 nm min^{-1}. Keeping in mind that the substrate was not a single crystal and that Ag does not increase in layer-by-layer fashion, we nevertheless present the Ag coverage in monolayer units (1 ML= 0.236 nm for Ag(111)) defined in terms of the attenuation of the Hf AES signal.

4.3.2 On TiO_2(110) and $(CH_3)_3COOH$ pre-saturated TiO_2(110)

The titania chamber (base pressure $8x10^{-11}$ Torr) has been described detailed previously [4.36]. It consists of a dual chamber ultrahigh vacuum system. The surface preparations by Ar^+ sputtering, annealing, and TMAAH functionization as well as surface analysis with AES and LEED are carried out in one chamber. The other chamber contains the scanning tunneling microscope and is also used to deposit thin ice layers and silver. Samples are mounted on molybdenum holders that can be transferred into the vacuum chamber through a load-lock using magnetically coupled linear motion and within the chamber using a XYZ-rotary manipulator and a wobble stick.

The $TiO_2(110)$ (MTI Corp., 10 x 2 x 0.5 mm) was polished both sides with off-angle less than 0.5 degree. The sample was bridged on two molybdenum springs. Between the samples and springs, there is a 0.05 mm thick tungsten foil that mechanically supports TiO_2 and decreases the sample temperature unevenness in the XY directions, and a 0.05 mm thick gold foil that contacts both tungsten and TiO_2 to decrease the temperature gradient in the Z direction. Above the sample, a 15 x 18 mm ceramic plate with a 6 x 8 mm rectangular hole was tightened down by screws to prevent vibrations. The sample can be heated to 1200 K by thermal radiation from a tantalum heater under the supporting tungsten foil. The sample temperature within the surface preparation chamber was measured by an optical fiber-couple pyrometer. The emissivity for polished Au of 0.02 was used while the sample was transparent, and 0.50 for oxidized Ti was used when the sample turned blue. The accuracy is estimated within ±20 K from previous experience. The sample temperature within STM chamber was measured by silicon diode, whose indicating temperature is about 5 degree lower than the actual sample temperature. Here, the temperature is presented without correction.

$TiO_2(110)$ was cleaned by cycles of 15 min 1 KeV Ar^+ sputtering (2 μA) at 400 K and 1 min annealing at 1050 K. The heating and cooling ramp rates are less than 2 K/s. After tens of such cycles, AES (Figure 4.1a) shows a sample surface free of carbon contamination, but involving small amount of calcium (~4% monolayer) and argon. The argon can be removed higher temperature annealing but not the calcium. Even with the presence of argon and calcium, a good (1x1) LEED pattern was observed (Figure 4.2b) using an electron energy of 88 eV.

Deionized H_2O, 18 MΩ/cm, was dosed through a standard leak valve at a chamber pressure of 6.0×10^{-8} Torr onto the TiO_2 surface held at 120 K, or TMAAH pre-saturated surface at 50 K. At these temperatures the thin ice layer is in the form of amorphous solid water (ASW) [4.34]. The water exposure is present in Langmuir (L), $1\ L=1\times10^{-6}$ Torr·s. Assuming that the water sticking coefficient is unity under these conditions, 1 L corresponds to roughly one monolayer. However, one must keep in mind that the ice film does not grow layer-by-layer necessarily, especially on a hydrophobic surface, i.e., on TMAAH-covered titania.

Ag was thermally evaporated from a homemade doser, and its deposition rate was measured by a crystal oscillator at the end of the doser. The rate was 0.1 nm/min on the crystal sensor, corresponding to ~24 pm/min, or ~0.1 ML/min, on the sample surface based on a calculation using the hardware geometry. For 1.2 ML Ag dosed on a clean surface, the Ag MNN transitions at 351 and 356 eV were observed in AES, confirming the deposition of Ag.

TMAAH (Aldrich 99%) was used without further purification. Right before dosing, it was frozen and pumped for 1 h to remove the volatile impurity by a turbo pump. Its purification was confirmed by residual gas analysis using a quadrupole mass spectrometer (UTI). TMAAH was dosed by backfilling via a standard leak valve. Since it is an electron- and photo- sensitive substance, UHV view ports were covered and the ion gauge and ion pump were shut off during experiments. Before dosing experiment began, the leak valve was calibrated to produce an initial pressure 5×10^{-8} Torr in test exposures. Exposures (pressure x time) are calculated assuming a constant dosing pressure equal to this initial pressure. The vapor pressure behind the leak valve was kept constant at the TMAAH saturation sublimation pressure by presenting solid TMAAH. Because no molecular adsorption happens at room temperature, 10 L TMAAH was exposed to $TiO_2(110)$ to prepare a fully pre-saturated surface of deprotonated trimethyl acetic acid.

STM experiments were performed using an Omicron variable temperature STM. Typical tunneling conditions are sample bias +2 V, tunneling current 0.2 nA, feedback 5% under the constant current mode. All images are taken at room temperature unless otherwise noted.

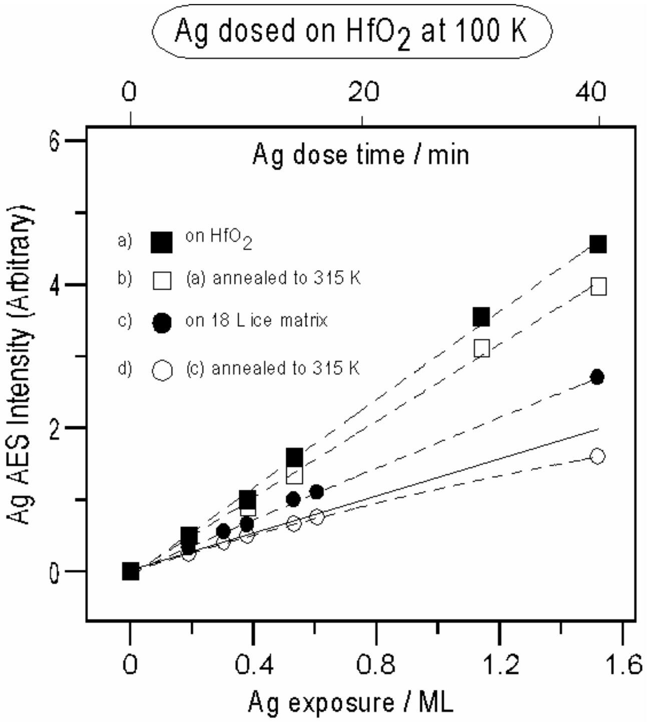

Figure 4.2: Ag AES (MNN) intensity variation with Ag dose (lower axis) or dose time (upper axis) for different processing conditions: (a) Ag deposited on clean HfO_2 at 100 K; (b) Ag deposited on clean HfO_2 at 100 K and annealed to 315 K; (c) Ag deposited on an 18 L (1.2 nm thick) crystalline ice layer at 100 K; and (d) Ag deposited on an 18 L (1.2 nm thick) crystalline ice layer at 100 K and annealed to 315 K. The dashed lines are fits to a quadratic equation (Table 4.1). The solid line is a straight line, drawn to emphasize the non-linearity of curve (d).

4.4 RESULTS

4.4.1 On HfO_2

4.4.1.1 Auger electron spectroscopy

The peak-to-peak Ag(MNN) AES intensities vary with Ag dose for different surface conditions (Figure 4.2). The Ag dose times range from 0 to 40 min corresponding to Ag coverages between 0 and 1.54 ML. Four major points emerge immediately: (1) For equal Ag doses, the AES signal is highest for dosing in the absence of $H_2O(s)$; (2) Annealing from 100 to 315 K lowers the Ag(MNN) intensity for Ag deposited with or without $H_2O(s)$; (3) After annealing to 315 K, comparing equal amounts of dosed Ag indicates that the structures formed in these two cases is very much different; and (4) Although the data set is somewhat sparse, there is no evidence for a distinct change of slope in (a) and (b) that would be expected were the growth mode layer-by-layer. There is curvature in (c) and (d) but it is not attributed to layer-by-layer growth. AFM data (see below) confirms the presence of particles for 1.5 ML Ag dose in both cases (b) and (d). CH_3I titration data (see below) confirms the absence of layer-by-layer growth above 0.8 ML for case (b).

Comparing curves (a) and (c), Ag deposited at 100 K on bare and ice-covered HfO_2, the signals in (c) are ~ 50% of those in (a). This reflects penetration of Ag into the ice layer. In another experiment (not shown), adding 18 L of $H_2O(s)$ after annealing attenuated the Ag(MNN) signal by 70%. From this we conclude that when hot Ag atoms interact with 18 L thick ice layer at 100 K, the average penetration is significantly less than the ice layer thickness, i.e., most of the as-deposited Ag exists within the ice matrix.

The signal decrease upon annealing, i.e., curves (b) and (d), is attributed to Ag agglomeration. The effect is much larger for Ag dosed into ice. The signal drops even though water is removed in passing from curve (c) to (d), a process that, in the absence of agglomeration, would increase the AES Ag signal. It is striking that the fractional signal change brought about by removal of H_2O is large and only weakly dependent on coverage over the range explored (the value in (d) is 0.6 of that in (c)). On the other hand, for deposition directly on HfO_2, annealing reduces the Ag AES signal to 0.8 of its as-deposited value, independent of Ag dose.

The decrease accompanying removing H_2O is not due to induced desorption of Ag during removal of water (Figure 4.3). This possibility is ruled out because there are no detectable mass 107 and 109 signals (sensitivity < 0.05 ML) between 100 and 315 K in TPD. Rather, Ag desorbs, as expected, above 800 K and the only other species desorbing between 2 and 200 amu is H_2O desorbing between 170 and 190 K (Figure 4.3). Furthermore the AES signals in figure 1(d) do not depend on the TPD ramp rate—between 1 and 10 K/s—used to remove H_2O (not shown).

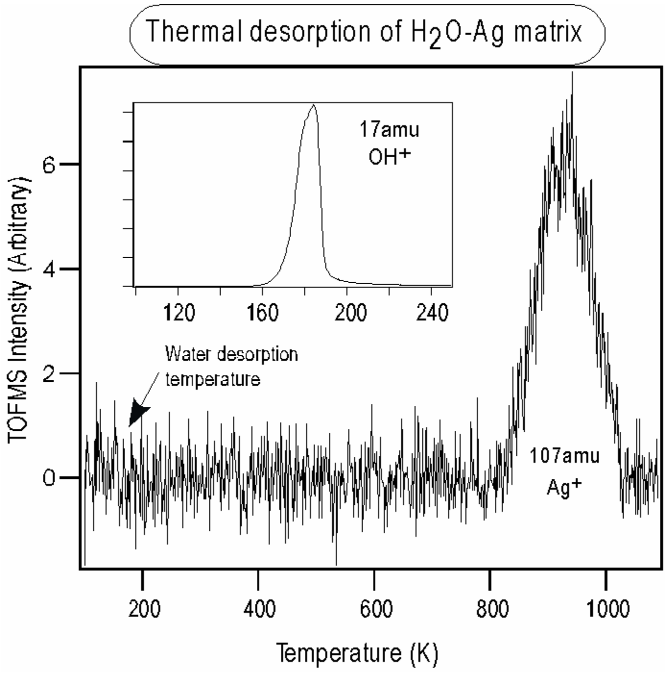

Figure 4.3: TPD (2.0 K s^{-1}) after dosing 1.5 ML Ag onto an 18 L ice layer at 100 K. There is no evidence for Ag desorption accompanying H_2O desorption. Arrow on lower curve marks the temperature of the water desorption peak (inset).

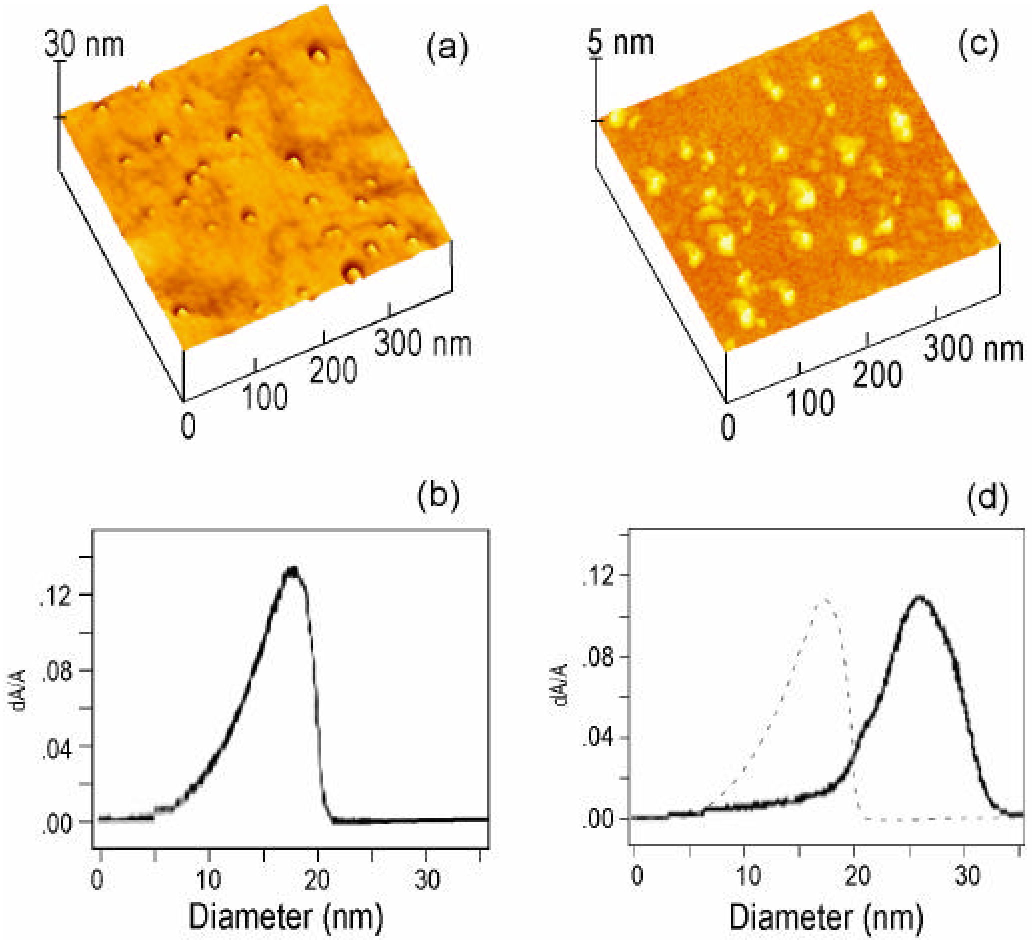

Figure 4.4: AFM results for thermally annealed Ag on HfO_2 samples. (a) and (b) – AFM image and particle diameter distribution for Ag deposited onto ice at 100 K and annealed to 315 K. (c) and (d) – AFM image and particle diameter distribution for Ag deposited onto bare HfO_2 at 100 K and annealed to 315 K. The dotted curve in (d) is reproduced from (b) and underscores the strong shift toward smaller particles. Notice the large difference in the z-scales of images (a) and (c).

4.4.1.2 Atomic force microscopy

To assess the surface topology, AFM images of annealed samples were acquired (Figure 4.4). Transmission electron microscopy elemental analysis confirms that the particles are silver and grow along [111] direction preferentially (not shown). For both images, layer-by-layer growth of Ag is clearly ruled out. Compared to deposition directly on HfO_2, Figure 4.4c, deposition onto crystalline H_2O, Figure 4.4a, leads to strikingly different Ag particles.

When ice is involved, the particles have a circular cross section and, with no adjustment for the AFM tip contribution, the diameter distribution ranges from ~ 5 to 20 nanometers (particles with diameters smaller than 5 nm were not resolvable) distributed as indicated in Figure 4.4b. The diameter distribution is asymmetric; it increases slowly from 5 nm, peaks at 18 nm, and then falls steeply to zero at 22 nm. This image is representative—images taken from 7 locations on the sample are all like those of Fig. 3a; nanoparticles are rarely clumped together, their number density is very low ($\sim 2\times10^{10}$ cm^{-2}), and relatively large distances separate them. Only 4% of the surface area is covered by particles. AFM line analysis of 40 particles shows the average height-to-diameter ratio is 0.32 ± 0.06. Thus, a representative particle formed by depositing 1.5 ML of Ag onto an ice layer at 100 K, desorbing the water by raising the temperature with a 2 K s^{-1} ramp to 315 K and annealing for 2 min. has dimensions 18 × 6 nm.

In the absence of ice, Figures 4.4c and 4.4d, when the same conditions are established, the particles are more broadly distributed, more irregularly shaped, cover much more of the surface (32 %) and have a significantly larger average diameter (25 nm). AFM line analysis of 40 particles gives an average height-to-diameter ratio of 0.066 ± 0.014, i.e., the height is only 1.6 nm for a 25 nm diameter particle. The ensemble average particle dimensions are 26 × 1.7 nm and, compared to Figure 4.4d, diameter distribution is more symmetric.

A rough approximation for the total coverage can be obtained from the AFM data and compared with the AES results. Based on the average dimensions extracted from Figure 4.4, and assuming the particles are shaped as a section from a sphere, the calculated number of Ag atoms in Figure 4.4a corresponds to 2.1 ML while that in Figure 4.4b corresponds to 1.3 ML. According to AES, 1.5 ML of Ag was deposited in each case. That the AFM data for Ag deposited on bare HfO_2 is slightly less than indicated by AES can be accounted for in terms of Ag not resolved in the AFM images. The large positive deviation of the sample with water may be caused by either the AFM tip distortion [4.37] or the oxidation of Ag in ambient [4.38].

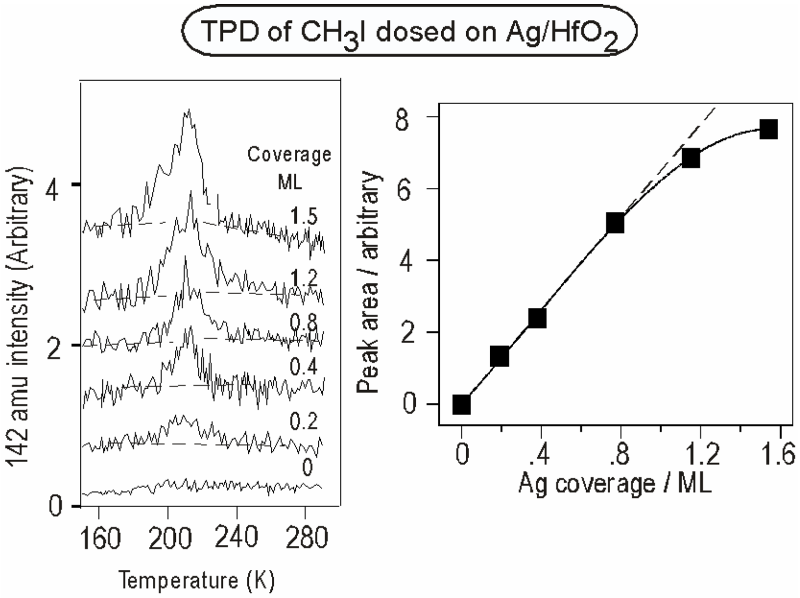

Figure 4.5: TPD (142 amu. 3 K s^{-1}) of CH_3I dosed onto Ag-covered HfO_2 at 150 K (to avoid multilayer formation). Plot with solid squares is the 142 amu peak area versus Ag coverage. These results involve samples dosed with Ag in the absence of ice.

Table 4.1: Fit parameters: AES signal versus Ag dose in Figure 4.1.

Sample	c_0	c_1	c_2	R^2
A: No ice, no anneal	-.016	29.7	0.192	.9993
B: No ice, anneal to 310 K	-.014	28.2	-.043	.9990
C: Ice, no anneal	-.002	18.9	-.768	.9996
D: Ice, anneal to 310 K	-.000	13.6	-2.00	.99989

Close examination of Figure 4.2 shows non-linear behavior, particularly for case (d). Fitting each of the four curves to a quadratic function, $I = c_0 + c_1\theta_{Ag} + c_2\theta_{Ag}^2$, where θ_{Ag} is the coverage of Ag, leads to the coefficients listed in Table 4.1. The noteworthy points are: first, the linear coefficient of curve (a) is 1.6 that of curve (c); second, the non-linear coefficients (c_2) are, in absolute terms, much smaller for curves (a) and (b) than for curves (c) and (d), an observation taken as indicating that the Ag is distributed more uniformly when directly deposited on HfO_2, curves (a) and (b). The non-linear coefficient for curve (c) is negative. It would be close to zero were the Ag atoms distributed uniformly and randomly in the ice matrix. Possible reasons for the negative value taken by c_2 in curve (c) include: (1) Ag atoms deposited late in the procedure penetrate deeper into the ice matrix than those deposited at early times, and (2) Ag atoms deposited late have a greater propensity to attach to atoms arriving earlier, i.e., small cluster development. The even larger negative c_2 found after removal of H_2O is attributed to extensive 3D cluster growth consistent with the AFM results.

4.4.1.3 CH_3I titration

To estimate relative areas of exposed Ag, CH_3I was dosed to saturation at 150 K and TPD was measured using a standard quadrupole mass spectrometer (Extrel). For Ag dosed on HfO_2 (no ice), the 210 K CH_3I (142 amu) peak area (Figure 4.5) was used to estimate the relative amount of exposed Ag [4.30]. The area as a function of Ag coverage grows linearly up to 0.8 ML, but less rapidly for higher Ag doses. This is consistent with the AFM results that, for 1.5 ML present clear evidence for particles (Figure 4.5). In analogous experiments with Ag particles prepared by deposition into ice, the 210 K peak was buried in the noise of the 142 amu plot. This is consistent with the relatively small number of particles detected in AFM (Figure 4.4) and the relatively weak AES signal (Figure 4.2).

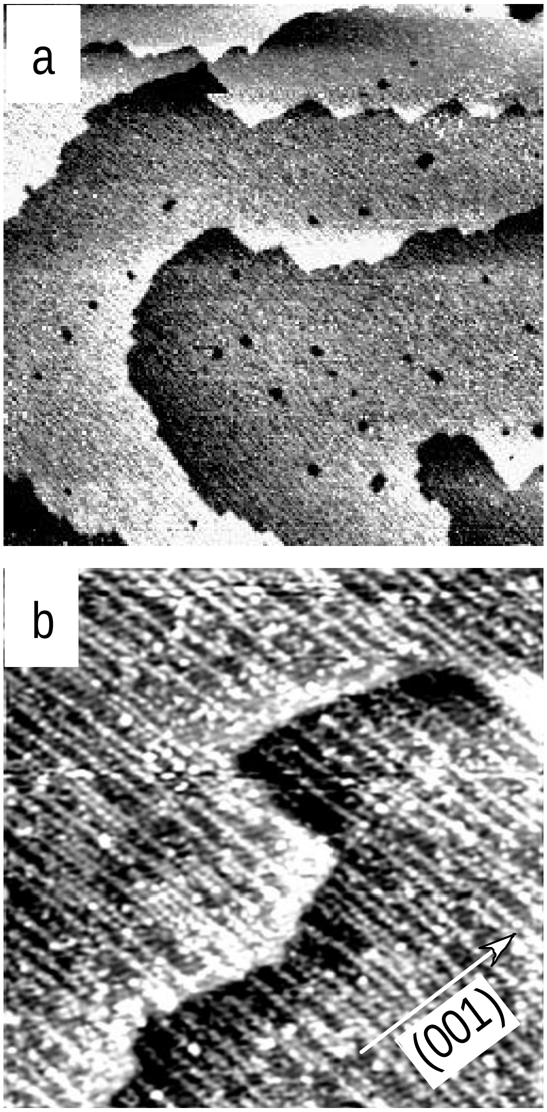

Figure 4.6: STM images of clean TiO2(110) (V_s=+1.99 V, I_t=0.20 nA). (a) 250 x 250 nm^2, (b) 50 x 50 nm^2.

4.4.2 On $TiO_2(110)$

The sputtered, annealed $TiO_2(110)$ surfaces consist of terraces 50-100 nm wide (Figure 4.6a), on which there are bright atomic rows separated by 1.3 nm, a characteristic of (1x2) surface reconstruction. Higher resolution STM images (Figure 4.6 b) show that the surface is not completely reconstructed. The bright rows are normally suggested to correspond to tunneling into the unoccupied Ti 3d state under positive sample bias condition [4.39, 4.17]. The separation between two closest bright rows is 1.3 nm, but a number of gaps in this row structure are also observed. Looking at the image more closely, there is another kind of row in addition to the brightest rows. The rows in the under layer have an exactly 0.65 nm separation, and are the initial (1x1) surface structure as observed by LEED (Figure 4.1b). Since the top bright rows run along the perpendicular direction of initial (001) direction, it is called cross-linked (1x2) reconstruction, which is generally formed by high concentration of Ti^{3+}, i.e., high level of TiO_2 reduction [4.40]. Indeed, the samples are dark blue after tens of vacuum annealing at 1050 K.

To serve as a benchmark experiment and for comparison with published results, 0.2 ML Ag was deposited onto a clean $TiO_2(110)$ surface (Figure 4.7a) at 120 K. Small particles with narrow size distribution spread over the whole surface randomly. Their average diameter is 5-6 nm and height is 0.7-0.8 nm. Our results are consistent with others [4.25, 4.26].

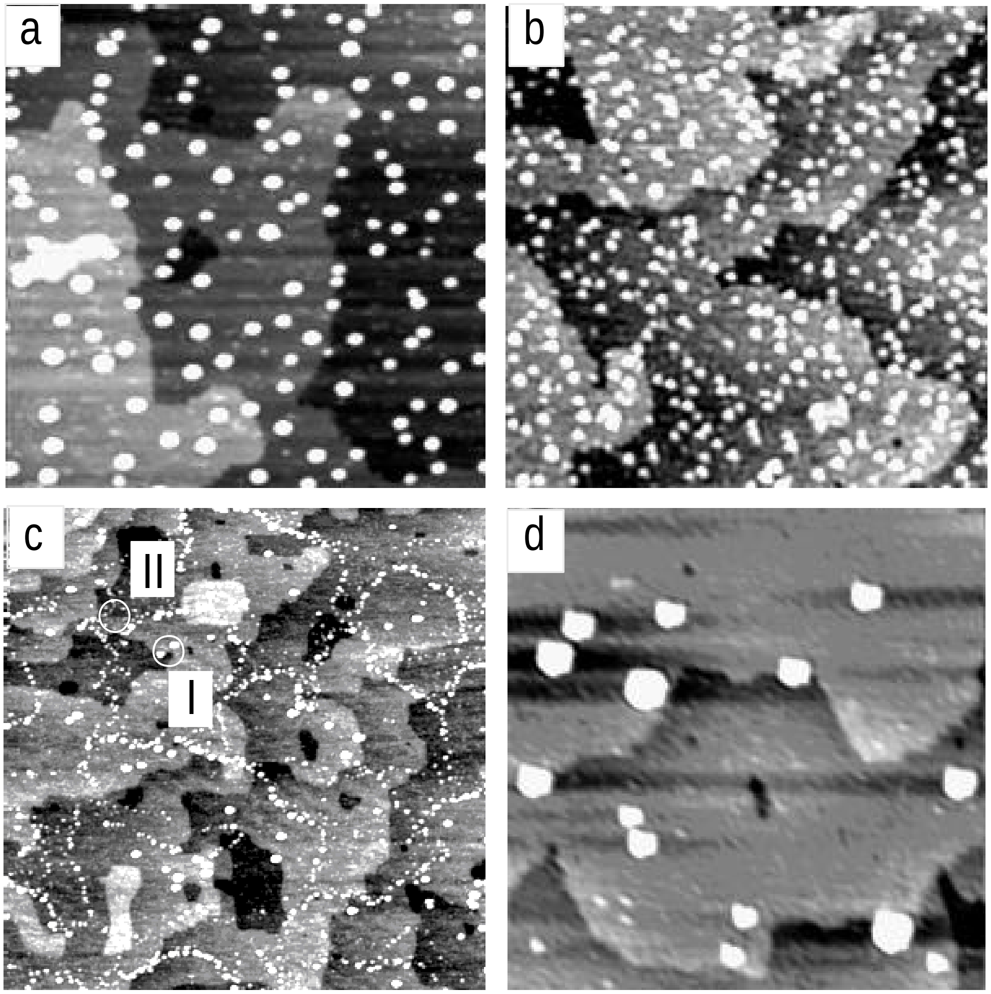

Figure 4.7: STM images of 0.2 ML Ag deposited onto different amount of solid water on TiO_2(110). (a) 0 L, 100 x 100 nm^2; (b) 4 L, 100 x 100 nm^2; (c) 18 L, 300 x 300 nm^2; (d) 60 L, 100 x 100 nm^2. Clearly, 1 D strings is formed only within a narrow window of water thickness. Ag is dosed at 120 K on the water pre-dosed surfaces. Water is removed by heating (~10 K/s). Images are taken under constant current mode at room temperature.

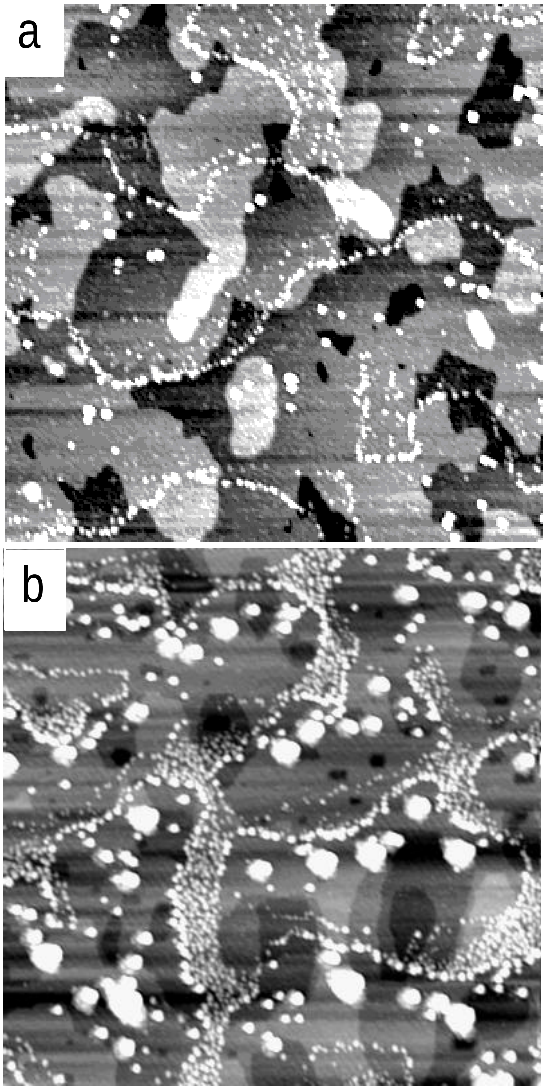

Figure 4.8: STM images of various amount of Ag onto a 18 L solid water layer on $TiO_2(110)$. (a) 0.1 ML Ag, 300 x 300 nm^2; (b) 1.2 ML, 300 x 300 nm^2. Both Ag and water are dosed at 120 K. Water is removed by ~ 10 K /s ramp. Images are taken under constant current mode at room temperature. Clearly, the 1 D stings always form from 0.1 to 1.2 ML Ag coverage.

With the same amount of Ag deposited onto a very thin ice layer (4L) at 120 K, the resulting nano particles still have a random spatial distribution, but their average size drops to 4-5 nm and number density increases to $2.5 \times 10^{12}/cm^2$ (Figure 4.7b), compared to $1.2 \times 10^{12}/cm^2$ without present of water. With the increasing of ice layer thickness, the significant changes happen. There are three different types of nano particles formed in terms of size and distribution when an 18 L ice layer is used (Figure 4.7c). Type I particles have average size 7 x 1 nm (diameter x height) and low number density. They are generally located on the concave sides of bead-like strings. These strings are composed of uniform size particles (5 x 0.5 nm), and run randomly. These strings have an average curvature 30-40 nm. On the convex sides of these strings, especially close to where two strings intersect, there is another type of particles (Type II). They are relatively small (2-3 x 0.3 nm) and crowd together. The stings disappears with further increase of ice layer thickness (Figure 4.7d), and resulting particles have broad size distribution from 2 to 10 nm and spread randomly on the surface. Apparently, adding a thin ice layer surely changes the growth of Ag on $TiO_2(110)$, and there is only a narrow window of ice layer thickness for the formation of one dimensional strings.

To investigate the Ag concentration on the string formation, different amounts of Ag were exposed on 18 L ice layers (Figure 4.8). Within the tested region—0.1 ML to 1.2 ML, nanoparticle strings always appear. Within the strings, the size of particles and the distance between the particles, as well as their total length in unit area, are small, vary weakly with different Ag coverage. However, both the number densities and the sizes of both Type I and Type II (refer to Figure 4.7c) increase significantly with increasing coverage. The results are summarized in Table 4.2.

Table 4.2: Variation of the resulting particle features with Ag dose onto 18 L ice on $TiO_2(110)$

?$_{Ag}$ (ML)	Particle Size (D x H in nm)		Particle in Strings (nm)		Specific Length of Stings (μm/μm^2)
	Type I	Type II	Size (DxH)	Distance	
0.1	(6.5±1.0)x(0.7±0.2)	(2.6±0.4)x(0.240±0.04)	(4.4±0.7)x(0.47±0.08)	5.0±1.0	14.7±2.6
0.2	(6.6±1.0)x(1.0±0.2)	(2.9±0.3)x(0.237±0.04)	(4.6±0.8)x(0.50±0.16)	4.9±0.9	16.0±3.3
1.2	(14.7±4.4)x(2.6±0.5)	(3.5±0.4)x(0.54±0.13)	(5.2±1.1)x(0.84±0.23)	5.3±1.6	15.9±2.0

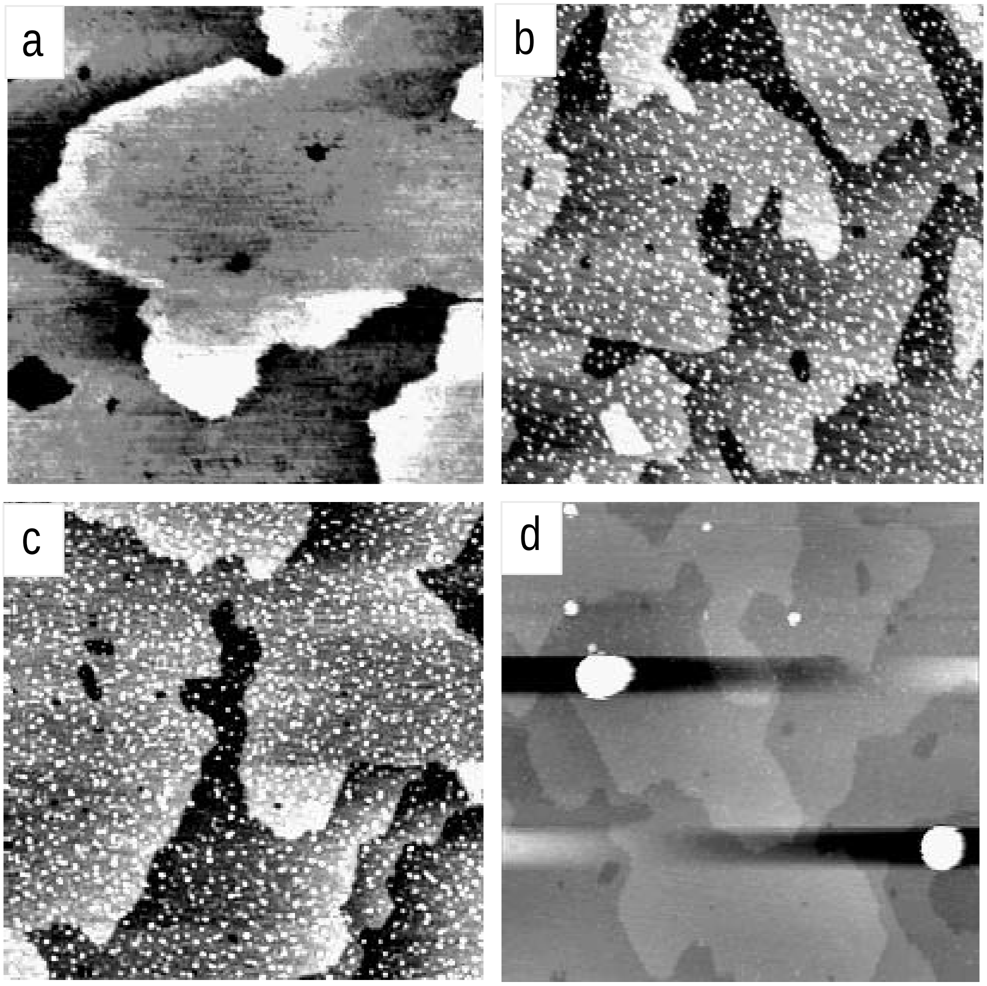

Figure 4.9: STM images of Ag deposition onto trimethyl acetic acetate ($TMAA^-$) saturated $TiO_2(110)$. All images are taken under constant current mode at room temperature. Both Ag and water are dosed at 50 K. (a) $TMAA^-$ saturated $TiO_2(110)$, 100 x 100 nm^2; (b) 0.2 ML Ag onto $TMAA^-$ saturated $TiO_2(110)$, 100 x 100 nm^2; (c) and (d) 0.2 ML Ag onto 18 L solid water on $TMAA^-$ saturated $TiO_2(110)$, 200 x 200 nm^2. (c) and (d) are taken at different spots located within 2 x 2 μm^2 (see Figure 4.10d). The similarity between (c) and (b) makes us believe that 18 L water is not enough to cover the all surface (see text).

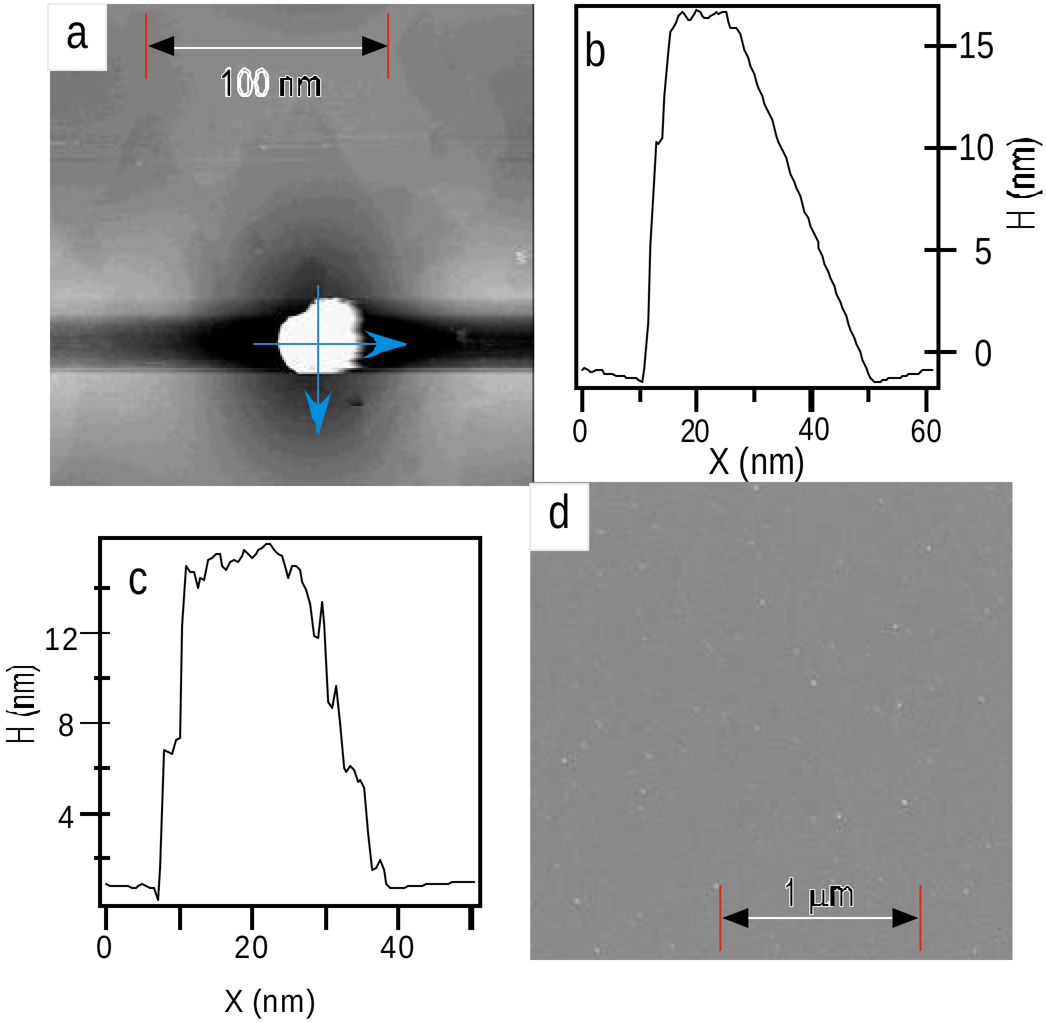

Figure 4.10: STM and SEM images and line profile of 0.2 ML Ag onto 18 L water on TMAA-saturated $TiO_2(110)$. (a) STM image of a huge Ag particle, whose height and radius have close dimension. (b) and (c) the STM line profile of the Ag particle in (a), and the lines are marked by light blue arrows. The tail in (b) is because the delayed response of STM to high objects. (d) SEM image of a large scope (2.5 x 2.5 µm). The bright dots are the huge particles in (d), within them there are smaller particles not resolved (see Fig. 4.9c). SEM is taken using 3 KeV electrons. Energy dispersive spectrum verifies the sparse bright dots are silver particles.

4.4.3 On TMAA$^-$ saturated TiO_2(110)

When TMAAH adsorbs on TiO_2(110) surface, its O-H bond breaks and surface trimethyl acetic acetate (TMAA$^-$), $-_{(a)}OC(C(CH_3)_3)O_{(a)}-$, forms with the tert-butyl group oriented away from the surface perpendicularly [4.22]. The TMAA$^-$ saturated surface is atomically flat (Figure 4.9a), and is extremely hydrophobic. When a 0.2 ML Ag is deposited on such a surface at 50 K (Figure 4.9b), small particles with narrow distribution spread randomly on the surface. Their average size is 3.5 x 0.44 nm, which is smaller than the same amount of Ag on clean TiO_2(110) at 120 K—5-6 x 0.7-0.8 nm (Figure 4.7a). The difference is likely caused by different substrate temperatures. When diffusion is controlling, tt has been shown that the cube of the number density of resulting particle (N) is proportional to the reciprocal of surface diffusion coefficient (D), i.e., $N^3 \propto 1/D$ [4.41]. Lowering substrate temperature lowers surface diffusion and smaller and denser particles result.

Deposition of 0.2 ML Ag onto a 18 L ice layer on TiO_2(110) gives two remarkably different images (Figure 4.9 c and d) that are taken at different locations with separation less than 2 μm. One location is very similar to that on TMAA$^-$ saturated TiO_2(110) without water, but the other is totally different. Particles with high dispersion of size distribution and very low number density form on the surface randomly. The largest particles have diameter larger than 30 nm while the smallest ones are only ~5 nm. We believe that the difference is caused by the very uneven distribution of ice layer on the TMAA$^-$ saturated TiO_2(110). Line profiles (Figure 4.10 b and c) show that the heights of some of these largest particles are similar to their radii and the particles grown three dimensionally. A large dimension scanning electron microscopy image (Figure 4.10d) shows that these large particles are distributed on the surface randomly with average separation several hundred nanometers.

To summarize the experimental results, significant differences of Ag nanoparticle growth are observed on different surfaces and on the same surface with presence or absence of water layers. On clean HfO_2, large diameter but low height particles with irregular shapes form at 100 K. With the presence of water layer, smaller diameter but higher height particles with a lens shape form on HfO_2. In many cases, the particles have a height larger than the initial water layer thickness. Our results got Ag deposition on clean TiO_2(110) are consistent with literature data, i.e., a narrow size distribution of particles randomly spread on the surface at 120 K. Differents amount of water lead to the very different Ag particles. With a very thin water layer (~ 4L), particles still randomly spread on the surface, but they are smaller and denser, their shapes are more irregular, and their size distribution are slightly wider than that on clean TiO_2(110). With a 18 L water layer, particles forms one dimensional strings that ran randomly on the surface. Separated by the stings, small numbers of large particles (Type I) and small and crowed particles (Type II) coexist in different domains. The sizes and number densities of the Type I and II particles increase with increasing Ag coverage, but within the sting particle sizes change very little and total length of these stings in a unit area does not change detectably. With a relative thick water layer (~60 L), strings are no longer present, the particle sizes vary from 2 to 10 nm with 0.2 ML macroscopic coverage of Ag, and the number density of these particles is low (~2 x 10^{11} cm^{-2}). On $TMAA^-$ saturated $TiO_2(110)$ without water at 50 K, particles are smaller and denser than that on clean $TiO_2(110)$ at 120 K. Two remarkably different types of regions exist when 18 L ice is used on $TMAA^-$ saturated $TiO_2(110)$. One has Ag particles with very similar features as on $TMAA^-$ saturated $TiO_2(110)$, and the other has few but huge nanoparticles (>30 nm) with very good three dimensional features ($H:R \approx 1:1$). It is believed that the former region is not covered by water.

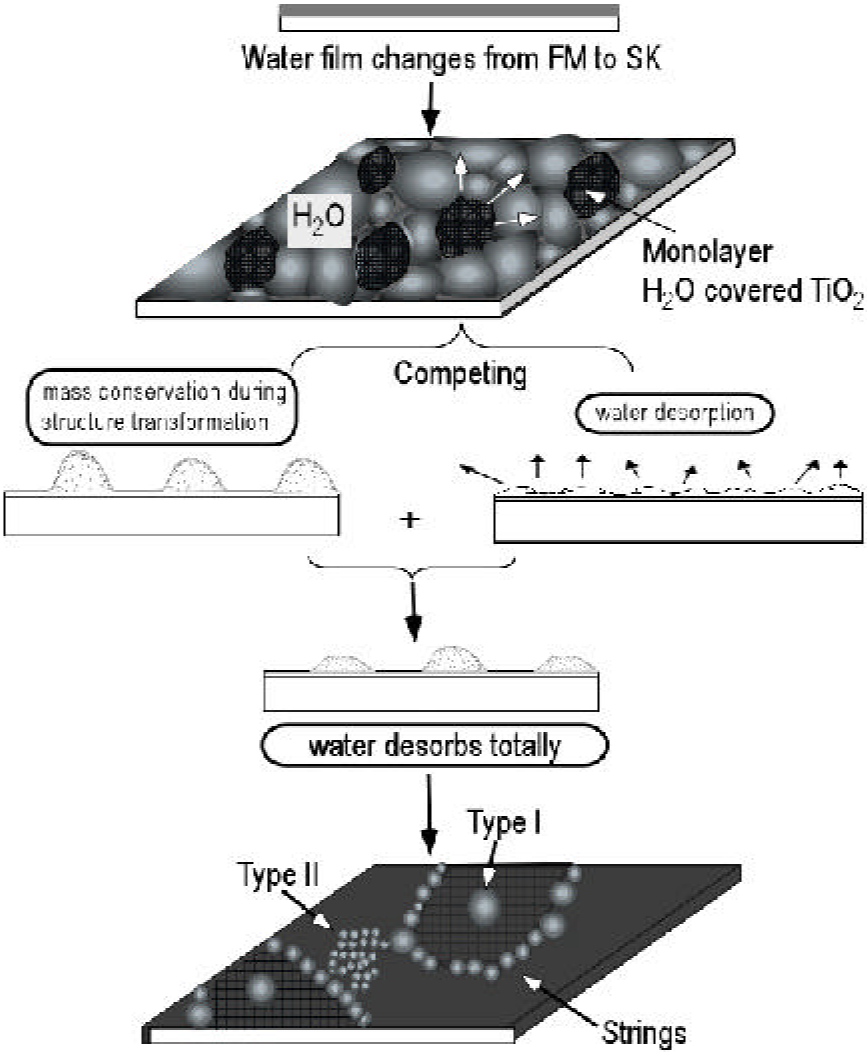

Figure 4.11: Proposed growth model of Ag deposition onto solid water layer on $TiO_2(110)$. At low temperature, solid water grows layer-by-layer (FM). When temperature rises, water morphology transform from FM to SK. Conservation of water mass forces higher water droplet formation at some spots. How good the conservation is depends on at what temperature the transformation occurs. When water relocates laterally and vertically, tiny Ag_n clusters formed upon deposition retain within water and travel with it so that they are traceable to the water redistribution. The stings track the periphery of water receding. Ag_n cluster agglomeration happens during both water relocation and desorption, but the portion depends on the Ag_n cluster concentration and water desorption rate (see text).

4.5 DISCUSSION

4.5.1 Deposition onto bare HfO_2 at 100 K

Since there are no published results of Ag deposition on clean HfO_2, it deserves more detailed discussion of the growth mode. Our results for deposition of Ag from thermal evaporation source at 850 K onto a thin amorphous HfO_2 film are consistent with a structure governed by a random spatial distribution of Ag atom arrival trajectories coupled with a short-lived thermalization trajectory that traps Ag atoms in a metastable configuration. This structure is closely approximated using a hit-and-stick model that ignores the thermalization portion of the Ag atom trajectory. Annealing to 315 K leads to irreversible restructuring that removes the metastable characteristics. This model is consistent with the AES and AFM data of Figures 4.2 and 4.4. Deposition at 100 K is consistent with a statistical hit-and-stick model, not a layer-by-layer (Frank-van der Merwe) or layer-plus-cluster (Stranski-Krastanov) model. And annealing at 315 K, leads to restructuring involving thermally activated 3D growth resulting in attenuation of the Ag AES signal and formation of thin Ag disc-like particles with broadly distributed diameters. A similar model is reported for Cu on $HfSiO_4$ [4.42]; when an amount of Cu more than sufficient to complete a single layer is deposited at 300 K, 15% of the oxide surface remains uncovered according to low energy He^+ ion scattering spectra. The metastability of this

$Cu/HfSiO_4$ structure is revealed during annealing; the Cu irreversibly restructures by 3D particle growth and significant de-wetting to expose more oxide.

4.5.2 General features of Ag deposition onto ice layers

Silver deposition onto thin ice layers clearly leads to different results (see the end of Section 4.4). We suppose that ice plays important roles by: (1) thermalizing the incident Ag and, at low temperatures (50-120K), keeping most, if not all, Ag from reaching the oxide substrate; (2) facilitating the formation of small clusters, Ag_n, that have a lateral distribution that is uniform across the ice and are more concentrated near the ice-vacuum than at the ice-substrate interface; and, most important, (3) controlling the agglomeration of these small clusters and the areal distribution of the resulting nanoparticles during lateral and vertical movement of the H_2O.

4.5.2.1 Morphology of solid water covered HfO_2, $TiO_2(110)$ and TMAA- saturated $TiO_2(110)$

Due to the difference of their hydrophilicites, ice layers are proposed to follow different growth modes on HfO_2, $TiO_2(110)$ and $TMAA^-$ saturated $TiO_2(110)$. HfO_2 is hydrophilic, and has a 74° contact angle of water under ambient[4.43]. Water TPD on HfO_2 (Figure 4.3) shows no distinguishable monolayer peak but onsets much higher temperature (150 K) than bulk water desorption (130 K). On gold, water has similar TPD feature [4.44] and a contact angle 40^o [4.45]. The morphology of the 10 nm thick ice films on a gold surface is dune-like, whose lateral and vertical corrugations are 60-90 nm and ~ 1 nm, respectively [4.46]. Thus, we suppose that solid water follows a Stranski-Krastinov model (SK, a few islands on top of layers). The wettability of water on TiO_2 surface has been studied intensively because of its potential use as amphiphilic (both water and oil wettable) materials. Under ambient water contact angle on $TiO_2(110)$ is $\sim 72^o$, and UV-radiation turns the surface to super-amphiphilic—contact angles of both water and oil are close to zero degree) [4.47]. This change has been attributed to the creation of surface vacancies that dissociate water and form microscopic hydrophilic domains [4.48]. More recently, a very detailed TPD study [4.22] shows that water even wets a oxygen-vacancy-free $TiO_2(110)$ surface under UHV. In water TPD on $TiO_2(110)$ with vacancy population 9%, both monolayer (265 K) and second layer (175 K) water desorption is distinguishable [4.49]. Our samples have a dark blue color, and are expected to contain some oxygen vacancies on their surfaces. Since Water TPDs are very similar on both $TiO_2(110)$ and MgO(100) [4.50] and an ice surface close to atomic flat is observed on MgO(100) [4.51] using AFM, we propose that solid water follows Frank-van der Merwe mode (FM, layer by layer). Whether it is SK or FM growth mode, the unevenness of Ag distribution in XY directions is negligible.

The projecting size of trimethyl acetic acid matches with the lattice constant of $TiO_2(110)$ well so that $TMAA^-$ can cover the whole surface densely packed if given enough exposure [4.22]. Thus a very hydrophobic even superhydrophobic surface may form. For example, the contact angle of water is ~ 160^o on an ultra-thin stearic acid ($CH_3(CH_2)_{16}COOH$) film adsorbed chemically onto a polyethylene coated aluminum wafer [4.52]. The effects of hydrophobic substances on water behaviors have attracted much attention since last two decades [4.53] for its *in vivo* importance. However, the water diffusion coefficients (D_{water}) on hydrophobic surfaces have been experimentally measured little, probably due to the high water diffusivity on such surfaces. Molecular dynamics (MD) simulation gives a lateral coefficient of ~4.4×10^{-5} cm^2/s on a flat hydrophobic surface at room temperature [4.54, 4.55]. Using the MD simulation results from 200 K to 350 K, extrapolating to 55 K gives $D_{water} \approx 5x10^{-9}$ cm^2/s. Water molecules are mobile enough reach to a thermodynamically stable state on the surface at 55 K within the time of 10^3 sec. Due to the strong repulsion force between tert-butyl group and water and attraction between water molecules themselves, it is plausible to propose water follows Volmer-Weber mode (VW, 3 D islands). To support our suspect, water desorption onsets at 130 K on $TMAA^-$ saturated $TiO_2(110)$, where the bulk water desorbs [4.22].

4.5.2.2 Small cluster formation within solid water films

Based on matrix isolation experiments, we suppose that Ag deposition onto ice at 100 K forms atoms and tiny clusters within the ice matrix. Huber et al. [4.15] report that 10^2 to 10^4 ppm Ag deposited simultaneously with H_2O at 10 K in an amorphous ice matrix exists as Ag_2-Ag_4 up to 125 K. In our case, the Ag/H_2O ratio is higher (On HfO_2, on the average for 1.5 ML Ag into 5 bilayers of water, the Ag/H_2O ratio would be of order 0.15; on TiO_2, on the average for 0.2 ML Ag into 18 L of water, the Ag/H2O ration would be of order of 0.01 versus a maximum of 0.01 in the previous work) so the cluster size distribution may be larger as the result of adding monomers, i.e., $Ag_n + Ag \to Ag_{n+1}$. Combination of clusters, $Ag_n + Ag_m \to Ag_{n+m}$, is less likely in view of the known stability of clusters to 125 K [4.15]. The very large particles (Figure 4.4a and 4.10a), formed as H_2O is removed, are then ascribed mainly to multiple small cluster agglomerations, Ag_n + Ag_m + ... + Ag_p $\to$ $Ag_{m+n+...+p}$.

4.5.2.3 Agglomeration of small clusters while water desorption and relocation

The unique features of resulting particles—the height of the Ag nanoparticles exceeds the average thickness of the water layer in many cases on HfO_2 and 1 D strings forms by Ag deposition onto 18 L water covered TiO_2(110), infer that the small Ag_n clusters must move a lot in both vertical and lateral directions. A following phenomenological growth model (Figure 4.11) is first used to interpret Ag deposition onto 18L ice layer on TiO_2(110), and then generalized to all cases. As the temperature rises and before significant desorption of H_2O, the flat solid water melts and relocated to form separate droplets on a monolayer/bilayer water covered $TiO_2(110)$ surface, very like SK mode. We assume that as the strongly H-bonded H_2O molecules move to form droplets, the small Ag_n clusters are swept along. As a result there are strong lateral variations of the Ag concentration across the substrate. When water recedes, Ag_n clusters travel with water molecules by both the attraction and the momentum transfer between water and silver. When Ag_n clusters move, they have chance to collide each other. Once they collide, they will agglomerate and release energy because of the high surface energy of silver. This process continues until the particle is large enough not to drag by water anymore. Thus large particles—Type I, form. During the dewetting process, water molecules have larger velocity than Ag_n clusters so that Ag_n clusters have higher concentration at the edge of water films, where agglomeration becomes easier to happen. Thus the strings, which track the rim of water receding, form. Most small Ag clusters remain trapped within water, which stays within string surrounding areas. Water desorbs further as the temperature continues to rise, bringing small Ag_n clusters in contact with each other thereby facilitating the growth of uniform small particles as observed (Type II). Because the nucleation process depends on the water desorption, it happens at almost the same moment so that Type I particles have the smallest size dispersion. Increasing Ag coverage increases the Ag_n clusters concentration so that the number density and size of both Type I and Type II particles increase. However, it does not change the total length of strings because the sting formation is controlled by the water dewetting, and the density and size of string composing particles change a little since they are controlled by both Ag_n cluster concentration and water dewetting.

When the ice layer is very thin, three effects appear: (1) Ag_n clusters are easy to reach to the substrate and the water molecules within monolayer/bilayer are immobile, forbidding the long region lateral movement; (2) their concentration is relatively high so that the agglomeration happens much earlier and water desorption competition makes not enough water left to relocate these Ag_n clusters; and (3), most important, the surface tension within the water layer, which the driving force for the morphology change from FM to SK, is eliminated as the water film is really thin. So, without the severe relocation of water, the Ag_n clusters agglomerate locally to form uniform and small particles. Compared to thermally Ag atoms on clean TiO_2(110), Ag_n clusters have larger mass and less kinetic energy so that they have less mobility as thermal emitted Ag single atoms, resulting smaller and denser particles. A potential application of deposition onto a very thin ice layer is to synthesize smaller and high number density particles, which is normally desired in heterogeneous catalysis. A relative thick ice layer (~10 nm for 60 L water) (1) prevents the Ag_n clusters to reach to the substrate until the final particles formed, at that moment most of water desorbs; and (2) takes longer time to desorb all the water.

So, Ag_n clusters travel longer time and horizontal distance, and the agglomeration is determined by the collision of Ag_n clusters mostly, resulting a log-normal size distribution of particles with low number density [4.56].

This model requires the massive mass transportation of water that is easily realized by liquid. Solid H_2O liquefaction at low temperature has some precedence in the literature. Surface melting has been reported for thin amorphous ice films [4.57, 4.58] and bilayer ice adsorbed on Pt(111) [4.59, 4.60]. TEM shows that liquid water and cubic ice co-exist from 140 to 210 K under vacuum. While most experiments put the temperature at which a liquid-like layer exists at about 243 K [4.61], molecular dynamics simulations show that the melting may occur between 150 K [4.62] and 190 K [4.63] for crystalline ice. A similar argument has been made to describe the formation of ice nanoclusters on $CeO_2(001)$ [4.64].

Similar to $TiO_2(110)$, Ag_n cluster agglomeration powered by water mass relocation is proposed to occur on HfO_2. Initial water layer has a SK structure, and it is proposed to become VW as temperature rises. The driving force is not only the surface tension within the thin ice layer but also the stronger attraction among water molecules than water-HfO_2. Although hafnium and titanium are the same column in periodic table, the hydrophilicity of their oxides is presumably very different because (1) HfO_2 does not have any oxygen vacancy to serve as water dissociation center due to its good thermal stability, and (2) our HfO_2 surface is O-terminated without five-coordinated Hf^{4+} to attract hydroxyl oxygen. Additionally, the small amount of carbon impurity in the HfO_2 may become hydrophobic centers to initiate water SK to VW transformation. The H_2O volume must be nearly conserved since the volume of the liquid droplets will be only slightly lower than the solid from which they form without water desorption. Thus, the average height of the H_2O droplets must be larger than the average thickness of the original ice layer. If the transformation occurs at low temperature, desorption is overwhelmed, most of water is conserved and large water droplets form to bring small Ag clusters in contact with each other thereby facilitating the growth of large clusters as observed, resulting very large particles with height larger than the initial ice thickness. From this perspective the small number of large Ag particles is traceable to the number and dimensions of the liquid water droplets formed in the SK to VW transformation process.

The proposed transformation mode is consistent with the measured 74^{o} contact angle of water on HfO_2 [4.43]. This observation indicates that the strong attractive hydrogen bonding interaction among water molecules competes effectively with the interaction of water with the surface of hafnia. Using the average height-to-diameter ratio determined from AFM line scans, and assuming lens shaped particles (section of a sphere), the average contact angle of the Ag nanoparticles with the HfO_2 surface is 69^{o}, very close to the water contact angle.

On $TMAA^-$ saturated $TiO_2(110)$, a thin water film (=60 L) cannot wet the whole surface at 55 K. It is plausible to assume the water sticking coefficient is unity at both 55 K and 120 K. Because some surface areas are not wetted, the same amount of water forms much larger dimension islands on $TMAA^-$ saturated $TiO_2(110)$ than on HfO_2. Thus, very large water droplets form as water melts. Again, the very large Ag particles reflect the number and dimensions of the water droplets (Figure 4.9d). The height-to-radius ratio is approximate 1, suggesting a superhydrophobic character of the surface as expected. The small particles shown in Figure 4.9c form on the substrate not covered by water.

4.5.3 Comparison of ice to xenon matrices

When Ag is deposited onto a Xe matrix, hemispherical Ag nano-particles form [4.14], and the number density and particle size distribution strongly depends on the thickness of the Xe layer. With 0.1 ML Ag deposited onto 300 ML Xe layer, 1.4 to 9.0 nm particles form, and have a log-normal distribution with number density $\sim 1 \times 10^{10}$ cm^{-2} characteristic of cluster-cluster aggregation [4.55]. Likely, this is the result of agglomeration of highly mobile small Ag clusters in solid Xe matrix during Ag deposition. Unlike ice layers, there is no the process of solid liquefaction to form droplets as Xe is removed. Furthermore, in ice layers, Ag_n cluster agglomeration is much less likely, until liquid droplets form, since (1) water-silver attraction due to dispersion forces is stronger than for xenon-silver, and (2) the ice lattice has much a higher heat capacity (energy absorption capacity) than the xenon lattice ($C_{p,ice} = 2.07$ J $g^{-1}K^{-1}$ vs. $C_{p,Xe} = 0.191$ J $g^{-1}K^{-1}$). Consequently, the thermal energy carried by inbound Ag atoms is dissipated over much shorter trajectories within H_2O(s) than Xe(s), as well as the potential energy released by Ag_n cluster agglomeration.

4.6 SUMMARY AND CONCLUSIONS

Thermally evaporated Ag atoms incident onto a thin (typically ~2 nm) solid water matrix at 55-125 K, penetrate into the ice matrix but do not reach the underlying substrates—amorphous HfO_2, TiO_2(110) and trimethyl acetic acetate pre-saturated TiO_2(110). Subsequent thermal removal of water by heating leads to Ag nanoparticle formation on the surfaces. For 1.5 ML Ag onto 18L water on HfO_2, the average particle height is much larger and the number density of particles (2×10^{10} cm-2) is much lower than on bare HfO_2. The average particle height is 5 times larger than the thickness of the original ice matrix. For Ag deposition onto 18 L water on TiO_2(110), one dimensional strings of Ag nanoparticles form, which distribute randomly on the surface. Separated by the strings, a few large particles and crowed small particles coexist. When water exposure decreases to 4 L, denser and smaller particles spread on the surface randomly compared to deposition of the same amount of Ag on clean TiO_2(110). Onto a 60 L water layer, fewer particles with broad size distribution form. For Ag deposition onto ice layer on $TMAA^-$ saturated $TiO_2(110)$, a very few huge particles with height-to-radius ratio close to 1 form. These results for deposition on ice are described qualitatively by a model that involves (1) formation, during Ag deposition, of a relatively homogeneous spatial distribution of tiny clusters, Ag_n; and (2) the competition of water lateral movement and desorption. Most of the tiny Ag_n clusters retain within water when solid water melts to forms large droplets. Among three surfaces, $TiO_2(110)$ is the most hydrophilic, solid water grows layer by layer (FM). With increasing substrate temperature, water film morphology changes from FM to SK, and water desorption competes. Final particles track the receding rim of water. On HfO_2, the morphology change of water film (from SK to VW) occurs at lower temperature, where desorption is negligible, and large water droplets form. $TMAA^-$ saturated $TiO_2(110)$ is the most hydrophobic, and solid water does not wet the surface. Very large water droplets form as temperature rises.

4.7 REFERENCES AND NOTES

[4.1] Van Santen, R. A.; Kuipers, H. P. C. E. *Adv. Catal.* **1987**, 35, 265

[4.2] Serafin, J.G.; Liu, A. C.; Seyedmonir, S. R. *J. Mol. Cat. A*. 1998, 131, 157

[4.3] Barteau, M. A.; Madix, R. J. *Chem. Phys. Solid Surf. Heterog. Catal.* **1982**, 4, 95

[4.4] Miyadera, T. *Appl. Catal. B* **1993**, 2, 199

[4.5] Zemlyanov, D. Y., Nagy, A.; Schlogl, R. *Appl. Surf. Sci.* **1998**, 133, 171

[4.6] Gaidadymov, V. B.; Skuratov, V. M.; Gromyko, V. A.; Krivobok, N. M.; Vasil'ev, Yu. B.; Khazova, O. A. SU 966026, U.S.S.R., **1982**

[4.7] Mizsei, J.; Pirttiaho, L.; Karppinen, M.; Lantto, *V. Sensors and Actuators B: Chemical* **2000**, B65, 195

[4.8] Slawson, R. M.; Van Dyke, M. I.; Lee, H.; Trevors, J. T. *Plasmid* **1992**, 27, 72

[4.9] Bukhtiyarov, V. I.; Prosvirin, I. P.; Kvon, R.I.; Bal'zhinimaev, B.S.; Podgornov, E. A. *Appl. Surf. Sci*. **1997**, 115, 135

[4.10] Roco, M. C. *J. Nanoparticle Research* 1999, 1, 1

[4.11] Quate, C. F. *J. Nanoparticle Research* **1999**, 1, 131

[4.12] Haruta, M.; Date, M. *Appl. Catal*. **2001**,222, 427

[4.13] Valden, M.; Lai, X.; Goodman, D. W. *Science* 1998, 281, 1647

[4.14] Huang, L.; Chey, S. J.; Weaver, J. H. *Phys. Rev. Lett*. **1998**, 80, 4095

[4.15] Huber, H.; Mackenzie, P.; Ozin, G. A. *J. Am. Chem. Soc*. **1980**, 102, 1548

[4.16] Fisher, M.; Devlin, J. P. *J. Phys, Chem*. **1995**, 99, 11584

[4.17] Diebold, U. *Surf. Sci. Rep*. **2003**, 48, 5

[4.18] Nozik, A. J. *Physica E: Low-Dimensional Systems & Nanostructures* **2002**, 14(1-2), 115

[4.19] Zakrzewska, K. *Thin Solid Films* **2001**, 391(2), 229

[4.20] Schultze, J. W.; Schweinsberg, M. *Electrochimica Acta* **1998**, 43, 2761

[4.21] Famakinwa, T.; Ikezawa, S.; Homyara, H.; Yoshioka, T.; Nakamura, K.; Ninomiya, Y.; Oda, H.; Hara, T.; Hori, M.; Fujii, S.; Yoshimura, K.; Taoda, H. *Problems of Atomic Science and Technology, Series: Plasma Physics* **2000**, 5, 159

[4.22] White, J. M.; Henderson, M. A. *J. Phys. Chem. B* (in press)

[4.23] Schaub, R.; WahlstrÖm, E.; RØnnau, A.; Lægsgaard, E.; Stensgaard, I.; Besenbacher, F. *Science* **2003**, 299, 377

[4.24] Chen, D. A.; Bartelt, M. C.; Seutter, S. M.; McCarty K. F. *Surf. Sci.* **2000**, 464, L708

[4.25] Luo, K.; Clair, T. P. St.; Lai, X.; Goodman, D. W. *J. Phys. Chem. B* **2000**, 104, 3050

[4.26] Lai, X.; Goodman, D. W. *J. Mole. Catal A: Chemical* **2000**, 162, 33

[4.27] Jeon, T. S.; White, J.M.; Kwong, D.L. *Appl. Phys. Lett*. **2001**, 78, 368

[4.28] Gusev, E. P.; Cartier, E.; Buchanan, D. A.; Gribelyuk, M.; Copel, M.; Okorn-Schmidt, H.; D'Emic, C. *Microelectronic Engineering* **2001**, 59, 341

[4.29] Kim, C.; Yan, X.-M.; White, J.M. *Rev. Sci. Instr.* **2000**, 71, 3502

[4.30] Wu, H.; Hsu, H.; Chiang, C. *J. Am. Chem. Soc*. **1999**, 121, 4433

[4.31] Kuo, C.T.; Kwor, R.; Jones, K. M. *Thin Solid Films* **1992**, 213, 257.

[4.32] Park, H.J.; Sun, Y.-M.; Lozano, J.; White, J. M. *Appl. Surf. Sci*. **2002**, 201, 171

[4.33] Safarik, D. J.; Meyer, R. J.; Mullins, C. B. *J. Vac. Sci. Tech. A*. **2001**, 19, 1537

[4.34] Smith, R. S.; Kay, B. D. *Nature* **1999**, 398, 788

[4.35] Powell C.J. NIST Electron Effective-Attenuation-Length Database, Version 1.0. **2001**

[4.36] Fitts, W.P. Ph.D. Dissertation: *Variable-Temperatuer Scanning Tunneling Microscopy Studies of Atomic and Molecular Level Surface Phenomena on Semiconductor and Metal Surface* 2001, 353 pp, University of Texas at Austin

[4.37] Yang, D.; Xiong, Y.; Guo, Y.; Da, D.; Lu, W. *J. Mater. Sci*. **2001**, 36, 263

[4.38] Chusuei, C. C.; Lai, X.; Luo, K.; Goodman, W. *Top. in Cat*. **2001**, 14, 71

[4.39] Onishi, H.; Iwasawa, I. *Surf. Sci*. **1994**, 313, L783

[4.40] Bennett, R. A.; Bowker, M. *Faraday Discuss*. **2000**, 114, 267

[4.41] Mo, Y. W.; Kleiner, J.; Webb, M. B.; Lagally, M. G. *Phys. Rev. Lett*. **1991**, 66, 1998

[4.42] Park, H. J.; Sun, Y.-M.; Troiani, H.; Santiago, P.; Yacaman, M. J.; White, J. M. *Surf. Sci*. **2001**, 521, 1

[4.43] Feng, A.; B. McCoy, J.; Munir, Z. A.; Cagliostro, D. *Mater. Sci. and Eng.* **1998**, A242, 50

[4.44] Kay, Bruce D.; Lykke, Keith R.; Creighton, J. Randall; Ward, Stephen J. *J. Chem. Phys.* **1989**, 91(8), 5120

[4.45] Bartell, F. E.; Cardwell, P. H. *J. Am. Chem. Soc*. **1942**, 64, 494

[4.46] S. Fein’s research Homepage: faculty.washington.edu/fain/fainAVS.pdf

[4.47] Wang, R.; Sakai, N.; Fujishima, A.; Watanabe, T.; Hashimoto, K. *J. Phys. Chem. B* **1999**, 103, 2188

[4.48] Diebold, U. *Appl. Phys. A* **2003**, 76, 681

[4.49] Henderson, M. A. *Surf. Sci.* **1998**, 400, 203

[4.50] Xu, C.; Goodman, D. W. Chem. Phys. Lett. 1997, 265(3-5), 341

[4.51] Liang, G.; Perry, S. Personal Communication

[4.52] Ren, S.; Yang, S.; Zhao, Y.-P.; Xiao, X.; Yu, T. *International Journal of Nonlinear Science and Numerical Simulation* **2002**, 3(3-4), 785

[4.53] Pratt, L. R.; Pohorille, A. *Chem. Rev*. **2002**, 102, 2671

[4.54] Lee, S.H.; Rossky, P. J. *J. Chem. Phys*. **1994**, 100(4), 3334.

[4.55] Gordillo, M. C.; Marti, J. *J. Chem. Phys*. **2002**, 117(7), 3425

[4.56] Park, S.H.; Lee, K.W. *J. Colloid and Interface Science* **2002**, 246, 85

[4.57] Sadtchenko, V.; Knutsen, K.; Giese, F.; Gentry, W. R. *J. Phys. Chem. B* **2000**, 104, 2511

[4.58] Jenniskens P; Banham S. F.; Blake D. F.; McCoustra, M. R. *J. Chem. Phys*. **1997**, 107(4), 1232

[4.59] Morgenstern, M.; Michely, T.; Comsa, G. *Phys. Rev. Lett*. 1996, 77, 703

[4.60] Ogasawara, H.; Yoshinobu, J.; Kawai, M. *J. Chem. Phys*. 1999, 111, 7003

[4.61] Materer, N.; Starke, U.; Barbieri, A.; Van Hove, M. A.; Somorjai, G. A.; Kroes, G.-J.; Minot, C. *Surf. Sci*. **1997**, 381, 190

[4.62] Weber, T.A.; Stillinger, F.H. *J. Phys. Chem*. **1983**, 87, 4277

[4.63] Kroes, G.-J. *Surf. Sci*. 1992, 275, 365

[4.64] Herman, G. S.; Kim, Y. J.; Chambers, A.; Peden, C. H. F. *Langmuir* **1999**, 15, 3993

Bibliography

1. Ali, Ali H.; Zaera, F. *J. Molecular Catalysis A: Chemical* **2002**, 177(2), 215
2. Anger, G.; Winkler, A.; Rendulic, K. D. *Surf. Sci.* **1989**, 220, 1
3. Arvanitis, D.; Doebler, U.; Wenzel, L.; Baberschke, K.; Stoehr, J. *Surf. Sci.* **1986**, 178(1-3), 686
4. Asfin, B.; Davies, P. R.; Pashuski, A.; Roberts, M. W. *Surf. Sci*. **1991**, 259, L724
5. Au, C. T.; Roberts, M. W. *Chem. Phys. Lett.* **1980**, 74(3), 472
6. Au, C.; Liao, M.; Ng, C. *J. Phys. Chem. A* **1998**, *102*, 3959
7. Auger, P. *J. Physique Radium* **1925**, 6, 205
8. Avery, N. R. *J. Am. Chem. Soc*. **1985**, 107, 6711
9. Backx, C.; De Groot, C. P. M. *Surf. Sci*. **1982**, 115(2), 382
10. Barteau, M. A.; Madix, R. J. *Chem. Phys. Solid Surf. Heterog. Catal*. **1982**, 4, 95
11. Bartell, F. E.; Cardwell, P. H. *J. Am. Chem. Soc*. **1942**, 64, 494
12. Bennett, R. A.; Bowker, M. *Faraday Discuss*. **2000**, 114, 267
13. Bent, B. E. *Chem. Rev*. 1996, 96(4), 1371
14. Berko, A.; Solymosi, F. *Appl. Surf. Sci.* **1992**, 55(2-3), 193

15. Bochmann, M. *Organometallics: Complex with transition metal-carbon s-bonds*; Oxford University Press: Oxford, 1994

16. Bol, C.W.J.; Friend, C.M. *Surf. Sci.* **1996**, *364*, L364

17. Borg, J.; Reijerse, J.F.C.-J.M; van Santen, R.A.; Niemantsverdriet, J.W. *J. Chem. Phys. 1994*, **101**, 10052

18. Bowker, M.; Guo, Q.; Joyner, R.W. *Surf. Sci.* **1991**, *257*, 33

19. Bowker, M.; Madix, R. J. *Applications Surf. Sci.* **1981**, 8, 299

20. Bowker, M.; Madix, R. J. *Surf. Sci.* **1982**, 116(3), 549

21. Bowker, M.; Madix, R. J., *Surf. Sci.* **1980**, 95(1), 190

22. Bowker, M.; Madix, R. J., *Surf. Sci.* **1981**, 102, 542

23. Brainard, R. L.; Madix, R. J. *J. Am. Chem. Soc.* **1989**, 111, 3826

24. Brainard, R. L.; Madix, R. J. *Surf. Sci.* **1989**, 214, 396

25. Brown, N.F.; Barteau, M.A. *Langmuir* **1992**, *8*, 862

26. Brown, N.F.; Barteau, M.A. *J. Phys. Chem.* **1996**, *100*, 2269

27. Brown, N.F.; Barteau, M.A. *Surf. Sci.* **1993**, *298*, 6

28. Brown, W. A.; King, D. A. *J. Phys. Chem. B* **2000**, 104, 2578

29. Bukhtiyarov, V. I.; Prosvirin, I. P.; Kvon, R.I.; Bal'zhinimaev, B.S.; Podgornov, E. A. *Appl. Surf. Sci*. **1997**, 115, 135

30. Burch, R.; Breen, J. P.; Meunier, F. C. *Appl. Catal. B* **2002**, 39(4), 283

31. Cammann, K.; Lemke, U.; Rohen, A.; Sander, J.; Wilken, H.; Winter, B. *Angewandte Chemie* **1991**, 103(5), 519

32. Camplin, J. P.; McCash, E. M. *J. Chem. Soc. Faraday Trans.* 1996, 92, 4695

33. Chen, C. J. *Introduction to Scanning Tunneling Microscopy*, Oxford Press, London, 1993

34. Chen, D. A.; Bartelt, M. C.; Seutter, S. M.; McCarty K. F. *Surf. Sci.* **2000**, 464, L708

35. Chiang, C.-M.; Bent, B. E. *Surf. Sci.* **1992**, 279, 79

36. Chusuei, C. C.; Lai, X.; Luo, K.; Goodman, W. *Top. in Cat.* **2001**, 14, 71

37. Chusuei, C. C.; Morris, R. E.; Schreifels, J. A. *Appl. Surf. Sci.* **1999**,153, 23

38. Davis, J. L.; Barteau, M. A. *Surf. Sci.* **1987**, 187(2-3), 387

39. Davis, M.E.; Suib, S.L. *Selectivity in Catalysis*; American Chemical Society: Washington, DC, 1993

40. de Jong, A.M.; Niemantsverdriet, J.W. *J. Chem. Phys.* **1994**, *101*, 10126

Diebold, U. *Appl. Phys. A* **2003**, 76, 681

41. Diebold, U. *Surf. Sci. Rep*. **2003**, 48, 5

42. Dubois, L.H.; Somorjai, G.A. *Surf. Sci*. **1983**, *128*, L231

43. Ekerdt, J. G.; Sun, Y.-M.; Szabo, A.; Szulczewski, G. J.; White, J. M. *Chem. Rev.* **1996**, 96, 1499

44. Endle, J. P.; Sun, Y.-M.; Nguyen, N.; Madhukar, S.; Hance, R. L.; White, J. M.; Ekerdt, J. G. *Thin Solid Films* **2001**, 388(1,2), 126

45. Famakinwa, T.; Ikezawa, S.; Homyara, H.; Yoshioka, T.; Nakamura, K.; Ninomiya, Y.; Oda, H.; Hara, T.; Hori, M.; Fujii, S.; Yoshimura, K.; Taoda, H. *Problems of Atomic Science and Technology, Series: Plasma Physics* **2000**, 5, 159

46. Feng, A.; B. McCoy, J.; Munir, Z. A.; Cagliostro, D. *Mater. Sci. and Eng.* **1998**, A242, 50

47. Fisher, M.; Devlin, J. P. *J. Phys, Chem*. **1995**, 99, 11584

48. Fitts, W.P. Ph.D. Dissertation: *Variable-Temperatuer Scanning Tunneling Microscopy Studies of Atomic and Molecular Level Surface Phenomena on Semiconductor and Metal Surface* 2001, 353 pp, University of Texas at Austin

49. Fu, S. S.; Somorjai, G. A. *Langmuir* **1992**, 8, 518

50. Gaidadymov, V. B.; Skuratov, V. M.; Gromyko, V. A.; Krivobok, N. M.; Vasil'ev, Yu. B.; Khazova, O. A. SU 966026, U.S.S.R., **1982**

51. Gates, Stephen M. *Chem. Rev*. **1996**, 96, 1519

52. Gordillo, M. C.; Marti, J. *J. Chem. Phys*. **2002**, 117(7), 3425

53. Gregoratti, L.; Baraldi, A.; Dhanak, V. R.; Comeli, G.; Kiskinova , M.; Roser, R. *Surf. Sci.* **1995**, 340, 205

54. Grunes, J.; Zhu, J.; Yang, M.; Somorjai, G. A. *Catal. Lett*. **2003**, 86(4), 157

55. Guo, X.; Madix, R. J. *ACS Symp. Ser.* **1996**, 638, 357

56. Gusev, E. P.; Cartier, E.; Buchanan, D. A.; Gribelyuk, M.; Copel, M.; Okorn-Schmidt, H.; D'Emic, C. *Microelectronic Engineering* **2001**, 59, 341

57. Habraken, F. H. P. M.; Kieffer, E. P.; Bootsma, G. A. *Surf. Sci*. **1979**, 83(1), 45

58. *Handbook of Auger Electron Spectroscopy*, 3rd Edition, Physical Electronics, **1995**

59. Haneda, M.; Kintaichi, Y.; Inaba, M.; Hamada, H. *Bull. Chem. Soc. Jpn.*, **1997**, 70, 499

60. Harris, T. D.; Madix, R. J. *J. Catal.* **1998**, 178, 520

61. Haruta, M.; Date, M. *Appl. Catal*. **2001**,222, 427

62. Henderson, M. A. *Surf. Sci.* **1998**, 400, 203

63. Herman, G. S.; Kim, Y. J.; Chambers, A.; Peden, C. H. F. *Langmuir* **1999**, 15, 3993

64. Ho, W. *J. Chem. Phys.* **2002**, 117(24), 11033

65. Hoke, J. B.; Stern, E. W.; Murray, H. *H. J. Mater. Chem.* **1991**, 1, 551

66. Hostetler, M. J.; Dubois, L. H.; Nuzzzo, R. G.; Girolami, G. S. *J. Am. Chem. Soc.* **1993,** 115, *2044*

67. Hostetler, M. J.; Nozzo, R. G.; Girolami, G. S.; Dubois, L. H. *J. Phys. Chem.* **1994,** 98, *2952*

68. Houtman, C.J.; Barteau, M.A. *J. Catal.* **1991**, *130*, 528

69. Houtman, C.J.; Barteau, M.A. *Langmuir* **1990**, *6*, 1558

70. Huang, L.; Chey, S. J.; Weaver, J. H. *Phys. Rev. Lett*. **1998**, 80, 4095

71. Hubbard, A. T., Ed., *Handbook of Surface Imaging and Visualization*, Chapter 59, CRC Press, **1995**

72. Huber, H.; Mackenzie, P.; Ozin, G. A. *J. Am. Chem. Soc*. **1980**, 102, 1548

73. Hwang, C.-H.; Lee, C.-W.; Kang, H.; Kim, C. M. , Surf. Sci. **2001**, 490(1-2), 144

74. Ihm, H. Ph.D. Dissertation: *Thermal activation and intermediates of six-membered cyclic hydrocarbons and alkyl nitrites on platinum(111) and copper* 2000, 169 pp, University of Texas at Austin
75. Ihm, H.; Medlin, J. W.; Barteau, M. A.; White, J. M. *Langmuir* **2001**, 17, 798
76. Ihm, H.; Scheer, K.; Celio, H.; White, J. M. *Langmuir* **2001**, 17, 786
77. Jang, B.W.L.; Spiver, J.J.; Kung, M.C.; Yang, B.; Kung, H.H. *ACS Symposium Series* **1995**, 587, 83
78. Jenniskens P; Banham S. F.; Blake D. F.; McCoustra, M. R. *J. Chem. Phys*. **1997**, 107(4), 1232
79. Jeon, T. S.; White, J.M.; Kwong, D.L. *Appl. Phys. Lett*. **2001**, 78, 368
80. Jones, G.S.; Mavrikakis, M.; Barteau, M.A.; Vohs, J.M. *J. Am. Chem. Soc*. **1998**, 120, 3196
81. Kameoka, S.; Ukisu, Y.; Miyadera, T. *Phys. Chem. Chem. Phys.* **2000**, 2(3), 367
82. Kammler, Th.; Kuppers, J. *J. Phys. Chem. B* **2001**, 105, 8369
83. Kammler, Th.; Kuppers, J. *J. Chem. Phys.* **1999**, 111(17), 8115
84. Kay, Bruce D.; Lykke, Keith R.; Creighton, J. Randall; Ward, Stephen J. *J. Chem. Phys.* **1989**, 91(8), 5120
85. Kim, C.; Yan, X. M.; White, J. M. *Rev. Sci. Instrum.* **2000**, 71, 3505

86. Kirstein, W.; Kruger B.; Thieme, F. *Surf. Sci.* **1986**, 176, 505

87. Konin, G. A.; Il'ichev, A. N.; Matyshak, V. A.; Khomenko, T. I.; Korchak, V. N.; Sadykov, V. A.; Doronin, V. P.; Bunina, R. V.; Alikina, G. M.; Kuznetsova, T. G.; Paukshtis, E. A.; Fenelonov, V. B.; Zaikovskii, V. I.; Ivanova, A. S.; Beloshapkin, S. A.; Rozovskii, A. Ya.; Tretyakov, V. F.; Ross, J. R. H.; Breen, J. P. *Topics in Catalysis* 2001, 16/17(1-4), 193

88. Kovacs, I.; Solymosi, F. *J. Mole. Catal. A* **1999**, 141, 31

89. Kroes, G.-J. *Surf. Sci*. 1992, 275, 365

90. Kua, J.; Faglion, F.; Goddard III, W. A. *J. Am. Chem. Soc*. **2000**, 122, 2309

91. Kubby, J. A.; Boland, J. J. *Surf. Sci. Rep*. **1996**, 24, 61

92. Kubota, J.; Kondo, J. N.; Domen, K; Hirose, C. *J. Phys. Chem*. **1994**, 98, 7653

93. Kung, M. C.; Bethke, K. A.; Yan, J.; Lee, J.-H.; Kung, H. H. *Appl. Surf. Sci.* **1997**, 121/122, 261

94. Kuo, C.T.; Kwor, R.; Jones, K. M. *Thin Solid Films* **1992**, 213, 257.

95. Lackey, D.; Surman, M.; King, D. A.; *Surf. Sci*. **1985**, 162, 388

96. Lai, X.; Goodman, D. W. *J. Mole. Catal A: Chemical* **2000**, 162, 33

97. Lascovich, J. C.; Giorgi, R.; Scaglione, S., *Appl. Surf. Sci.*, **1991**, 47(1), 17

98. Lee, I.; Kim, S. K.; Zhao, W.; White, J. M. *Surf. Sci.* **2002**, 499(1), 53

99. Lee, S.H.; Rossky, P. J. *J. Chem. Phys*. **1994**, 100(4), 3334.

100. Liang, G.; Perry, S. Personal Communication

101. Lin, J.-L.; Bent, B. E. *Chem. Phys. Lett.* **1992**, 194, 208

102. Lin, J.-L.; Bent, B. E. *J. Vac. Sci. Tachnol. A* **1992**, 10, 2202

103. Lin, J.-L.; Chiang, C.-M.; Jenks, C. J.; Yang, M. X.; Wentzlaff, T. H.; Bent, B. E. *J. Catal.* **1994**, 147(1), 250

104. Livneh, T.; Asscher, M. *J. Phys. Chem. B* **2000**, 104(14), 3355

105. Luo, K.; Clair, T. P. St.; Lai, X.; Goodman, D. W. *J. Phys. Chem. B* **2000**, 104, 3050

106. Madix, R. J. *Surface reactions* Chapter 2, Berlin; New York : Springer-Verlag, 1994

107. Manner, W. L.; Dubois, L. H.; Girolami, G. S.; Nuzzo, R. G.; *J. Phys. Chem.* **1998**, 102, *2391*

108. Materer, N.; Starke, U.; Barbieri, A.; Van Hove, M. A.; Somorjai, G. A.; Kroes, G.-J.; Minot, C. *Surf. Sci*. **1997**, 381, 190

109. Matloob, M. H.; Roberts, M. W. *J. Chem. Soc. Faraday Trans. I* **1997**, 73, 1393

110. McCash, E. M. *Vacuum* **1990**, 40, 423

111. Medlin, J. W.; Barteau, M. A.; Vohs, J. M. *J. Mol. Catal.* **2000**, 163, 129

112. Miyadera, T. *Appl. Catal. B* **1993**, 2, 199

113. Mizsei, J.; Pirttiaho, L.; Karppinen, M.; Lantto, *V. Sensors and Actuators B: Chemical* **2000**, B65, 195

114. Mo, Y. W.; Kleiner, J.; Webb, M. B.; Lagally, M. G. *Phys. Rev. Lett*. **1991**, 66, 1998

115. Montreuil, C. N.; Shelef, M. *Appl. Catal.* **1991**, 75, L1

116. Morgenstern, M.; Michely, T.; Comsa, G. *Phys. Rev. Lett*. 1996, 77, 703

117. Nehasil, V.; Stara, I.; Matolin, V. *Surf. Sci*. **1997**, 377-379, 813

118. Netzer, F. P.; Goldmann, A.; Rosira, G.; Bertel, E. *Surf. Sci*. **1988**, 204, 387

119. NIST website chemistry book, http://webbook.nist.gov/chemistry

120. Nozik, A. J. *Physica E: Low-Dimensional Systems & Nanostructures* **2002**, 14(1-2), 115

121. Nyarady, S. A.; Sievers, R. E. *J. Am. Chem. Soc.* **1985**, 107(12), 3726

122. Nyberg, C.; Tengstaal, C. G.; Andersson, S.; Holmes, M. W *Chem. Phys. Lett.* **1982**, 87, 87

123. Ogasawara, H.; Yoshinobu, J.; Kawai, M. *J. Chem. Phys*. 1999, 111, 7003

124. Onishi, H.; Iwasawa, I. *Surf. Sci*. **1994**, 313, L783

125. Outka, D. A.; Friend, C. M.; Jorgensen, S.; Madix, R. J. *J. Am. Chem. Soc.* **1983**, 105, 3468

126. Outka, D. A.; Madix, R. J. *J. Am. Chem. Soc*. **1987**, 109(6), 1708

127. Pallassana, V.; Neurock, M.; Lusvardi, V. S.; Lerou, J. J.; Kragten, D. D.; Van Santen, R. A. *J. Phys. Chem. B* **2002**, 106(7), 1656

128. Papageorgopoulos, D. C.; Ge, Q.; King, D. A. *Surf. Sci.* **1998**, 397(1-3), 13

129. Park, H. J.; Sun, Y.-M.; Troiani, H.; Santiago, P.; Yacaman, M. J.; White, J. M. *Surf. Sci*. **2001**, 521, 1

130. Park, H.J.; Sun, Y.-M.; Lozano, J.; White, J. M. *Appl. Surf. Sci*. **2002**, 201, 171

131. Park, S.H.; Lee, K.W. *J. Colloid and Interface Science* **2002**, 246, 85

132. Park, S.-K.; Yun, T.-H.; Rhee, S.-W. *Proc. Electrochem. Soc.* **1993**, 93(2), *64*

133. Patsalas, P.; Handrea, M.; Logothetidis, S.; Gioti, M.; Kennou, S.; Kautek, W. *Diamond and Related Materials* **2001**, 10(3-7), 960

134. Payne, S.H.; Kreuzer, H.J.; Frie, W.; Heinz, K. *Surf. Sci*. **1999,** 279, 421

135. Payne, S.H.; Kreuzer, H.J.; Frie, W.; Heinz, K. *Surf. Sci.* **1999**, *421*, 279

136. Powell C.J. NIST Electron Effective-Attenuation-Length Database, Version 1.0. **2001**

137. Pratt, L. R.; Pohorille, A. *Chem. Rev*. **2002**, 102, 2671

138. Quate, C. F. *J. Nanoparticle Research* **1999**, 1, 131

139. Ren, S.; Yang, S.; Zhao, Y.-P.; Xiao, X.; Yu, T. *International Journal of Nonlinear Science and Numerical Simulation* **2002**, 3(3-4), 785

140. Roco, M. C. *J. Nanoparticle Research* 1999, 1, 1

141. Russell, J. N., Jr.; Gates, S. M.; Yates, J. T., Jr.. *Surf. Sci*. **1985**, 163, 516

142. S. Fein's research Homepage: faculty.washington.edu/fain/fainAVS.pdf

143. Sadtchenko, V.; Knutsen, K.; Giese, F.; Gentry, W. R. *J. Phys. Chem. B.* **2000**, 104, 2511

144. Safarik, D. J.; Meyer, R. J.; Mullins, C. B. *J. Vac. Sci. Tech. A*. **2001**, 19, 1537

145. Schaub, R.; WahlstrÖm, E.; RØnnau, A.; Lægsgaard, E.; Stensgaard, I.; Besenbacher, F. *Science* **2003**, 299, 377

146. Schenk, A.; Winter, B.; Biener, J.; Lutterloh, C.; Schubert, U. A.; Kuppers, J. *J. Appl. Phys.* **1995, 77**, *2462*

147. Schultze, J. W.; Schweinsberg, M. *Electrochimica Acta* **1998**, 43, 2761

148. Serafin, J.G.; Liu, A. C.; Seyedmonir, S. R. *J. Mol. Cat. A.* 1998, 131, 157

149. Sexton, B. A. *Surf. Sci.* **1979**, 88, 299

150. Shelef, M. *Chem. Rev.* **1995**, 95(1), 209

151. Shustorovich, E.; Bell, A. T. *Surf. Sci*. **1991**, *248,* 359

152. Siokou, A.; van Hardeveld, R.M.; Niemantsverdriet, J.W. *Surf. Sci.* **1998**, *402-404*, 110

153. Slawson, R. M.; Van Dyke, M. I.; Lee, H.; Trevors, J. T. *Plasmid* **1992**, 27, 72

154. Smith, R. S.; Kay, B. D. *Nature* **1999**, 398, 788

155. Solymosi, F. *J. Mole. Catal. A.* **1998**, 131, 121

156. Somorjai, G. A. *Chem. Rev*. **1996**, 96(4), 1223

157. Somorjai, G.A. *Introduction to Surface Chemistry and Catalysis;* Wiley-Interscience: New York, 1994

158. Stuve, E. M.; Madix, R. J.; Sexton, B. A. *Surf. Sci.* **1982**, 119(2-3), 279

159. Sun, Y.-M.; Yan, X.-M.; Mettlach, N.; Endle, J. P.; Kirsch, P. D.; Ekerdt, J. G.; Madhukar, S.; Hance, R. L.; White, J. M. *J. Vac. Sci. Technol. A* **2000**, 18, 10

160. Surman, M.; Lackey D.; King, D. A. *J. Electron Spectroscopy and Related Phenomena* **1986**, 39, 245

161. Surman, M.; Solymosi, F.; Diehl, R. D.; Hoffman P., King, D. A. *Suf. Sci*. **1984**, 146, 144

162. Taylor, K. C. *Catal. Rev.-Sci. Eng.* **1993**, *35* (4), 457

163. Thiel, P. A.; Madey, T. E. *Surf. Sci. Rep.* **1987**, 7, 211

164. Uvdal, P.; Wiegand, B.C.; Serafin, J.G.; Friend, C.M. *J. Chem. Phys.* **1992**, *97*, 8727

165. Valden, M.; Lai, X.; Goodman, D. W. *Science* 1998, 281, 1647

166. Van De Walle, C. G. *Materials Science Forum* **2000**, 338-342 (Pt. 2, Silicon Carbide and Related Materials, Part 2), 1561

167. Van Santen, R. A.; Kuipers, H. P. C. E. *Adv. Catal.* **1987**, 35, 265

168. Wachs, I.E.; Madix, R.J. *Surf. Sci.* **1978**, *76*, 531

169. Wagner, F. T.; Moylan, T. E.; *Surf. Sci.* **1987,** 191, 121

170. Wang, R.; Sakai, N.; Fujishima, A.; Watanabe, T.; Hashimoto, K. *J. Phys. Chem. B* **1999**, 103, 2188

171. Wanger, F.T.; Moylan, T.E.; Schmieg, S.J. *Surf. Sci.* **1988**, *195*, 403

172. Weber, T.A.; Stillinger, F.H. *J. Phys. Chem*. **1983**, 87, 4277

173. Weissermel, K.; Arpe, H.-J. *Industrial organic chemistry*, 3rd Edition, Weinheim, New York, 1997

174. Weldon, M. K.; Friend, C. M. *Chem. Rev.* **1996**, 96, 1391

175. White, J. M.; Henderson, M. A. *J. Phys. Chem. B* (in press)

176. Wiegand, B.C.; Uvdal, P.E.; Serafin, J.G.; Friend, C.M. *J. Am. Chem. Soc.* **1991**, *113*, 6686

177. Wu, H.; Hsu, H.; Chiang, C. *J. Am. Chem. Soc*. **1999**, 121, 4433

178. Xu, C.; Goodman, D. W. Chem. Phys. Lett. 1997, 265(3-5), 341

179. Xu, X.; Friend, C. M. *Langmuir* **1992**, 8, 1103.

180. Xu, X.; Friend, C. M. *J. Am. Chem. Soc*. **1991**, 113, 6779

181. Xu, X.; Friend, C. M. *J. Phys. Chem.* **1991**, 95, 10753

182. Xu, X.; Friend, C.M. *Surf. Sci.* **1991**, *260*, 14

183. Yan, X.-M.; Kim, C.; White, J. M. *J. Vac. Sci. Technol. A* **2001,** 19(5), 2629

184. Yan, X.-M.; Kim, C.; White, J. M. *Thin Solid Films* **2001**, 391(1), 62

185. Yang, D.; Xiong, Y.; Guo, Y.; Da, D.; Lu, W. *J. Mater. Sci.* **2001**, 36, 263

186. Yang, M. X.; Eng, J., Jr., Kash, P. W.; Flynn, G. W.; Bent, B. E. *J. Phys. Chem.* **1996**, 100, 12431

187. Yang, Q. Y.; Maynard, K. J.; Johnson, A. D.; Ceyer, S. T. *J. Chem. Phys.* **1995**, 102, 7734

188. Yao, Y-F. Y. *J. Catal.* **1984**, 87, 152

189. Zaera, F.; Tjandra, S. *J. Am. Chem. Soc.* **1993**, 115, 5851

190. Zakrzewska, K. *Thin Solid Films* **2001**, 391(2), 229

191. Zemlyanov, D. Y., Nagy, A.; Schlogl, R. *Appl. Surf. Sci.* **1998**, 133, 171

192. Zhao, W.; Kim, C.; White, J.M. *Surf. Sci.* **2000**, *451*, 267

193. Zhu, X. Y.; White, J. M. *Catal. Lett.* **1988**, 1(8-9), 247

Vita

Xiaoming Yan was borne on August 18th, 1971 in Henan Province, China. He is a son of Yuanqing and Xueren Yan with an elder sister. He moved to Yaan, Sichuan with his family after he finished his ninth grade in 1986. He graduated from Yaan Middle School as the top one student among more than 300 in 1989, and entered Peking University without the College Entrance Examination. He majored in Chemistry and received his B.S. in 1994. Extending his education at Peking University, he studied complex oxide materials, especially their applications in electrochemistry, and obtained his M.S. in 1997. After teaching less than a year at Sichuan Agricultural University, he entered the graduate studies program in physical chemistry at the University of Texas at Austin in 1998, under the direction of Professor J. M. White. In 2001 he was award the University Continuing Fellowship, Welch Academic Excellent Award, H. R. Henze Teaching Excellent Award, and Faraday Teaching Excellent Fellowship. He was award for outstanding teaching assistant in 2002. In November of 2002, he married Sharon X. Cheng, also a graduate student at UT. After completion of his Ph. D. work in August 2003, he will work at Lawrence Berkeley National Lab as a postdoctoral fellow.

Permanent address: 98 Shoreline Court, Richmond, CA 94804

This dissertation was typed by the author.